Zwitterionic Poly(arylene ether sulfone) Copolymers:

Membrane Applications and Fundamentals

by

Yi Yang

A Dissertation Presented in Partial Fulfillment
of the Requirements for the Degree of
Doctor of Philosophy

Approved June 2019 by the
Graduate Supervisory Committee:

Matthew D. Green, Chair
MaryLaura Lind
Shuguang Deng
Jerry Y.S. Lin
François Perreault

ARIZONA STATE UNIVERSITY

August 2019

ABSTRACT

Zwitterionic polymers, due to their supurior capability of electrostatically induced hydration, have been considered as effective functionalities to alleviate bio-fouling of reverse osmosis (RO) membranes. Bulk modification of polysulfone-based matrices to improve hydrophilicity, on the other hand, is favored due to the high membrane performance, processibility, and intrinsic chlorine resistance. Here a novel synthetic method was demonstrated to prepare zwitterionic poly(arylene ether sulfone) (PAES) copolymers, which was blended with native polysulfone (PSf) to fabricate free-standing asymmetric membranes via non-solvent induced phase separation process. Both the porosity of the support layer and surface hydrophilicity increased drastically due to the incorporation of zwitterion functionalities in the rigid polysulfone matrix. The water permeance and antifouling ability of the blend membranes were both remarkably improved to 2.5 Lm^{-2} h^{-1} bar^{-1} and 94% of flux recovery ratio, respectively, while salt rejection remained at a high level (98%) even under the high exposure to chlorine (8,000 ppm•h). Besides the preliminary blended membrane design, for the future membrane property enhancement, this dissertation also focused on polymer structure optimizations via elucidating the fundamentals from two perspectives: 1). Synthetic reaction kinetics and mechanisms on polycondensation of PAES. Interestingly, in combination of experiments and the computational calculations by density functional theory (DFT) methods in this work, only the aryl chlorides (ArCl) monomer follows the classical second-order reaction kinetics of aromatic nucleophilic substitution (SNAr) mechanism, while the kinetics of the aryl fluorides (ArF) reaction fit a third-order rate law. The third order reaction behavior of the ArF monomer is attributed to the activation of the carbon-fluorine bond by two potassium cations (at least one bounded to phenolate), which associate as a strong three-body complex. This complex

acts as the predominant reactant during the attack by the nucleophile. 2). Optimized copolymer structures were developed for controlled high molecular weight (Mw ~ 65 kDa) and zwitterionic charge content (0~100 mol%), via off-set stoichiometry during polycondensations, following with thiol-ene click reaction and ring-opening of sultone to introduce the sulfobetaine functional groups. The structure-property-morphology relationships were elucidated for better understanding atomic-level features in the charged polymers for future high-performance desalination applications.

ACKNOWLEDGEMENTS

There are many people I have to thank for supporting me throughout the journey of graduate school. First and foremost, I would like to express my sincere gratitude to my faculty advisor, Dr. Matthew D. Green. I thank him for taking me on at the start point of Green research group four and half years ago, and for his countless encouragement on my research pathways for truth. Dr. Green was such my inspiration for my growth to be a person with self-motivations. The work in this dissertation would not have been done without his patient guidance and passion along the way. I also gratefully appreciate the opportunities he provided to me on attending a variety of conferences covering different relevant fields, and also nominating me for fellowships and awards. I am greatly thankful to his guidance on honing my presentation and professional writing skills. His style of academic guidance and belief in principles will ever glow and carry with me.

I wish to thank my joyful mom, Meiying Shi, who always to be the light at night in my life with her unconditional love, interpersonal advice, and girls talks. My dad, Tianliang Yang, makes me feel equally safe that he is always around me whenever I need. Thanks to my sister Meng and brother-in-law Yuan for constantly making fun of me, reminding me not be the center of the universe, and same importantly caring can be the power in life. Also, my Summer, my sun shine.

I must express my gratitude to Dr. Joseph Dennis for his guidance on polymer synthesis, Dr. Frederick Beyer for technical discussion, and also thank all of my ASU colleagues: Dr. Pinar Cay Durgun, Sr. Karl Weiss, Sr. David Lowry, Dr. Cherry Brian, Dr. Jeffery Yarger, Ms. Alexis

Hocken, Dr. Huidan Yin, Dr. Kedi Wu, Dr. Bohan Shan, Mr. Dhruv Dholaria, Meng Wang, Mr. Mani Modayil Korah, Dr. Tianmiao Lai, Mr. Yifei Xu. I greatly thank the coauthors of my publications: Ms. Tiffany Ramos, Mr. Jihun Heo, Ms. Alexis Hocken, and especially Dr. Christopher L. Muhich for his tremendous computational work on the kinetics study as a great contribution to my work. Along with my ASU colleagues, I gratefully thank all of my friends, both at ASU and elsewhere, for being great friends with me and helping me maintain my sanity.

Finally, I would like to thank my committee, Dr. MaryLaura Lind, Dr. François Perreault, Dr. Jerry Lin, and Dr. Shuguang Deng for their technical assistance and guidance. Thanks to Dr. Lind, especially, not only for kindly providing me experimental tools, but also guidance on academia life. Also, thanks to Dr. Perreault for many valuable discussions as well as the guidance on the experiments as much as he could. I would also like to thank NSF for their generous funding of this project.

TABLE OF CONTENTS

LIST OF TABLES

LIST OF FIGURES

Figure Page

Figure Page

Figure Page

Chapter 1: Introduction

1.1 Presentation of Water Crisis

1.1.1 United State Water Portfolio

Clean water is a necessity for both residential and industrial use.[1–3] With worldwide issues such as population growth, climate extremes, industrialization of developing nations, impoverished nations without the infrastructure to produce and distribute potable water and the ever-changing energy landscape, the current demand of sustainable clean water has ballooned at an exponential rate.[4–6] Unfortunately, guaranteeing a sufficient supply of clean water is one of the grand challenges facing society today and in the future.[7] Approximately 1.1 billion people lack access to water and 2.7 billion people experience water scarcity at least one month per year.[8,9] It was predicted by World Wild Life (WWF) that by 2025, two-thirds of the world's population might be facing water shortages.[10] Developing efficient technology as described in this dissertation that enable sustainable access to clean water is critical for ensuring a sustainable water future.

Currently, potable water in the United States mainly comes from surface water that is collected in reservoirs and allocated based on the demands.[11,12] Figure 1.1 depicts trends in drought forecast, current freshwater and saline water usage, and the location and

depth of saline aquifers within the United States.[13,14] As of 2010, freshwater withdrawals from surface water and groundwater sources continue to dominate the country's water usage.[8,15] Within the United States, most of the regions collocated over saline aquifers (e.g., the High Plains, the Southeast, the Southwest, and Southern California) are still suffering from shortages in clean water supply.[16]

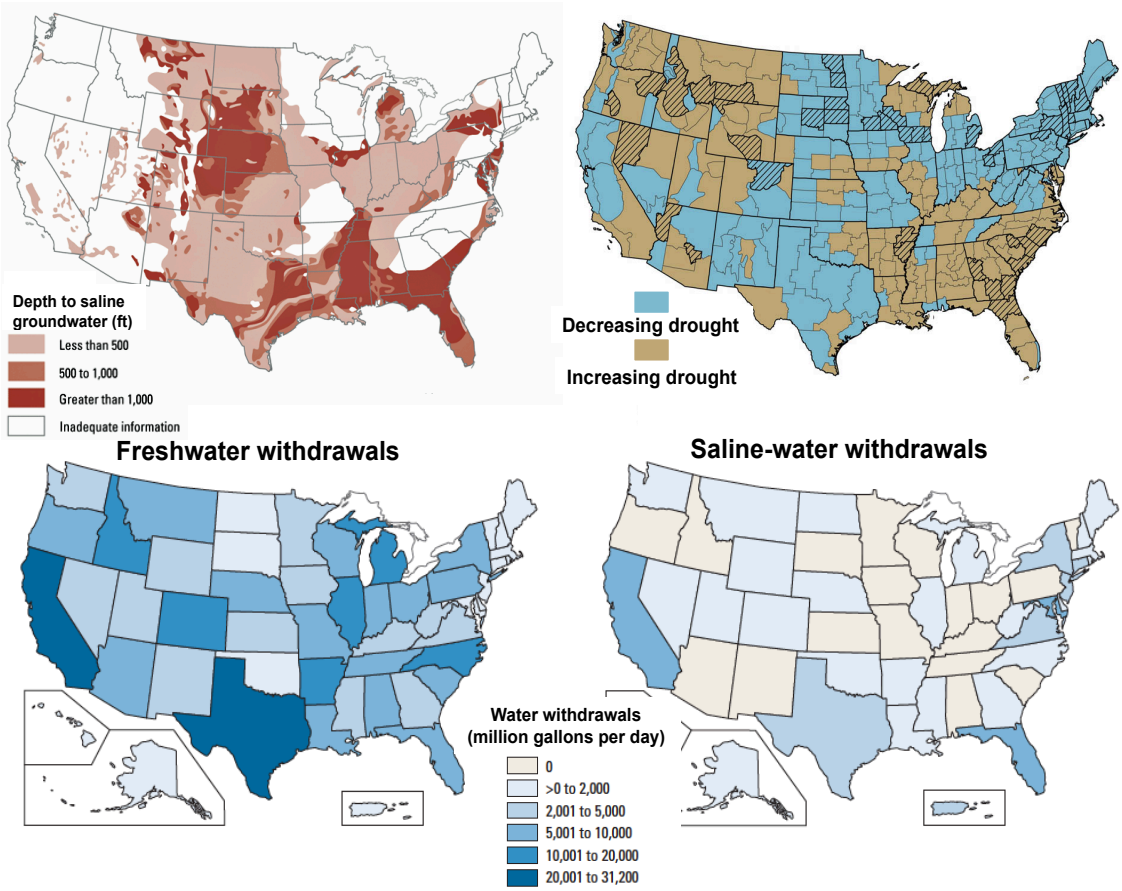

Figure 1.1. Water use, scarcity, and saline water supplies within the US. Top left: location and depth below ground of saline groundwater aquifers. Top right: trends observed in water scarcity according to the Palmer Drought Severity Index from 1958–2007. Bottom: 2010 comparison of regional freshwater and saline-water use.

1.1.2 Mitigation Strategies

The vast majority of potable water comes from surface water that currently

ranges because of reduced snowfall and unpredictable rainfall (recent trends have seen periods of high rain with a tendency to runoff rather than accumulate in natural and/or manmade reservoirs). Growing attention and efforts, therefore, have focused on wastewater reuse and utilization of other water sources (i.e., seawater or brackish groundwater, or even water vapor in desert air) that are more abundant and sustainable than surface water.[17–19] Desalination of seawater has been developed and industrialized since World War II, allowing for a more steady supply from the seemingly endless resource that is the ocean without impairing natural freshwater ecosystems. The first wave of desalination technologies was conventional thermal distillation, which was highly energy-intensive. The next generation of desalination, called reverse osmosis (RO), is still used today and dominates desalination applications in industry. RO consumes much less specific energy and the process and material costs are also lower.[20] Furthermore, according to the 2010 census, approximately 61% of the US population lives >60 miles from a coastline, which highlights the need for inland point-of-use water purification technology.[21] This suggests that not only seawater, but brackish groundwater desalination would serve a significant fraction of the US population and help abate surface water demands during intensifying drought forecasts.[22] Herein, RO technology also serves a superior role by operating with a 60–85% water recovery at a production cost of approximately \$0.4/m^3 for brackish groundwater (these values depend on the quality of the water source).[23–25]

1.2 Membrane-based Desalination

The underlying challenge for desalinating water sources is the perm-selective,

efficient separation salts and other unwanted compounds from water.[20,22] Four broad routes have been proposed based on different driving forces in transport: 1) thermally-driven techniques, such as membrane distillation (MD)[26] and pervaporation (PV)[27,28]; 2) concentration-driven techniques, the typical example is forward osmosis (FO)[29]; 3) electric field-driven techniques, for instance electrodialysis and capacitive deionization;[3] and 4) pressure-driven techniques, such like RO and pressure-retarded osmosis (PRO).[19] This section will compare advantages and disadvantages between RO and some of the efficient, scalable, and promising techniques for desalination. While the first three techniques are all useful technologies for production of potable water from saline water sources, as explained below, only RO desalination can currently address the magnitude of the problem.

1.2.1 Thermally-driven Desalination

In MD, vapor molecules evaporate from the feed solution and are transported through micron-dimension pores (often ranging from 0.1 to 1 μm) of hydrophobic membranes as a distillate.[27,30] The driving force in the MD process is the vapor pressure difference induced by the temperature difference across the membrane. Using MD has many attractive features, such as a theoretical 100% rejection of ions, macromolecules, colloids, cells, and other non-volatiles, which can be reached in a single step. However, the hydrophobicity of MD membrane may decrease resulting in the reduction of permeate flux and the loss of salt rejection due to the wetting of membrane surface during prolonged use. Additionally, MD is still limited by the module and engineering design in a scaled-up application. Desalination by PV is a combination of diffusion of water

through a membrane and its evaporation into the vapor phase on the other side of the membrane to produce fresh water.[28,30,31] PV has some advantages for desalination: salt rejection is quite good, especially for monovalent salts, being generally above 99%, due to the high density of the hydrophilic polymer membranes or the tunable pore size of inorganic membranes. Secondly, as PV is a phase change process, it does not have to overcome the osmotic pressure of saline feed solution. Therefore, PV can handle highly concentrated salt solutions without adjusting the driving force, which is related to the vapor pressure difference across the membrane. Although PV is a feasible way to produce potable water, finding membrane materials with a high performance and low-grade heat source, like solar energy, geothermal energy or waste heat from industry, for heat supply to the feed makes it essentially impossible to retrofit existing desalination plants with this technology. Thus, there are still obstacles for commercial implementation.

1.2.2 Forward Osmosis Desalination

In forward osmosis, the osmotic pressure between the feed solution and a higher concentrated solution on the other side of the membrane provides the driving force to induce a net flow of water through the membrane into the draw solution, thus effectively separating the feed water from the salts.[29] The main advantages of using FO are that it operates at low or no hydraulic pressures, it has high rejection of a wide range of contaminants, and it may have a lower fouling propensity of membranes than pressure-driven membrane processes. Currently, FO faces several difficulties to achieve commercial scales, such as the development of densely packed modules and the

requirements of the draw solutions (needs to be easily separable from the product freshwater, have low or no toxicity, utilize low energy to regenerate or re-concentrate, and are chemically non-reactive with polymeric membranes).

1.2.3 Reverse Osmosis Desalination

Reverse osmosis desalination, especially seawater RO (SWRO), are the current state-of-the-art, which enjoys scalability of membrane modules and has reduced energy consumption to within striking distance of the practical minimum energy requirements for salt separation, are therefore expected to maintain leadership in the near future. This technique uses hydraulic pressure as the driving pressure to oppose, and exceed, the osmotic pressure of an aqueous feed solution to produce purified water. Currently, the largest SWRO plant in the world is in Ashkelon, Israel and it has a production rate of about 110 million m^3 $year^{-1}$. Considering the global average water consumption per capita of 1243 m^3 $year^{-1}$ (5% for domestic use, 85% for agricultural irrigation, and 10% for industrial use), this plant can supply fresh water to less than 100,000 people.[32] Hence mega-sized desalination plants must be developed if we are to provide new clean water supplies to billions of people. In this context, the biggest challenge would be making RO desalination affordable for poorer countries. Unarguably, the capital investment and operating costs of RO plants must be further reduced to achieve this. Electricity (energy), labor, and chemicals make up about 87% of the total RO cost.[33,34] Developments in membrane material and module optimization can significantly contribute to the reduction of all three aspects. Despite these myriad challenges, RO desalination from saline water sources represents the best opportunity for worldwide clean water production.

Among the large number of membrane materials for RO, polymeric membranes have received significant focus due to their low cost, scalability, and promising ability to produce a wide range of membrane types for desalination. The membranes for RO desalination generally include asymmetric membranes and thin-film composite (TFC) membranes.[35] Asymmetric membranes, like the typical Loeb-Sourirajan cellulose acetate (CA) membranes in 1960s, were formed with a dense selective layer over a thick porous layer and showed pure water flux of 0.35 m^3 m^{-2} day^{-1} and a salt rejection of 99% at a transmembrane pressure drop of more than 100 bar and a 4 wt% NaCl solution.[36] However, the susceptibility to hydrolysis and chlorine-mediated oxidative degradation in operation, as well as sensitivity to microbial contamination, limited the durability and precluded commercial implementation. In addition, only a few polymers can form asymmetric structures in one-step solution casting, and even less are commercially preferable in terms of satisfactory performance in water permeability and salt rejection. This led to two-step casting methods that enabled individual optimization of the materials used for the micro-porous support film and for the barrier layer, the former for mechanical support and the latter for optimal salt rejection and permeate flux. Furthermore, a wide variety of polymers can be tested for the barrier layer and support layer separately. Recently reported TFC desalination membranes showed predominant improvements than the previous asymmetric membranes and were designed with various approaches, mainly including interfacial polymerizations,[37] surface grafting,[38] and initiated chemical vapor deposition (iCVD).[39]

1.3 Problem Statement

State-of-the-art RO systems can operate at a specific energy consumption of near 2 kW-h/m^3. With the thermodynamic minimum energy for separation being 1.1 kW-h/m^3 (for seawater at 50% recovery), today's conventional RO systems are already within striking distance of the ''practical energy minimum'' required for separation. There is very little room for further energy-use reductions for desalination of seawater and other waters of lower salinity due to the fact that the energy consumption for RO desalination is limited by thermodynamics. The focus therefore is supposed to shift to cost. Cost encompasses all of the problems and challenges of desalination today: system design, pretreatment, module design and configuration, pumps, fittings, monitoring, energy recovery, system maintenance, and more.[40]

In addition to salt rejection in RO process, membrane rejection or resistance to some other species, such as chlorine-based membrane-cleaning agent and some micropollutants in wastewater, are also needed. The strategies range from extensive pre-treatment, such as microfiltration and ultrafiltration prior to RO stage, to post-treatment, such as multiple RO stages, ion exchange and post-water chlorination. These additional steps contribute substantial chemical and energy usage and incur capital costs, which could be avoided if more fouling/chemically resistant RO membranes were available.

Membrane fouling — that is, the accumulation of substances on the membrane surface or within the membrane pores — is a major obstacle for the efficient operation of membrane systems. Excessive fouling deteriorates membrane performance (that is, water flux and selectivity), necessitates chemical cleaning, which is unsustainable and shortens membrane life, and increases energy consumption and operating costs.[22,41,42] The severity of fouling can vary substantially and is affected not only by feed water quality and

process conditions (for example, transmembrane pressure drop and feed flow rate), but also by the fouling propensity of the membrane itself.[17] The development of membrane materials with a low fouling propensity remains highly important.

Another pitfall of the current polyamide-based TFC membranes is their high sensitivity to chemical degradation by strong oxidants, most notably chlorine-driven oxidative degradation,[43] due to the nature of the amide linkages in the polymer backbone (as shown in Figure 1.2). Polymer degradation leads to the unavoidable replacement of full modules. In addition, after the membrane filtration step, water must be re-chlorinated when used as potable water supply.[44,45] Continuous de- and re-chlorination strongly decrease the efficiency of RO/NF systems, hamper operation and maintenance, while also inducing higher costs.[46]

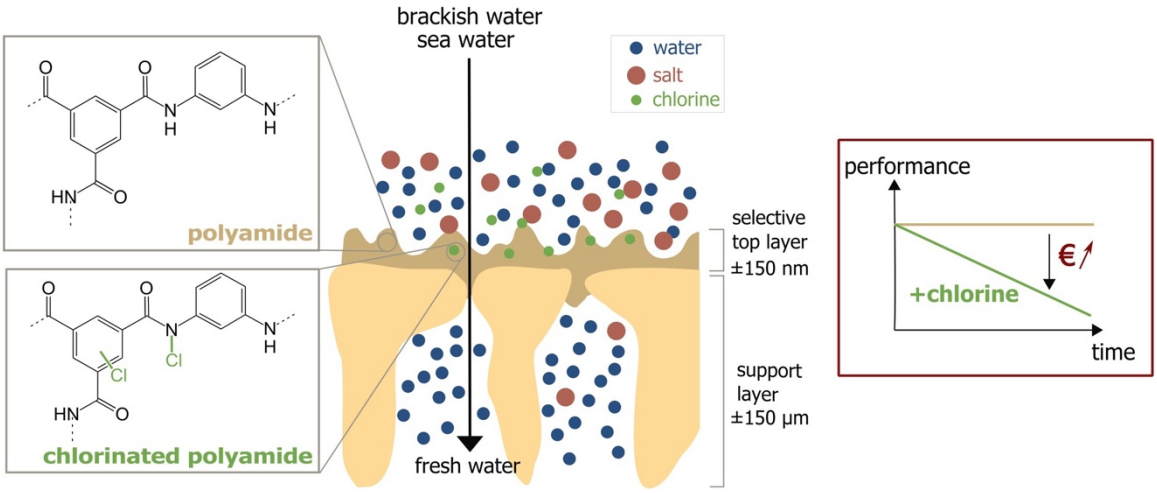

Figure 1.2. Scheme of a membrane for a water purification process. Adapted from R. Verbeke et al./Progress in Polymer Science 72 (2017) 1-15. Copyright with permission from Elsevier.[43]

1.4 Research Motivation

The presentation of all the problems above state-of-the-art RO technology is facing leads to the design of new membrane technologies, processes, or materials. Exclusively, finding alternatives to aromatic polyamide as a next generation of membrane materials for RO is needed to go even further in improving desalination membrane resiliency. The formation of polymeric membranes for targeted performances is a complex phenomenon, since it involves fundamental aspects of chemistry, physics, and material science. In this work, a comprehensive and newly designed polymer structure and the corresponding membrane platform were developed from preliminary desalination application to structure optimization and fundamental understanding of the structure-property relationships. With such a path, sustainable and cost-friendly membrane material candidates would be able to be explored to a broader range, and fundamentals on synthetic routes of the promising polymers and their structures would also be extended.

1.5 Research Objectives

The overarching goal of this work is to develop a new platform of synthetic polymeric membrane that possesses both bio-fouling resistance and chlorine tolerance during the RO desalination process as well as maintains efficient water transport and high salt rejection. This goal will be pursued via (1) the development of a series of novel zwitterion-modified poly(arylene ether sulfone) copolymers and the creation of a membrane platform with the targeted desalination performances; (2) understanding of the polysulfone polycondensation reaction mechanism to facilitate the synthesis of high molecular weight linear polysulfones, which are accessible for further post-

functionalization; (3) the optimization of polymer structure in a controllable fashion for the improvement of mechanical strength of the membranes and also for better understanding of the structure-property relationships.

1.6 Dissertation Organization

After the introduction provided in Chapter 1, the thesis will continue in Chapter 2 into various background material. This includes a brief introduction of polycondensation reactions and the well-accepted theories on reaction kinetics and mechanisms for the guidance of further polymer structure optimization. Next, water filtration/desalination membrane fundamentals will be introduced, ranging from water/ion fundamental transport mechanisms in polymeric membranes, to representative membrane fabrication techniques for different applications, and membrane fouling and oxidative degradation issues and corresponding solutions, which motivated and enlightened this thesis work in order to design a new polymer membrane platform. Chapter 3 will detail a novel synthetic route to prepare zwitterionic poly(arylene ether sulfone) copolymers, the development of fabrication methods to make blend membranes, and membrane characterizations and performances (including fouling/chlorine resistance and desalination performance). Chapter 4 will illustrate the fundamental understanding of the kinetics and mechanisms of polycondensation reactions between bisphenol A and aryl halides (fluoride and chloride) monomers. More importantly, this work discovered the importance of aryl fluoride (or chloride) interactions with dissociated alkali ions and/or alkali containing charge complexes, which from the application perspective dramatically increased polycondensation reaction rate, product conversion, and polymer molecular

weight. In particular, a high polymer molecular weight and a high glass transition temperature is significantly critical to maintain the rigidness of the polymer and the mechanical strength. Based on the theoretical study of the polycondensation mechanisms, the optimized reaction condition parameters and preferential reagents were applied for the work in Chapter 5, as upgraded novel synthesis route for high molecular weight linear poly(arylene ether sulfone) copolymers with flexible chemistry to controllably incorporate a variety of charged functionalities. The effects of charge density on polymer thermal and mechanical properties, as well as other understandings on the structure-property relationships will be discussed. Finally, Chapter 6 will discuss conclusions and potential paths forward to expand the charged polymeric membrane platforms.

Chapter 2: Background and Theory

This chapter provides background information on a number of important topics discussed throughout the dissertation. First, relevant information on polycondensation reaction mechanisms will be considered from a fundamental perspective to complete the framework needed for the reader to understand the work shown later in Chapter 4 on the discovery of a third-order (second-order) rate law of the potassium cations (phenolate complexed) activated aromatic nucleophilic substitution mechanism in the reaction of aryl fluorides (chlorides) and phenolate. Next, the fundamentals of water/salt transport within polymer membranes will be introduced. Furthermore, the chapter will focus on the state-of-the-art polymeric membrane fabrication techniques for water filtration and desalination processes. Finally, biofouling and oxidative degradation of membranes are the two main issues that limit the performance of current RO desalination membranes; thus, these issues will be introduced to provide background information and context for the reader. Preliminary work on a novel membrane platform designed in our lab demonstrated promising membrane performance with respect to biofouling resistance, chlorine tolerance, and water/salt permselectivity (Chapter 3). Therefore, the fundamental understandings of the polymer synthetic route and the structure-property relationships are necessary to further optimize the platform.

2.1 Synthesis of Poly(arylene ether sulfone)s

Poly(arylene ether sulfone) (PAES)-based membranes are commonly used for

ultrafiltration (UF) and microfiltration (MF) membranes, and also as support membranes for reverse osmosis (RO), forward osmosis (FO) and nanofiltration (NF) because of their strong mechanical properties, thermal stabilities, and chemical stabilities in acidic, basic, aqueous, and oxidative environments.[47–49] On the other hand, their intrinsic hydrophobicity makes it hard to act as an active dense layer for efficient transport of water molecules, which in turn limits the permselectivity of water/ions.[50,51] Chemical modifications of PAES, such as sulfonation and carboxylation, therefore, have received attention as strategies to improve the hydrophilicity and fouling resistance of PAES membranes.[52–56]

Starting from the synthesis of pristine PAES, the most commonly applied synthetic routes of polycondensation will be introduced in this section. Then, the corresponding well-accepted mechanism will be discussed to give the reader a detailed perspective on the development of this family of polymers.

2.1.1 Polycondensation of Poly(arylene ether sulfone)s

The original definition of a polysulfone is any polymer containing a sulfonyl group, and they were known and produced as early as the 1960s by Johnson et al. The classical theory of polycondensation developed from the work of Carothers and Flory describes the step growth of monomers which are symbolized as “a-b” monomers (when different reactive functional groups are present on the same monomer and the “a” group must react with the “b” group) or when “a-a” and “b-b” monomers (each monomers has either two “a” or two “b” reactive groups and the “a” group must react with the “b” group) react to afford a linear polymerization.[57] From the polymerization kinetics

analysis perspective, it is much simpler if equal reactivity of functional groups is assumed, and that the reactivity is not influenced by the extent of the reaction. It is also evident that, although experimentally there is a decrease in reactivity with increased molecular size, the effect is significant only at a very small scale, i.e., oligomers, in step-growth polymerizations. The reaction rate constant reaches an upper limit quickly at a degree of polymerization of 3 (i.e., 3 “a” and 3 “b” groups have reacted together), and then remains constant and independent of molecular size during the remainder of the polymerization. Based on this consideration, the rate of a polycondensation reaction to make a PAES is conveniently expressed in terms of the concentrations of the reacting functional groups, i.e., phenol (or phenolate) and aryl halide groups.[58]

The molecular weight of a polymer is of prime concern from a practical perspective, since a polymer will not display desirable thermal or mechanical strength characteristics unless a sufficiently high molecular weight is obtained. It is therefore critical to consider these performance criteria with regard to the control of molecular weight in polycondensation reactions. Since the degree of polymerization, which determines the average length of the linear polymer chain, is a function of reaction time, a desired molecular weight can be obtained by quenching and terminating the reaction at the appropriate time. However, this method may lead to further undesired chain growth due to the fact that the end groups of the polymer remain reactive under subsequent heating (e.g., extrusion or thermal processing techniques). Thus, another way to avoid this situation is to conduct the reaction at an offset stoichiometry, when one kind of functional group is fed at a slight excess relative to the other or when a monofunctional monomer is added, so that the polymerization will proceed to the end when one reactant

is used up and the end of the polymer chain maintains the same functional group that is fed in excess. The quantitative adjustment of this stoichiometric imbalance to control molecular weight was established as the Carothers equation:

$$\overline{X_n} = \frac{1 + r}{1 + r - 2rp}$$

Where $\overline{X_n}$ is the number-average degree of polymerization, r is the stoichiometric ratio of two functional groups ($r \geq 1$), and p is the reaction conversion of the limiting groups.

Since the original polysulfone, poly(phenylene sulfone), has unrealistic processability due to its high melting point of over 500 ˚C,[59] poly(arylene ether sulfone)s (PAES) was developed as an alternative thermoplastic. The most widely used synthetic method to produce PAES, especially high molecular weight PAES, for both industrial and research purposes[52,57,60–69] consists of polycondensation reactions of bisphenols with 4,4'-dichlorodiphenyl sulfone (DCDPS) or with 4,4'-difluorodiphenyl sulfone (DFDPS) in an aprotic polar solvent such as dimethylacetamide (DMAc), or dimethyl sulfoxide (DMSO) using weak base such like potassium carbonate (K_2CO_3) (Scheme 2.1.).[70–72]

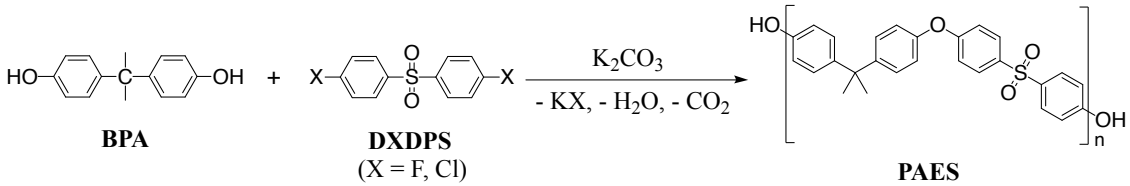

Scheme 2.1. Typical polycondensation route to prepare poly(arylene ether sulfone)s.

2.1.2 Aromatic Nucleophilic Substitution (S_NAr) Mechanism

The mechanism behind this polycondensation reaction is widely accepted as a classical aromatic nucleophilic substitution (S_NAr), in which the aryl halide is activated by the halide, which acts as an electron withdrawing group, toward the attack from the nucleophile.[73,74] When the nucleophile attacks the aromatic structure there is no way to maintain aromaticity. Instead the attacked carbon must adopt a sp^3 tetrahedral intermediate. The loss of aromaticity comes at a huge energetic cost, thus S_NAr is only a reasonable reaction if the resulting anion can be delocalized throughout the aromatic ring. This relatively stable intermediate, called the Meisenheimer complex, was identified in 1902 and has been characterized by both NMR and crystallographic data.[75] The initial attack by the nucleophile on the aromatic structure is the rate determining step. Scheme 2.2 shows the mechanism for the above reaction, including the formation of a Meisenheimer complex.

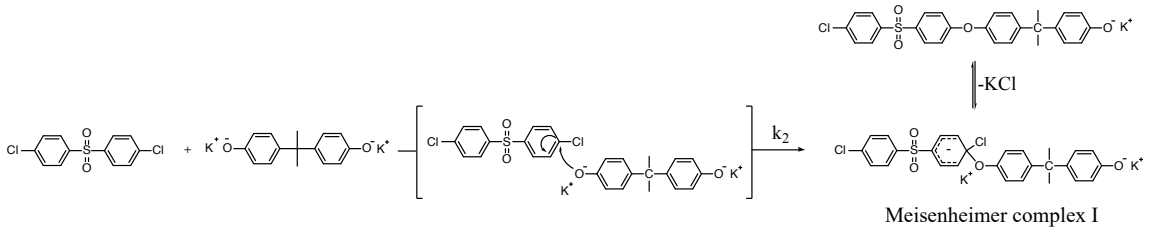

Scheme 2.2. S_NAr mechanism on polycondensation of PAES from ArCl and K^+PhO^-.

In contrast, traditional nucleophilic substitutions (typically known as S_N2 or S_N1), involve a nucleophile attacking on a substrate (electrophile) to replace a leaving group and take place at an aliphatic carbon center. The fundamental mechanisms of S_NAr

reaction and S_N2 reactions have one important distinction, a difference in the rate-limiting step. In S_NAr reactions, the rate limiting step is typically the formation of a Meisenheimer complex[76] (Scheme 2.3) from the two reactant species, for which the reactivity of the aryl halide decreases in the order F>Cl>Br>I based on the electronegativity of the halogen.[73] In the SN_2 reactions, the rate limiting step is when the nucleophile forces off the leaving group, for which the reactivity of the alkyl halides decreases in the opposite order: I > Br > Cl > F based on how the stability of the leaving group as a conjugate base.

2.1.2.1 Linear Kinetics

The vast majority of aromatic nucleophilic substitution reactions display kinetics and responses to structural and environmental factors that indicate a bimolecular mechanism according to criteria stated by Bunnett.[74] In particular, the S_NAr reaction for any aryl dihalide monomer and nucleophile has been well studied and reported as a second order rate law, [74] being first order with respect to the nucleophile and first order with respect to the aryl halide compound. Early evidence from Lulof's thorough investigation of the kinetics of the reaction of 1-chloro-2,4-dinitrobenzene with sodium alkoxides (Table 2.1) showed the usual second-order rate law with good agreement to experimental data. Another example includes the S_NAr reaction between 4,4' dichlorodiphenyl sulfone and bisphenates in an aqueous sodium hydroxide/dimethylsulfoxide system.

Table 2.1. Reaction of 1-chloro-2,4-dinitrobenzene with sodium alkoxides showed typical second-order rate law in S_NAr pathway. [74]

ORIGINAL CONCENTRATION = 0.058 *M*		ORIGINAL CONCENTRATION = 0.035 *M*		ORIGINAL CONCENTRATION = 0.012 *M*	
Time	Second-order rate coefficient	Time	Second-order rate coefficient	Time	Second-order rate coefficient
min.		*min.*		*min.*	
11.1	1.47	31.1	1.63	19.1	1.78
21.6	1.47	42.7	1.63	43.4	1.78
35.5	1.47	53.8	1.62	58.9	1.78
42.5	1.47	63.1	1.63	69.1	1.78
49.9	1.47			86.3	1.78
Mean.....	1.47	Mean.....	1.63	Mean.....	1.78

* Both reactants were in equal concentration in absolute ethanol. Temperature = 15°C. These runs represent about 70–75 per cent reaction.

2.1.2.2 Nonlinear Kinetics

With the widespread studies and understanding on the kinetics and mechanisms of a variety of monomer systems based on the validation of the second-order reaction rate law, some experimental findings showed deviations from the well-accepted kinetic behaviors. The initial and classical route for the synthesis of the family of PAES is via nucleophilic aromatic substitution of 4,4'-dichlorodiphenyl sulfone with bisphenates using dimethylsulfoxide (DMSO) and aqueous sodium hydroxide (commonly referred to as the caustic process). Schulze and Baron used the caustic process and observed an initial curvature in the kinetic plot (Figure 2.1) and justified it to the higher reactivity of one halide in the DCDPS monomer.[77] Another perspective to rationalize can be the inhibited polymer mobility and chain growth during the reaction when the molecular

weight and the intrinsic viscosity of polymer solution keep increasing.

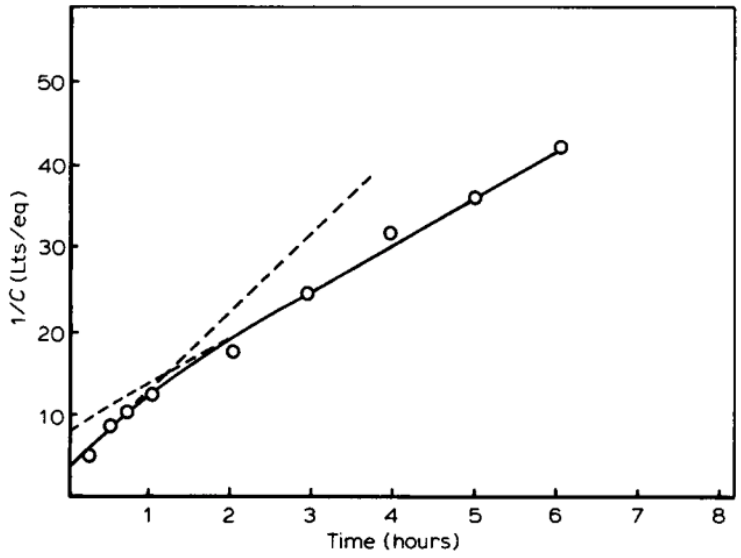

Figure 2.1. Kinetic plot of polymerization reaction of BPA and DCDPS. C0 ~0.25 eq/lts (Expected second order plot).[77]

Although high molecular weight homopolymers can be synthesized in a relatively short time, hydrolytic side reactions can be the limitation for the synthesis of both homopolymers derived from insoluble bisphenates and for copolymers. Many works from the late 1970s therefore turned the interests on using a weak base, such as anhydrous potassium carbonate/N,N'-dimethylacetamide system used by McGrath and coworkers, for the preparation of poly(arylene ether sulfone)s.[77–79]

Investigations of the kinetics and mechanism of this reaction demonstrated that with the use of potassium carbonate as an alternative base, the reaction route deviates from a second order rate expression. Interestingly, the interpreted apparent order of the reaction for preformed phenoxide for various initial concentrations varied from 0.85 to

1.35 as indicated in Figure 2.2. Additionally, the kinetic plot of the reaction of p-(t-butyl) phenol, an example of a model monofunctional phenol with 4,4'-dichlorodiphenyl sulfone, did not yield a straight line when plotting the inverse of concentration versus time. This deviation was been rationalized as a result of the partially insoluble nature of the potassium carbonate in the reaction solution.

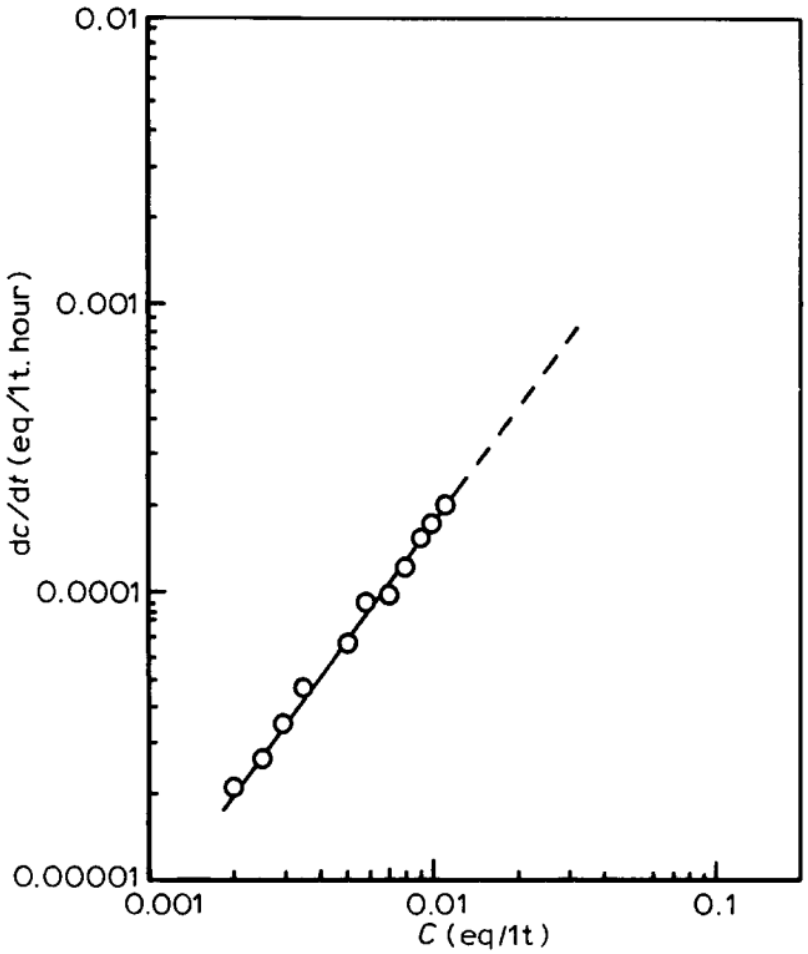

Figure 2.2. Apparent order of polymerization reaction in the presence of performed phenoxide at 150 ˚C (n=1.35 for C0 ~0.015).[77]

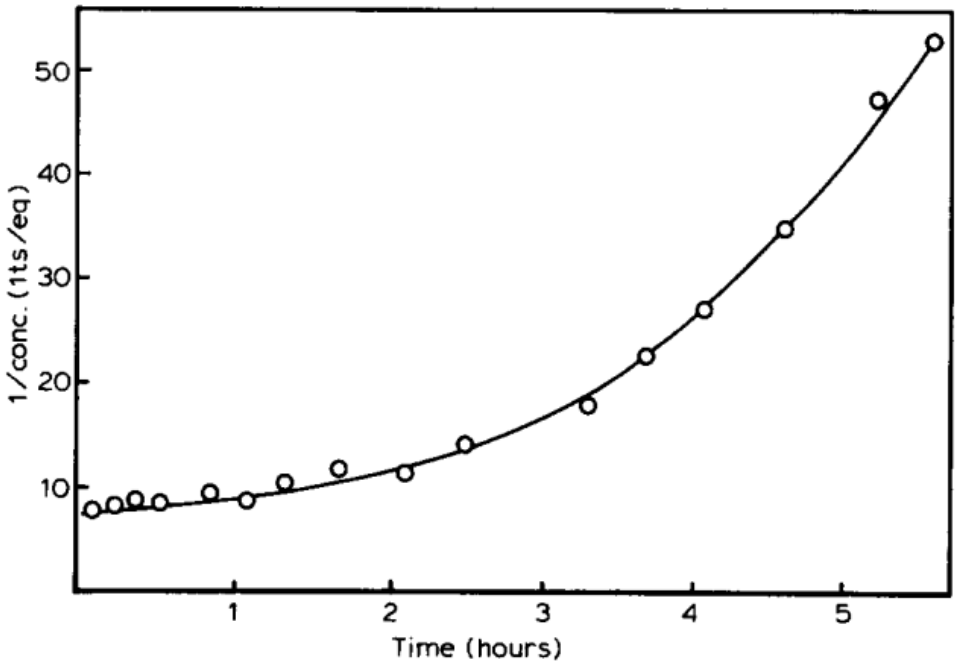

Figure 2.3. Non-linear kinetic plot of the reaction of p-(t-butyl) phenol and DCDPS at 150 ˚C.[77]

Overall, most of the aryl halide and nucleophilic compounds, with various base/solvent effects, have been systematically understood from a kinetic and mechanistic perspective. However, aryl fluoride-based and aryl chloride-based S_NAr reactions are special cases that have not been fully studied in terms of kinetics until this dissertation (Chapter 4).

2.2 Water/ion Transport: Solution-Diffusion Model

The solution-diffusion model summarizes the current understanding of non-porous membrane-facilitated transport processes.[80–82] On the feed side of the dense membrane, solutions containing a high concentration of solute come into contact with the semipermeable membrane, from which water molecules/ions pass.[82] Thus, the solution diffusion process relies on the combined effects of penetrant (i.e., water and/or ion) sorption into the polymer film and subsequent diffusion of the penetrant across the dense polymer. Permeability in this case is defined as,

$$P_i = K_i \times D_i \quad (1)$$

where K_i is the sorption, or partition, coefficient, and D_i is the effective concentration-averaged diffusion coefficient. The quality of the dense layer is not only dependent on how efficient water can pass through (i.e., water permeability or water flux), but it is also characterized by the permeability selectivity, α, defined as the ratio of the permeability of the more permeable penetrant to that of the less permeable penetrant:

$$\alpha \equiv \frac{P_w}{P_S} = \frac{K_w}{K_S} \times \frac{D_w}{D_S} \quad (2)$$

where the so-called sorption, or solubility, selectivity is K_w/K_s, and the so-called diffusivity, or mobility, selectivity is D_w/D_s. Empirically, salt rejection, R, is often reported to describe a membrane's ability to separate water and salt, which is not a material intrinsic property and is often measured under specific operating conditions.

Water sorption in a dense polymer layer is dependent on how many water molecules sorb into the densely packed polymer chain regions or molecularly sized holes between polymer chains, known as free volume. Thus, the water sorption coefficient is

related to the fraction of water in a swollen polymer (ϕ_w) by

$$K_w = \frac{\phi_w M_w}{c_w^S V_w} \quad (3)$$

where M_w is the molecular weight of water, and c_w^s is the mass concentration of water in the external solution. In the case of desalination, when c_w^s is approximately equal to the density of pure water, the water sorption coefficient is essentially equal to the volume fraction of water dissolved in the polymer. In regard to the diffusion coefficient, which is related with the polymer's average free volume $\langle v_f \rangle$, the size of the penetrant is also important in terms of the mobility of the penetrant through molecularly sized windows in the randomly fluctuating polymer matrix, which can be represented by

$$D_i = a_i \times \exp\left[-\frac{b_i}{\langle v_f \rangle}\right] \quad (4)$$

where a_i and b_i are adjustable constants and b_i is proportional to the size of penetrant i. In desalination applications, many salts of interest likely diffuse through swollen polymers as dissociated, hydrated ions with an effective size greater than that of water. Therefore, the more rapid diffusion of smaller water molecules is predicted relative to larger hydrated ions. However, Yasuda et al.[83] suggested that the average free volume, $\langle v_f \rangle$, in swollen hydrogels would exclusively depend on the volume fraction of water dissolved in the polymer matrix, or K_w. It means that both salt and water diffusion coefficients would increase with increased water uptake, which is favorable since water permeability increased if non-porous polymers are more hydrophilic, but simultaneously the diffusion selectivity of water over the hydrated ion decreased. This tradeoff between water diffusion and water/salt diffusion selectivity is actually the dominant factor that gives rise

to the apparent behavior of water/salt transport tradeoff in swollen polymers. This tradeoff is one of the challenges focused on in this research as it associates with an overall energy/cost efficiency of the desalination process. Finally, it is difficult to determine the thickness of the active thin layer in most cases, and as such only the pressure-normalized flux, called permeance, L_p, is used to characterize water transport, rather than P in Equation 1. Normally permeance has units of LMH/bar, defined as,

$$1\ \mathrm{LMH/bar} = 1\ \mathrm{dm^3/m^2 \cdot h \cdot bar} = 2.78 \times 10^{-12}\ \mathrm{m^3/s \cdot N}$$

2.3 Membrane Fabrication Techniques for Water Filtration/Desalination

Polymeric membranes for water desalination have received significant focus due to their low cost, processability, and promising ability to produce a wide range of membrane types for targeted separation applications.[35,84–87] Depending on the size of the solute to be separated, membrane characteristics can be tuned for microfiltration (MF), ultrafiltration (UF), nanofiltration (NF) and RO desalination applications.[88–91] This section will introduce three widely used membrane fabrication techniques for the state-of-the-art polymeric membranes.

2.3.1 Thin-film Composite Polyamide Membranes

Thin-film composite (TFC) membranes, the gold standard for NF, RO, and FO applications, contain a dense thin selective layer on top of a separate porous layer (the support provides mechanical strength during the high pressure process). State-of-the-art

TFC polyamide membranes are most commonly prepared using interfacial polymerization of a diamine — most commonly, m-phenylenediamine (MPD) or piperazine (PIP) — from an aqueous solution penetrating into the support containing a triacyl chloride, usually trimesoyl chloride (TMC), in the organic phase (Figure 2.4).[36,92,93] After the polymerization finishes at the water/organic interface, the polyamide thin film forms and physically attaches on top of the porous support. Then, subsequent hydrolysis of nonreacted acyl chloride groups yields carboxyl groups, which confer a negative charge to the membrane surface and thus further increase the hydrophilicity.

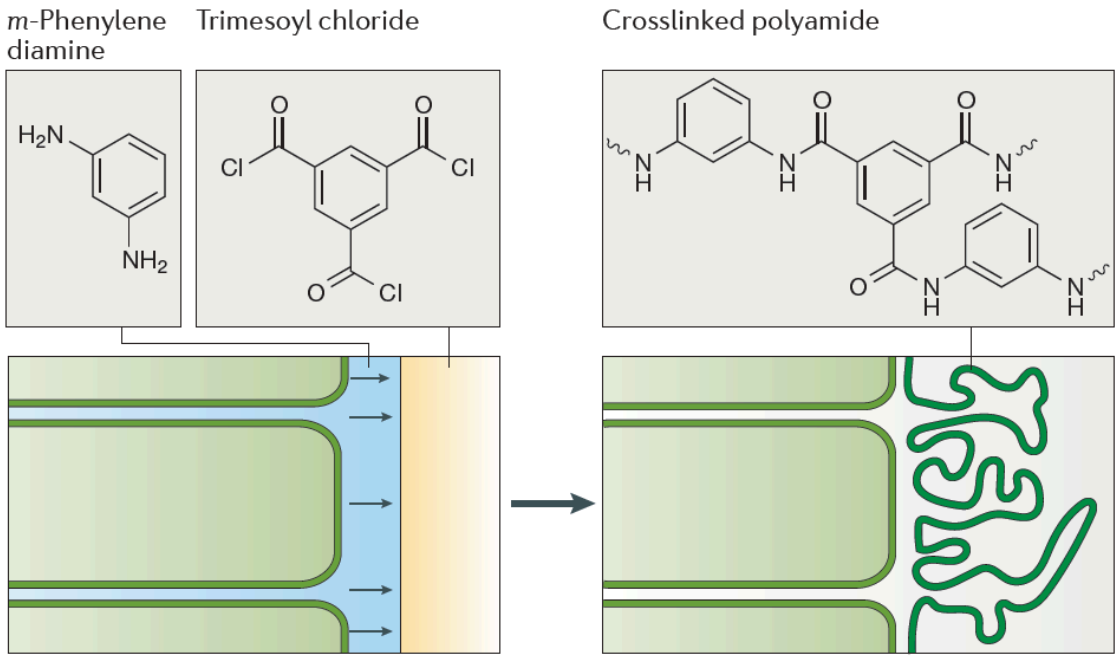

Figure 2.4. A schematic representation of interfacial polymerization to form thin-film composite (TFC) reverse osmosis membranes.[36]

2.3.2 Phase Inversion Membranes

Most commercial porous membranes, such as MF, UF, or the support layer of TFC membranes, as well as some dense membranes for RO and FO, are all fabricated via phase inversion techniques. To form the membranes with a dense selective layer on top and a porous support at one-step casting, a process known as phase inversion, or phase separation, is utilized.[94] Normally in a phase inversion process, a liquid polymer dope solution is precipitated into two phases: a solid, poly-rich phase that forms the matrix of the membrane and a liquid, polymer-poor phase that forms the membrane pores. Typically, based on different mechanisms, precipitations of dope solution can be induced thermally by a decrease in the temperature of the casting film to form a microporous structure, called thermally induced phase separation (TIPS)[95]; alternatively, phase inversion can also happen when there is evaporation of the solvent from the casting film solution, and/or a solvent/non-solvent exchange in either liquid or vapor phase, as called non-solvent induced phase separation (NIPS). The polymer precipitation by NIPS is part of the overall membrane preparation procedure for most of the RO and ultrafiltration membranes, and many gas separation membranes. In the NIPS process, a stable one-phase polymer solution is made at low temperature (20-60 °C), and then is cast on a flat glass plate as a solution exposed to the atmosphere. The relative humidity and exposure time change the membrane morphology. Then, the film solution undergoes a phase inversion via the coagulation in a non-solvent bath (i.e., water). In the current work, the formation and thickness of the dense layer on the top is quite important to improve the water flux of the membranes while maintaining a high level of salt rejection and strong mechanical strength.

The dope solution is often comprised of a polymer, solvent, and sometimes solution modifiers. The precipitation process involves interactions with the non-solvent (i.e., water) and a ternary system phase diagram shown in Figure 2.5 represents the precipitation pathways of different layers of the film. As can be seen, during the precipitation process, the casting solution, starting from a point such as t0 in one-phase regime, enters the two-phase regime by crossing the binodal line. This normally brings the casting solution into a metastable two-phase regime, where polymer solution compositions are thermodynamically unstable but will not precipitate unless well nucleated. As more solvent leaves the casting solution and water enters the solution, the composition crosses into the two-phase regime, where the phase inversion instantaneously happens through polymer and solvent demixing, and solvent/non-solvent exchange, leading to a bi-continuous pore structure. The lines separating the two-phase regime and the metastable regimes are known as the spinodal lines. The spinodal lines meet the binodal line at the critical point. The top surface of the polymer film, in a few seconds after t_0, has almost completely precipitated since this top layer fully contacts water in the first place once the film enters the water bath. When the top surface precipitates, the polymer gel densifies and micropores are not formed. On the other hand, precipitation of the bottom surface is just about to begin from a point near t_0, and eventually forms the pores in the polymer matrix.

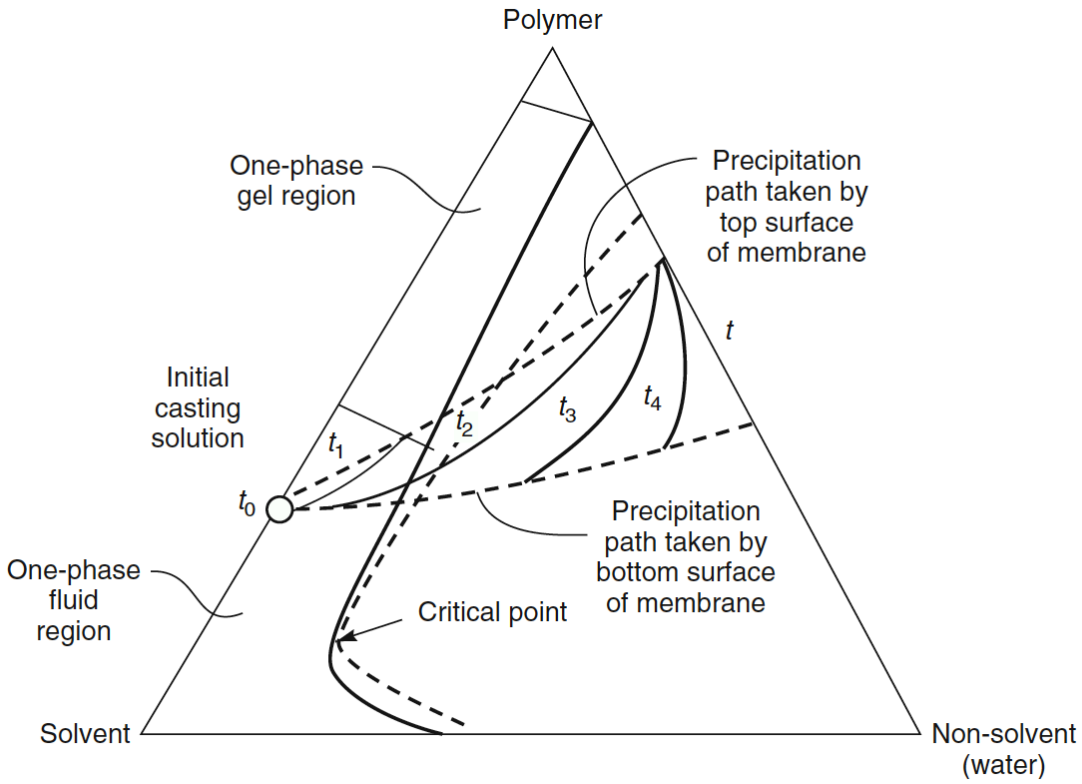

Figure 2.5. The precipitation pathway is presented by the movement of a line through the ternary system phase diagram. The surface layer of water-precipitation membranes precipitates faster than the underlying substrate.[218]

The initial concentration of casting solution is quite important, generally about 25 wt% for RO or gas separation. An appropriate range of solution concentration will lead to the precipitation occurring as a liquid droplet in a continuous polymer-rich phase. Otherwise, if dilute casting solutions are used, in which the precipitation pathway enters the two-phase region of the phase diagram below the critical point, precipitation produces polymer gel particles in a continuous liquid phase, forming powdery membranes. Beyond that, solvent evaporation of the top surface before the film goes into water bath also

facilitates the formation of the top dense layer. After the solvent evaporation step, the top surface would begin to precipitate in water from an even higher point than t_0 (one-phase polymer gel), which may become too rigid to allow the polymer chains rotate, and eventually densifies or even becomes a solid polymer glass.

2.3.3 Fibrous Membranes

Electrospinning is another facile and unique technique used to form porous membranes generally for pretreatment processes to remove divalent metal ions, grease, and other particulates.[96–99] Electrospun nanofibrous membranes possess several attractive attributes, compared with other porous membranes like phase inversion membranes, such as high porosity, control over pore size, interconnected open pore structure, and a large surface area per unit volume.[100] The electrospinning technique (scheme shown in Figure 2.6) requires the application of a high voltage to draw polymer fibers out of a liquid solution toward a grounded target. In the electrospinning process, the electrified jet containing an entangled polymer solution generates solid fibers by continuing to stretch due to the electrostatic repulsions between the charged polymer surfaces, which extend from the Taylor cone toward the target as the solvent begins to evaporate. The technique is a simple and cost effective to produce fibers ranging in size from 10 nm –100 mm.[101,102] Another advantage of electrospinning is the number of tunable parameters, such as: concentration, voltage, solvent choice, ambient humidity, temperature, and sample-to-target distance.[103] Each of these variables can influence the characteristics of the fiber and the nonwoven mat and are easily tailored.

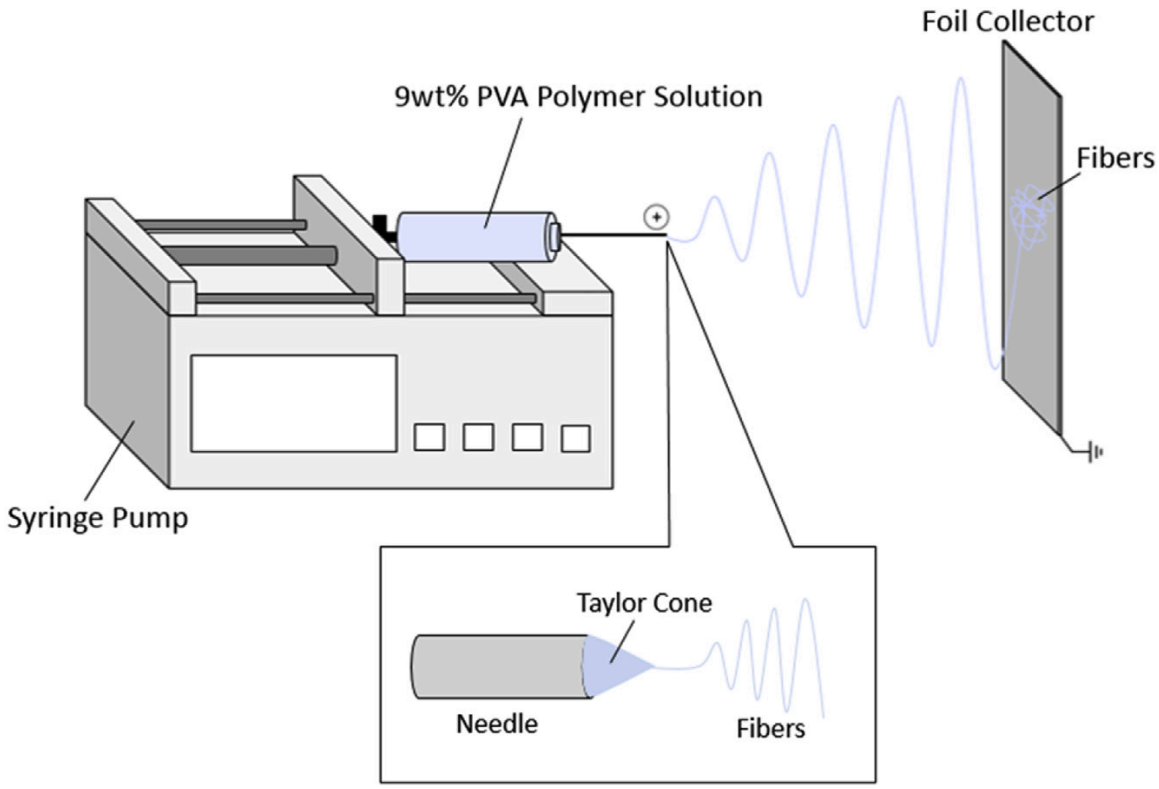

Figure 2.6. Schematic of the horizontal electrospinning apparatus.[104]

Our earlier works on developing eco-friendly electrospun fibrous membranes, for example, illustrated the flexibility and controllability of this techniques on membrane hydrophilicity, fiber diameter, and effective pore size, etc. via tailoring the fabrication parameters.[105] Specifically, we tailored the content ratio between hydrophobic compounds, i.e., poly(vinyl chloride) (PVC) and hydrophilic species, i.e., soy protein, in the polymer mixture solutions to optimize the membrane morphologies, such as fiber diameter, pore surface area, and membrane hydrophilicity. The compositions of the series of blend membranes with different PVC/soy protein ratios were confirmed using Fourier transform infrared (FT-IR) spectroscopy (Figure 2.7-1). Then, SEM images of the series

of blend membranes were collected (Figure 2.7-2) and showed a decrease in average inter-fiber spacing and average fiber diameter with an increase in the soy protein content.

(1)

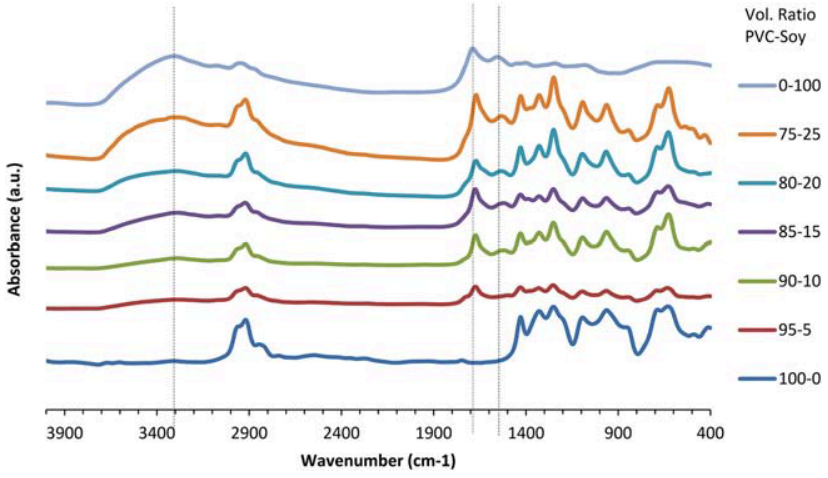

(2)

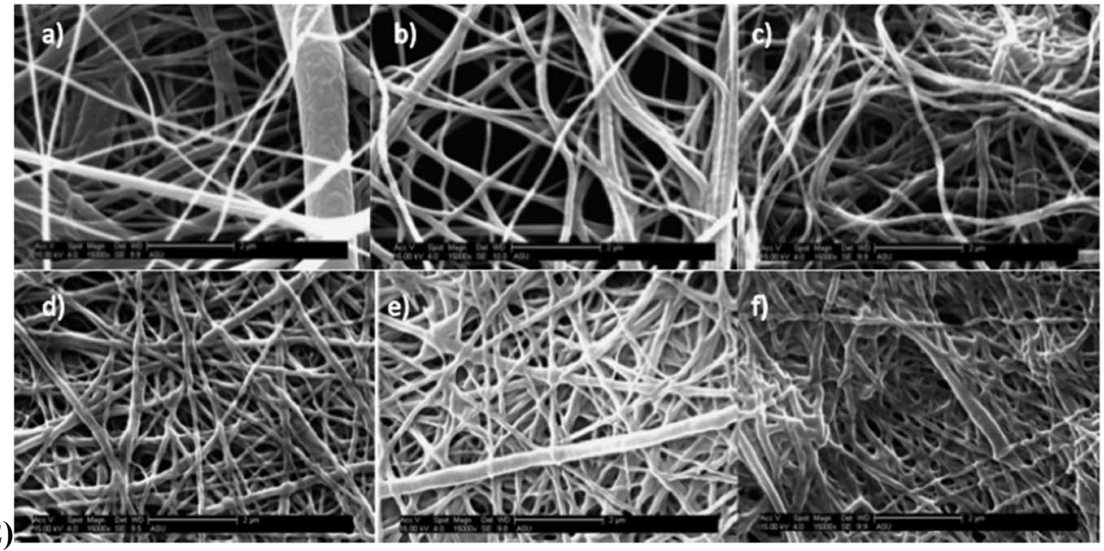

Figure 2.7. (1) Confirmation of mat compositions by Fourier-transform infrared spectroscopy (2) SEM surface images of PVC-soy protein electrospun mats in various PVC/soy protein contents ((a) (100:0), (b) (95:5), (c) (90:10), (d) (85:15), (e) (80:20), and (f) (75:25) (volumetric ratio of 15 wt % PVC:15 wt % soy protein)).[105]

Another relevant work studied the fabrication and characterization of crosslinked

electrospun poly(vinyl alcohol) (PVA) nanofibrous membranes. This study thoroughly investigated the effects of the chemical structure of the crosslinker, poly(ethylene glycol) (PEG) diacid, on the membranes morphologies and their physical properties. Specifically, by controlling the chain length of the PEG diacid crosslinkers during the crosslinking process of the pristine electrospun PVA nanofibrous membranes, the average fiber diameter increased while the average pore area decreased significantly (Figure 2.8). Importantly, in terms of the correlations to the properties that are critical for potential pre-treatment membrane processes, the crosslinked membranes showed enhanced thermal and mechanical properties, as well as the impressive controllability on membranes swellings.

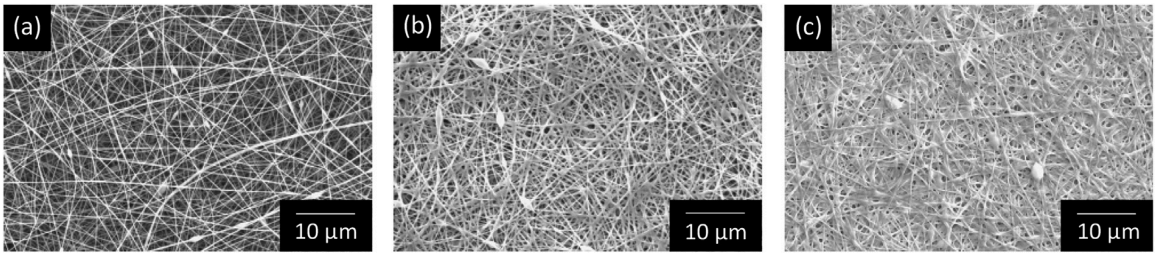

Figure 2.8 Scanning electron micrographs of (a) as spun 9 wt % PVA mat, (b) 9 wt % PVA mat crosslinked with the short PEG diacid (M_n = 250 g/mol), and (c) 9 wt% PVA mat crosslinked with the longer PEG diacid (M_n = 600 g/mol).[104]

2.4 Challenges and Solutions in RO Membrane Processes

2.4.1 Bio-fouling in RO Processes

Water filtration and desalination membranes in general are prone to organic and biological fouling because of their inherent chemical and physical surface properties.[106–110] Proper tailoring of the surface chemical properties of membrane can substantially enhance the fouling resistance. There are three types of fouling: organic fouling by adsorption of dissolved organic matter; scaling by deposition of precipitated salts or by surface nucleation and growth of sparingly soluble salts; and biological fouling (biofouling) by deposition and growth of microorganisms to form strongly adherent biofilms.[111] While physical accumulation of particulates (cake formation) is typically managed by module design, controlling the membrane surface chemistry is crucial in mediating both adsorptive fouling by organic compounds and cell adhesion.[112–114] This can be achieved by functionalizing the membrane surface with chemical moieties that strongly resist organic molecule adsorption and cell adhesion. Specifically, there are three surface characteristics critical to alleviating the affinity between bio-foulants and the surface: (1) hydrophilicity, (2) hydrogen bond acceptor presence/concentration, and (3) electroneutral and absence of hydrogen bond donors.[36]

The most common hydrophilic materials incorporated in fouling-resistant surfaces are poly(ethylene oxide) (PEO)-based and zwitterionic (containing equal numbers of anionic and cationic groups connected by covalent bonds) polymers. The binding between water molecules and zwitterionic polymers, i.e., polysulfobetaine and polycarboxybetaine, is formed via dipole interactions, which are much stronger than the hydrogen binding between water molecules and PEO. It was proposed that the hydration layer of the hydrophilic surfaces provides a strong steric repulsive barrier that prevents the adsorption of organic molecules and bacteria. These hydrophilic groups or segments

can be incorporated onto a membrane surface by various designs and approaches, mainly including surface grafting, initiated chemical vapor deposition (iCVD), or coating.[115–120] These methods, however, involve post-modification of formed membranes which introduce additional manufacturing steps and associated costs. They also typically cause an initial decline in pure water flux.

An efficient way to incorporate fouling-resistant functionalities in the membranes without incorporation of additional manufacturing steps involves the combination of amphiphilic surface-segregating copolymers and commodity polymer for relatively easy processability (Figure 2.9). The blend membrane is commonly fabricated via NIPS with the incorporation of in situ surface segregation. Specifically, during the phase inversion process, the hydrophilic zwitterion copolymers only result in isolated zwitterionic groups or highly constrained short segments to all the polymer/water interfaces. The surface segregation creating a membrane surface as well as the interior pore walls with an exposed hydrophilic layer that imparts fouling resistance, while in the meantime the hydrophobic backbone of the amphiphilic copolymer or the commodity polymers ensure rigidness of the polymer bulk matrix.[121,122] This surface segregation behavior of the amphiphilic copolymers during the phase inversion process has been successfully used to fabricate porous membranes that efficiently inhibit the adsorption of organic foulants and adhesion/growth of microorganisms on the membrane surface.

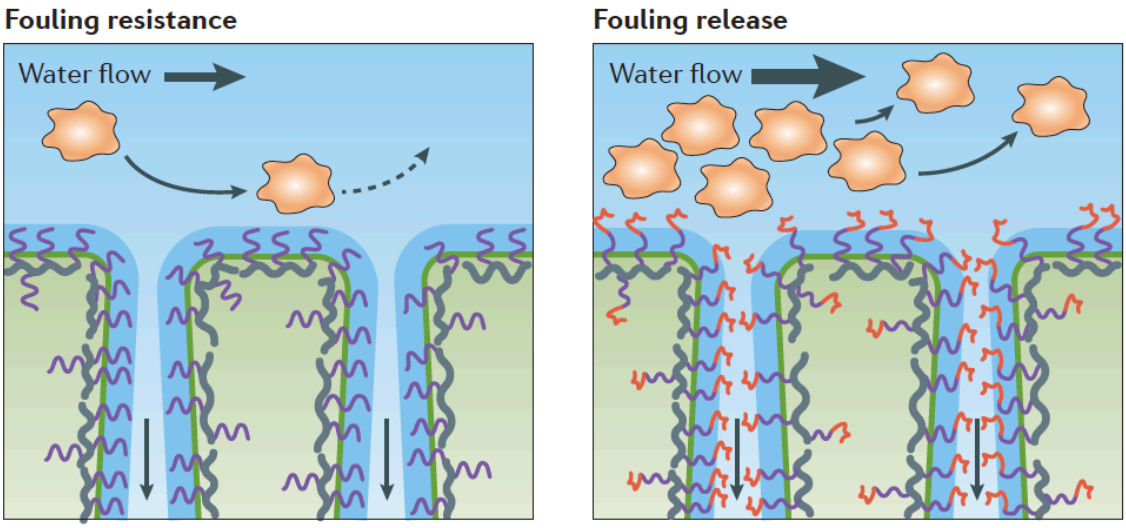

Figure 2.9. Polymeric materials and self-segregation approach for fouling minimization in phase inversion membranes. In this approach, the phase inversion casting solution contains a hydrophobic polymer and a comb copolymer with a hydrophobic backbone and side chains that are at least partially hydrophilic. During non-solvent-induced phase separation in water, the hydrophilic side chains self-segregate at the membrane/water interface, whereas the backbone anchors itself in the membrane matrix.[36]

It is worth noting that besides the surface chemistry modifications, the surface morphology also plays a crucial role on the membrane bio-fouling propensity. Typically, piperazine (PIP)-based polyamide TFC membranes are relatively smooth and have a root-mean-square (RMS) roughness of less than 10 nm. Whereas, the m-phenylenediamine (MPD)-based polyamide TFC membranes have a characteristic 'rigid-and-valley' rough structure with RMS roughnesses over 50 nm. The roughness is due to protruding polyamide nodules by the nature of interfacial polymerizations for the formation of the selective thin layer. Although the rough nodular morphology increases surface area, which may improve water permeability, the increased roughness also enhances all types

of fouling, given the fact that the foulant has a higher opportunity for attachment to the membrane. Therefore, many researchers have studied strategies to control the surface morphology. A recent work by Chowdhury et al.[123] shows that thinner, smoother membranes with roughness as low as 2 nm can be made with an electrospray technique, and that they maintain a comparable perm-selectivity relative to a commercial benchmarking membrane.

2.4.2 Oxidative Degradation in Polyamide RO Membranes

As illustrated earlier, the polyamide-based TFC membranes instinctively perform worse after chlorination due to the sensitivity of the amidic nitrogen, and therefore, by definition, are non-chlorine-tolerant. Many mechanisms of chlorine attack to PA were proposed, such as (1) the predominant route that the oxidizing species (HOCl) attacks the amidic nitrogen via N-chlorination reaction followed by Orton rearrangement, which is promoted in acidic media (Figure 2.10); (2) the hydrolysis of the amidic group; (3) the chlorine attack to the free aromatic amine end-groups and unreacted amine monomers, which results in cross-linking of these species and tightened polymer networks; (4) the chlorinated PA-membranes undergo a diffusion-limited relation process through swelling, which induces a physical change of PA layer and thus their perm-selectivity performances.[44,124–127]

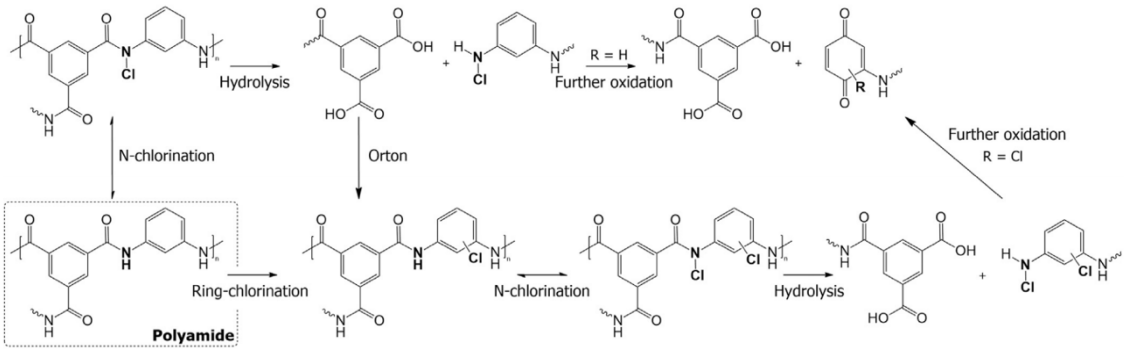

Figure 2.10. Scheme of the mechanism on PA degradation by chlorine attack. Adapted from R. Verbeke et al./Progress in Polymer Science 72 (2017) 1-15. Copyright with permission from Elsevier.[43]

Many approaches have been suggested to develop chlorine-tolerant membranes, in order to extend membrane lifetime and increase the operation efficiency of RO systems. A chlorine-tolerant membrane would eliminate the need for dichlorination before RO and re-chlorination in post-treatment, and thus reduce the capital cost. Polymeric membranes, such as CA, polysulfone, polyimide, polymethacrylate, polybenzimidazole and polystyrene were already proved to be chlorine-tolerant.[128–135] However, because of their limited perm-selectivity performances (i.e., hydrophobicity, narrow operation condition range, etc.), these RO membranes still remain uncompetitive with PA in terms of their RO desalination performances. Chemistry modification of polymers and membrane coatings[136] and surface grafting,[137] or introducing nanoparticles[130] have been the most widely researched perspectives.

Specifically, by alternating the monomer species during interfacial polymerizations, based on the polymer tolerant towards chlorine in order of aromatic >

cycloaliphatic > aliphatic diamines, PA-membranes with higher chlorine-tolerance were obtained. Other non-PA-based membrane systems have also shown exceptional chlorine-tolerance for RO processes, of which sulfonated poly(arylene ether sulfone)s is an outstanding representative.[51,138,139] Polysulfone has much better chlorine tolerance over a broad range of pH values than aromatic polyamides because its main chain consists of aromatic rings and chemically strong bonds between carbon, sulfur, and oxygen. Sulfonation of polysulfone has been reported as a material design strategy to increase the hydrophilicity and subsequently improve the water flux. Also, the sulfonate groups enhance Donnan exclusion, which can improve the perm-selectivity.

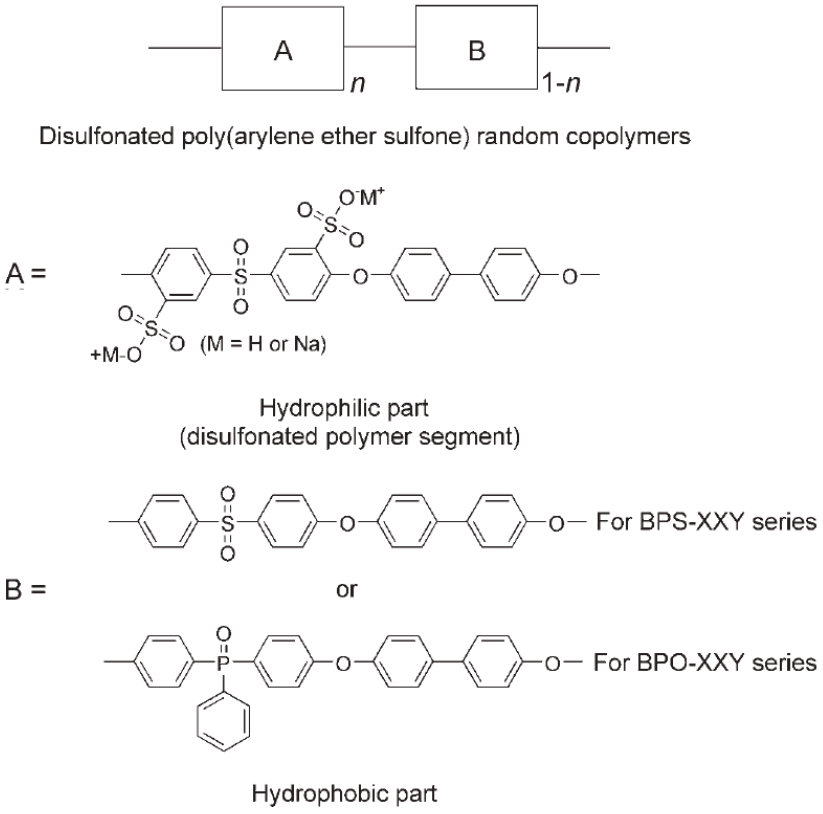

Figure 2.11. Chemical structure of random, disulfonated poly(arylene ether sulfone)s. A=hydrophilic segment, B=hydrophobic segment; XX=mol% disulfonated monomer (20, 30, 35, and 40); Y=H (free acid form) or N (sodium salt form).[51]

2.5 Summary

This section provides a summary of the polymer chemistries, membrane processing, and transport processes in desalination. For polymer synthesis, fundamentals on polycondensation reaction of polysulfone elucidated the kinetics, reaction mechanisms, and subsequently guided the optimization of polymer structures. An overview of the water filtration and desalination membranes followed to provide a whole picture for the later chapters, from the fundamental understanding of the transport behavior to the current representative techniques in membrane fabrications and finally the main challenges and solutions in the field.

Chapter 3: Zwitterionic poly(arylene ether sulfone) copolymers Part 1: Synthesis, Blend Membrane Preparation, and Membrane Performances

Published as

Yi Yang, Tiffany L. Ramos, Jihun Heo, Matthew D. Green, "Zwitterionic poly(arylene ether sulfone) copolymer/poly(arylene ether sulfone) blends for fouling-resistant desalination membranes", Journal of Membrane Science, 561 (2018), 69-78. DOI: 10.1016/j.memsci.2018.05.025.

3.1 Introduction

Polymeric membranes for water desalination have received significant focus due to their low cost, processability, and promising ability to produce a wide range of membrane types for targeted separations applications.[35,84–87] Polysulfone (PSf) based membranes are commonly used for ultrafiltration (UF) and microfiltration (MF) membranes, and also as support membranes for reverse osmosis (RO), forward osmosis (FO) and nanofiltration (NF), because of their strong mechanical properties and their thermal and chemical stability.[47–49] On the other hand, their intrinsic hydrophobicity makes it hard to act as a selective dense layer against small molecules and salt.[50,51] Chemical modifications of polysulfone, such as sulfonation and carboxylation, therefore, have received attention as strategies to improve the hydrophilicity, and thus water permeance, as well as the fouling resistance of polysulfone membranes.[52–56]

Polysulfobetaines, in which both the sulfonate anion and the ammonium cation are covalently attached to the same repeat unit, have been used to prepare zwitterionic polyelectrolytes that improve the anti-fouling properties of water purification membranes.[140,141] Zwitterions improve anti-fouling on membrane surfaces because of their high intrinsic hydrophilicity, which forms a hydration layer through electrostatic interaction between zwitterions and water molecules. This hydration layer provides a steric repulsive barrier to prevent the adsorption of organic molecules and bacteria on the substrate surface.[142] There are many works on polysulfobetaine-based membranes for water desalination; however, most of the membranes reported are polyamide (PA) or poly(sulfobetaine methacrylate) (PSBMA) based thin-film composite (TFC) membranes, which contain a dense selective layer on top of a separate porous layer (the support provides mechanical support for the selective layer that would fail at the high process pressures). Recently reported zwitterionic TFC desalination membranes were designed with various approaches, mainly including interfacial polymerizations,[37] surface grafting,[38] and initiated chemical vapor deposition (iCVD).[39] However, there are pitfalls for these approaches, such as 1) high sensitivity of PA- or PSBMA-based selective layers to chlorine-driven oxidative degradation,[43,143] and 2) specialized devices and complicated pre-treatment steps, which make it hard to scale up due to increased fabrication costs and energy consumption.

In contrast, the bulk modification of polysulfone-based matrices to improve hydrophilicity is favored due to the intrinsic chlorine resistance,[55] facile processing conditions, high membrane performance, and scalable synthesis and manufacturing.[50] In addition, it was reported that increasing the hydrophilicity of the support layer (e.g., if the

functionalized PSf was used as the support instead of the selective layer) also facilitated a reduction in internal concentration polarization (ICP), which had a positive effect on water permeability (up to 18% pure water permeability enhancement for sulfonated supports when compared to non-sulfonated supports) and salt rejection.[52,144] However, to our best knowledge, few reports so far focused on RO desalination, anti-fouling properties, and chlorine resistance of zwitterionic polysulfone-based membranes by bulk modification on both the selective layer and the porous support.

In the present work, we developed a convenient route to prepare charge-modified polysulfone-based desalination membranes. A zwitterionic copolymer, poly(arylene ether sulfone-co-sulfobetaine arylene ether sulfone) (PAES-co-SBAES), was synthesized and characterized using ^{1}H NMR spectroscopy and size exclusion chromatography. Then, the copolymer was blended with PSf to control the charge content and the membranes were prepared by the non-solvent induced phase separation (NIPS) process. The effects of zwitterionic SBAES segments on membrane morphology and hydrophilicity were investigated. Finally, the transport and anti-fouling properties, as well as the chemical stability, of the blended membranes for water desalination were tested, and all membrane performances were compared with a commercial PA TFC membrane.

3.2 Experimental

3.2.1 Materials and Reagents

2,2'-Diallylbisphenol A (DABA, 85%) was purchased from Sigma-Aldrich and distilled from tetrahydrofuran (THF) under vacuum before use. 4,4'-Dichlorodiphenyl

sulfone (DCDPS, 98%) was purchased from Sigma-Aldrich and recrystallized from diethyl ether before use. THF and toluene (99.8%) were purchased from Sigma-Aldrich and used after passing through M. Braun SPS-800 solvent purification system. Bisphenol A (BPA, ≥99%), 18-Crown-6 (99%), N,N-Dimethylacetamide (DMAc, 99.5%), N,N-Dimethylformamide (DMF, ≥99.8%), potassium carbonate (K_2CO_3, ≥99%), 1,3-propane sultone (1,3-PS), polysulfone (16,000 Da by MO), bovine serum albumin (BSA, ≥98%), deuterated chloroform ($CDCl_3$, 99.8 atom% D, 0.03% (v/v) TMS), 2-(Dimethylamino) ethanethiol, 2,2-Dimethoxy-2-phenylacetophenone (DMPA, 99%) were all purchased from Sigma-Aldrich and used as received. Chloroform (99.8%) and hydrochloric acid (HCl, 36.5-38%) were purchased from BDH® VMR analytical and used as received. Fluorescein-conjugated BSA (FITC-BSA, Life Technologies, A23015) and phosphate-buffer saline (PBS) were generously provided by the group of Dr. Francois Perreault at Arizona State University. A commercial TFC RO membrane BW30 (DOW Chemical Co. Ltd. (Minneapolis, MN, USA)) was provided by Prof. Mary Laura Lind.

3.2.2 Synthesis of PAES-co-SBAES copolymers

3.2.2.1 Synthesis of allyl-modified poly(arylene ether sulfone) (A-PAES) copolymer

The allyl-containing poly(arylene ether sulfone) copolymer was synthesized via traditional step-growth polymerization.[67] BPA (7.54 g, 33.06 mmol), DABA (0.53 g, 1.74 mmol), DCDPS (10 g, 34.8 mmol), K_2CO_3 (4.8 g, 34.8 mmol), and 18-Crown-6 (0.1 g) were added to a three-neck, 250-mL flask equipped with a condenser, Dean Stark trap, nitrogen inlet/outlet, and a mechanical stirrer. DMAc (95 mL) and toluene (46 mL) were

added to the flask to dissolve the monomers. The solution was heated under reflux at 110 ˚C for 4 h while the toluene-water azeotrope was removed from the reaction mixture, and then the toluene was completely removed by slowly increasing the temperature to 130 ˚C. The reaction was continued for 36 h at 130 ˚C. The reaction mixture was cooled to room temperature and diluted with 200 mL of chloroform. It was filtered to remove the salt, then stirred with excess 36.5%-38% HCl for 2 h at 25 ˚C, and precipitated by addition to stirring DI water. The polymer was filtered and dried under vacuum at 100 ˚C for 24 h. Then, the polymer was dissolved in chloroform, passed through a 0.45 μm Teflon® filter, then isolated by precipitation in DI water. The product (A-PAES(1), referred as A-PAES if not specified) was dried at 100 ˚C under vacuum for 24 h.

3.2.2.2 Synthesis of tertiary amine-modified PAES (TA-PAES) copolymer

The synthesized PAES copolymer (5 g, 1 mmol), 2-(dimethylamino) ethanethiol (1.4 g, 10 equiv.), and DMPA (76.8 mg, 0.3 equiv.) were dissolved in DMF (20 mL) to perform a post-polymerization modification via the thiol-ene click reaction.[145] The reactor flask was purged with nitrogen for 15 min. Irradiation with UVGL-15 compact UV lamp (365 nm) was carried out for 2 h at 23 ˚C. The solution was concentrated using a rotary evaporator, and the remaining solution was diluted with THF (5 mL) and dialyzed against THF in a dialysis tube (1 kDa MWCO) for 3 days. The THF outside the dialysis tube was exchanged with fresh THF every 2 h over the first 10 h and then every 6 h until completion. The polymer was then isolated by precipitation in DI water, and the product was dried at 100 °C under vacuum for 24 h.

3.2.2.3 Synthesis of PAES-co-SBAES copolymers

To a solution of TA-PAES (4.8 g, 1 mmol) in DMF (20 mL), 1,3-propane sultone (244.3 mg, 2 equiv.) was added. The solution was stirred at room temperature for 1 h and at 60 °C for 18 h. The solution was concentrated using a rotary evaporator, and the remaining solution was diluted with THF (5 mL) and dialyzed against THF in a dialysis tube (1 kDa MWCO) for 3 days. The THF outside the dialysis tube was exchanged with fresh THF every 2 h over the first 10 h and then every 6 h until completion. The polymer was then isolated by precipitation in DI water, and the product was dried at 100 °C under vacuum for 24 h. In addition, to demonstrate the suitability of the reaction conditions, an A-PAES copolymer (A-PAES(2)) was synthesized and functionalized (with product nomenclature of PAES-co-SBAES(2)) in the same fashion as described in Section 2.2. However, in this case a lower molecular weight was targeted via offset alcohol:chloride stoichiometry, and a different allyl group content was targeted by controlling the DABA:BPA ratio; the overall stoichiometry was 9:81:100 BPA:DABA:DCDPS.

3.2.3 Characterization of PAES-co-SBAES copolymers

3.2.3.1 Copolymer structure

^{1}H-NMR spectroscopy was performed on a Varian 400 MHz spectrometer using deuterated chloroform ($CDCl_3$) to determine the copolymer chemical structures. Samples were prepared as 20 mg of dried polymer dissolved in deuterated chloroform. Chemical shifts are given in ppm downfield from tetramethylsilane (TMS).

3.2.3.2 Molecular weight

In order to determine the molecular weight of the copolymers, size exclusion chromatography (SEC) was performed using a Waters Alliance e2695 HPLC system interfaced to a light scattering detector (miniDAWN TREOS) and an Optilab T-rEX differential refractive index (dRI) detector. The mobile phase was THF Optima (inhibitor-free) at a flow rate of 1.0 mL min^{-1}, and samples were calibrated against Pressure Chemical Company low dispersity polystyrene standards of 30 kDa and 200 kDa using Astra v6.1 software. Then, ~1.0 $mg \cdot mL^{-1}$ filtered solutions of polymer in THF were prepared for SEC.

3.2.4 Fabrication of PSf/PAES-co-SBAES blend membranes

The PSf/PAES-co-SBAES blend membranes were prepared via the NIPS process.[146–149] In a typical process, a mixture of PSf and PAES-co-SBAES (total of 1.0 g) was dissolved in THF (3.0 g) at room temperature for 6 h. The weight ratios between PAES-co-SBAES and pristine PSf were 0, 0.25, 0.68, and 1.52, corresponding with the weight percent of zwitterionic segment in the blends as 0, 2, 4, and 6 wt%, respectively (labeled as M-0, M-2, M-4, and M-6). After 6 h of sonication, the dope solution was left at room temperature for another 6 h, and then spread onto a flat glass plate with a doctor blade at a wet thickness of 100 μm, evaporated at room temperature and 20% relative humidity for 20 s. Then, the plate and partially dried solution were immersed into a coagulation bath of deionized water at 25 °C. The blend membrane spontaneously lifted from the glass plate, after which it was washed thoroughly with deionized water and stored in fresh deionized water for future use. Each membrane was air-dried overnight and dipped in 50% isopropanol for 20~30 min before the following tests.

3.2.5 Membrane characterization

3.2.5.1 Membrane morphology and properties

Membrane composition was determined by fourier transform infrared (FT-IR) spectrum (4000-400 cm^{-1}) on a Nicolet™ iS™ 50 FT-IR spectrometer at 4 cm^{-1} resolution and 32 scans. Membrane thickness and morphology were characterized using an environmental scanning electron microscope Philips XL30 ESEM-FEG operating at 4 kV. Membrane samples were freeze-fractured using liquid nitrogen for cross-sectional examination, and sputter coated with gold before imaging. Membrane surface morphology and roughness were obtained using atomic force microscopy (AFM). Samples for AFM were scanned by Dimension Multimode 8 with tapping mode. The scanning speed was set to 1 Hz, and scanning size was 256 × 256. Data were analyzed by Gwyddion software. Surface hydrophilicity of the membranes was tested by water contact angle measurement (Attension Theta optical tensiometers, Biolin Scientific). Five random spots on the surface were measured for each membrane sample at room temperature and the average value was taken.

3.2.5.2 Membrane separation performance

Filtration experiments were performed on 49 mm diameter membranes using a 300 mL Sterlitech HP4750 stirred, dead-end filtration cell with an effective filtration area of 14.6 cm^2. A Sartorius ED3202S extend precision balance connected with a LabVIEW software was used to monitor the flow rates every 3 s. All filtration tests were performed at room temperature and feed solution was stirred in 125 rpm by using a Teflon-coated magnetic stir bar to reduce concentration polarization. All tested membranes were

supported by a polyester fabric support (Whatman, 47mm). All filtration membranes were pre-pressurized under a hydrostatic pressure of 8 bar for at least 30 min, and then following the filtration tests were performed and recorded with the same hydrostatic pressure of 8 bar. Before each filtration test was performed, deionized water was first passed through the membrane until the system remained stable for at least 30 min. Flux is the flow rate through the membrane normalized by membrane active area. Permeance is a membrane transport property that normalizes the flux with the applied transmembrane pressure, and is obtained by

$$J_V = \frac{Q_V}{A_m} \quad (1)$$

$$L_P = \frac{J_V}{\Delta P - \Delta \pi} \quad (2)$$

Where J_v is the volumetric filtrate flux across the membrane ($L \cdot m^{-2} \cdot h^{-1}$), Q_v is the volume flow rate ($L \cdot h^{-1}$), A_m is the effective membrane area (14.6 cm^2), ΔP is the hydrostatic pressure (bar), $\Delta \pi$ is the osmotic pressure (bar), and L_p is the permeance of the membrane ($L \cdot m^{-2} \cdot h^{-1} \cdot bar^{-1}$).

To characterize the salt selectivity of the membranes, we used sodium chloride as the salt during filtration tests. A 2.0 g/L aqueous solution of sodium chloride was filtered through the membrane. The salt rejection and salt passage were calculated by the definition that

$$R(\%) = \left(1 - \frac{C_P}{C_F}\right) \times 100\% \quad (3)$$

$$SP(\%) = 100\% - R(\%) \quad (4)$$

Where R is the salt rejection (%), SP is the salt passage (%), C_P is the permeate concentration (g/L), and C_F is the feed concentration (g/L). C_P and C_F were measured by an Accumet Excel XL50 conductivity meter. For each copolymer ratio, three membrane samples prepared under same conditions were tested.

3.2.5.2 Fouling resistance tests

Fouling tests were performed using a cross-flow filtration system with membrane effective size of 8.4 cm × 4.6 cm in each cell. Considering the normal RO operating pH is 7-9, the fouling experiment of 0.1 g/L bovine serum albumin (BSA) in pH 7.0 ± 0.1 at 200 psi (~13.8 bar) and 25 °C were performed for both M-4 and M-BW30. First deionized water was filtered through the membrane until the system stabilized. This pure water flux was taken as the initial flux J_{W1} ($L \cdot m^{-2}$). Then we added 0.1 g/L BSA aqueous solution in pH 7.0 ± 0.1, and protein solution flux J_P ($L \cdot m^{-2}$) was recorded every 60 s. After 12 h of protein solution filtration, the membranes were rinsed with deionized water for 3 h and the time was not counted in the filtration process. Pure water flux for the washed membrane was re-measured as J_{W2} ($L \cdot m^{-2}$) to determine the flux recovery ratio (FRR) and total fouling ratio (R_t) by Eqs. (4) and (5). The same procedure was followed for the blend membrane and the control.

$$FRR = \frac{J_{W2}}{J_{W1}} \times 100\% \quad (4)$$

$$R_t = \left(1 - \frac{J_P}{J_{w1}}\right) \times 100\% \quad (5)$$

Irreversible fouling resistance of the membranes was tested further by monitoring the adhesion of fluorescein-conjugated BSA (FITC-BSA) on the membrane active surface using an epifluorescence microscope. Specifically, 5.0 mg of FITC-BSA was dissolved in 1 mL of phosphate-buffer saline (PBS) at pH 7.4; then, 50 μL of the solution was taken and diluted to a concentration of 0.05 mg/mL. Tests were performed on membrane fragments approximately 1 cm^2 in area, which were adhered to the surface of a petri dish using chemical-resistant tape applied to the edges of the membrane (such that only the top surface of the membrane contacted the BSA solution). Then, 5.0 mL of the prepared FITC-BSA solution was added to fully cover the surface of the membranes, which were incubated on a rocking plate (60 rpm) for 3 h in the dark. After the solution was removed from the dish, the membrane surface was rinsed with fresh PBS for 1 min on the rocking plate (60 rpm). Then the membranes were cut and placed on a glass slide. One drop of deionized water was added on the membrane surface before a cover slip was placed on top, the combination was sealed with nail polish to avoid any evaporation of water during fluorescence imaging. The prepared sample was then observed on an inverted Axiovert 200M epifluorescence microscope (Carl Zeiss Inc., Thornwood, NY, USA). For each sample, ten spots were randomly chosen to acquire fluorescence images. The fluorescence intensity of the acquired image was processed by ImageJ software for further analysis.

3.2.5.3 Membrane stability tests

To test the chemical stability of the membrane under chlorine exposure, the M-2 and M-BW30 membranes were exposed to an aqueous solution of sodium hypochlorite at a concentration of 1.0 g/L for up to 12 hours in a sealed container; initially, the available chlorine in the sodium hypochlorite solution was calibrated using iodometric titration[150], and concentrated HCl was added in order to adjust the pH value of the solution to 7.1. After exposure, the membrane was rinsed with deionized water twice. Then, filtration performance was evaluated before and after exposure to chlorine as described above in Section 2.5.

3.3 Results and Discussions

3.3.1 Synthesis of PAES-co-SBAES copolymers

Copolymers containing a relatively hydrophobic poly(arylene ether sulfone) (PAES) backbone and hydrophilic sulfobetaine side chains were synthesized by step growth polymerization and post-polymerization modifications. The backbone structure was chosen as PAES due to its high glass transition temperature, which is significantly above room temperature (>200 °C for high molecular weights),[151] strong mechanical properties, and chlorine resistance. Sulfobetaine was chosen as the functional group to attach to the PAES backbone through post-polymerization modifications due to its hydrophilicity and demonstrated anti-fouling performance in membrane applications. Additionally, free-standing membranes would be obtained (due to the T_g and modulus of PAES-based polymers) that are compatible and miscible with a PSf matrix in order to prepare blended membranes with tunable charge content. The allyl-modified PAES

copolymer was prepared by introducing BPA and DCDPS in the presence of potassium carbonate in toluene/DMAc, as well as an allyl-containing monomer, DABA, (Scheme 1). In this way, the PAES copolymers with pendant allyl groups can be functionalized after the polymerization (i.e., with zwitterions) and the concentration of allyl functionality can be tailored by varying the monomer ratio of DABA/BPA. The polymers were synthesized via step-growth polymerization at temperatures below the standard conditions for PSf synthesis in order to reduce the isomerization of allyl groups and other side-reactions (e.g., regioisomers can form on the PAES copolymer, shown in the upper right of Scheme 3.1).

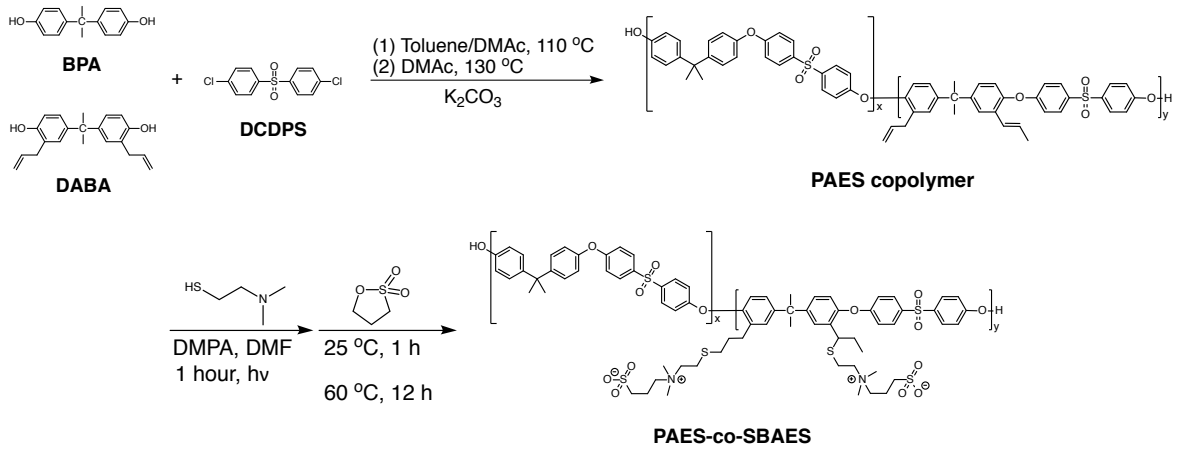

Scheme 3.1. Synthesis of zwitterionic PAES-co-SBAES copolymers.

From the analysis of ^{1}H-NMR spectra (Figure 3.1), the ratio of DABA incorporated into the copolymer matched what was fed to the reaction, indicating favorable polymerization behavior. Subsequent post-polymerization modification reactions successfully introduced tertiary amines and the ring-opened sultone yielded the zwitterion copolymer. A fraction of the allyl groups isomerized, even while performing

the polymerization at a low temperature. In spite of this, the thiol-ene click reaction was successful and the tertiary amine-modified PAES (TA-PAES) copolymer was isolated. Importantly, no unsaturated bonds from the allyl group or the corresponding isomer were observed following the thiol-ene click reaction. Therefore, amphiphilic PAES-co-SBAES(1) (referred as PAES-co-SBAES, if not specified) copolymers with SBAES content of 10 wt% and PAES-co-SBAES(2) with SBAES content of 20 wt% (based on ^{1}H-NMR spectroscopy) were synthesized successfully. As an aside, the zwitterion functionality was introduced in this work due to its potential fouling resistance; however, the allyl precursor serves as a platform to introduce any number of functional groups through the thiol-ene reaction.

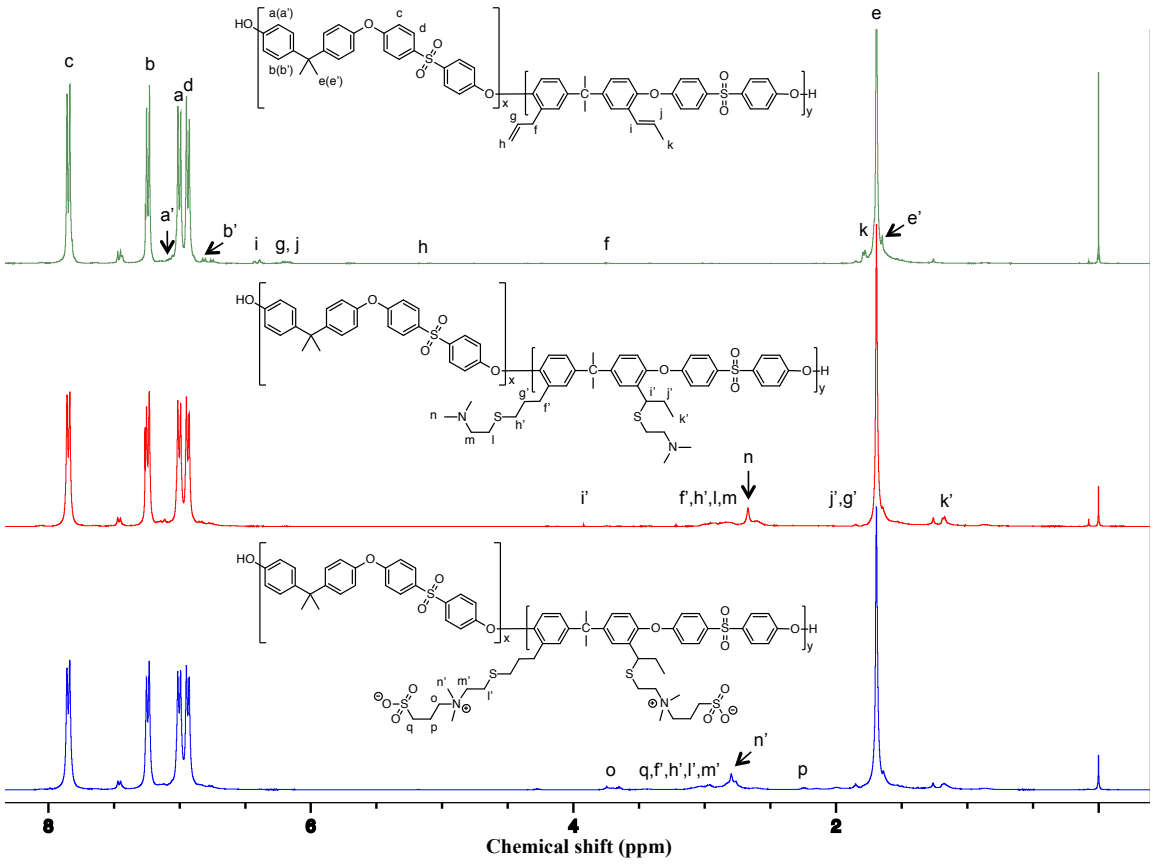

Figure 3.1. ^{1}H-NMR spectra of A-PAES copolymers (top), tertiary amine-modified

PAES (TA-PAES) copolymers (middle), and zwitterionic PAES-co-SBAES copolymers (bottom) respectively. Plots indicate successful copolymerization of PAES-co-SBAES with an SBAES content of 10% by weight.

The molecular weights of allyl-modified poly(arylene ether sulfone) copolymer (A-PAES(1) and A-PAES(2)), and corresponding zwitterionic PAES-co-SBAES (1) and PAES-co-SBAES (2) were determined with SEC (Figure 3.2, Table 3.1). First, offsetting the stoichiometry of the reacting chloride and alcohol functional groups will limit the conversion achieved, which will reduce the molecular weight. When comparing A-PAES(1) and A-PAES(2), the polymer with the offset stoichiometry displayed a longer elution time and hence a lower molecular weight. Additionally, the polymer produced from the reaction with a 1:1 stoichiometry has a Đ (M_w/M_n) approaching 2.0, while the reaction with an offset stoichiometry exhibited a lower Đ. However, substituting the zwitterionic functionality onto the polymer yielded interesting results. PAES-co-SBAES(1) still displayed a shorter elution time than PAES-co-SBAES(2) and hence a higher molecular weight. However, the SEC determined that PAES-co-SBAES(1) possessed a lower molecular weight than its precursor, A-PAES(1). Conversely, the shorter precursor, A-PAES(2) increased in molecular weight after post-polymerization functionalization to form PAES-co-SBAES(2). Two factors are potentially at play here: the polymer length and the fraction of charge. For the shorter chain (A-PAES(2)), the substituted polymer contains 20 wt% SBAES groups and, thus, the charge plays a more dominant role and causes chain extension.[152,153] However, for the longer polymer chain, the increased chain flexibility and lower charge content (10 wt%) potentially contribute to a more complicated solution conformation. In future experiments, a more thorough

understanding of the connection between charge content, chain length, and solution conformation for zwitterionic PAES will be developed. The combination of NMR spectroscopy and SEC data confirm that the copolymers were successfully synthesized and display typical step-growth polymerization behavior.

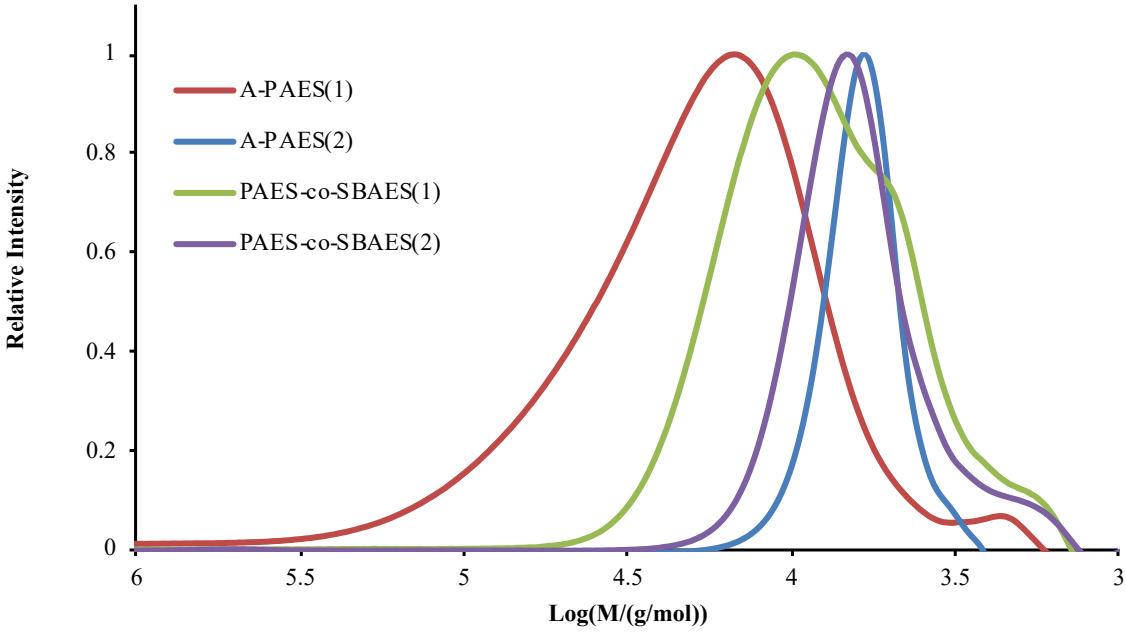

Figure 3.2. Size exclusion chromatography traces of allyl-modified poly(arylene ether sulfone) copolymer (A-PAES(1) and A-PAES(2)), and corresponding zwitterionic PAES-co-SBAES (1) and PAES-co-SBAES (2).

Table 3.1. Molecular weights of allyl-modified poly(arylene ether sulfone) copolymer (A-PAES(1) and A-PAES(2)) polymerized with different stoichiometries, and corresponding zwitterionic PAES-co-SBAES (1) and PAES-co-SBAES (2).

	Mn_{SEC} (g/mol)	Mw_{SEC} (g/mol)	Đ	Mn_{NMR} (g/mol)	DABA:BPA:DCDPS
A-PAES(1)	15,140	28,160	1.86	8,920	5:95:100
A-PAES(2)	6,230	7,720	1.24	4,500	9:81:100
PAES-co-SBAES(1)	9,770	12,500	1.28	9,370	5:95:100
PAES-co-SBAES(2)	6,760	8,650	1.28	4,950	9:81:100

3.3.2 Membrane morphology

Blended membranes containing the PAES-co-SBAES copolymer and pristine PSf homopolymers were prepared by a controlled phase inversion process. The two polymers were dissolved in THF, deposited on a glass plate using a doctor blade, partially evaporated in air, and then immersed in a coagulation bath containing deionized water to prepare asymmetric membranes (i.e., the NIPS process). To study the morphology of the membranes as a function of zwitterion content in the blend polymers, images of the cross-sectional structures of the pristine PSf (M-0) and blend membranes with varying SBAES contents were taken using SEM, as shown in Figure 3.3. Specifically, our analysis focused on the observed density and thickness of the selective layer (formed during solvent evaporation) and the porous support structure beneath (formed following immersion in the coagulation bath). As can be observed, the pristine PSf membrane M-0

displays a thick dense layer around 2 μm and few random macro-pores under the top dense layer, which can be attributed to the instantaneous demixing that occurs in the phase inversion process.[31] All of the blend membranes showed typical asymmetrical structures, consisting of a dense skin-layer on the top surface with a thickness around 100 nm and a porous sub-layer with a thickness around 15 μm. Sponge-like micro-porous structures were observed in all blend membranes, while the finger-like porous structures in the cross-section became more visible and both macro-pore size and micro-pore size became larger with the increasing zwitterion content in blend membranes. In addition, a noticeable decrease in the dense layer thickness above the porous support layer was observed after the incorporation of the zwitterion-functionalized copolymer. We propose that this was both due to 1) a reduced THF vapor pressure in the polar, hydrophilic blend solutions, thus limiting the rate of evaporation when the film is exposed to a dry atmosphere, and 2) due to a reduced viscosity of the blend solution that expedited the solvent/non-solvent exchange during the phase inversion process. The SEM images showed that the zwitterion-functionalized copolymer facilitated pore-formation during phase inversion. Blend membranes with concentration of zwitterion greater than 6 wt% were attempted, but the resulting membranes were too brittle (i.e., not free-standing) for filtration experiments. So the apparent limit of the zwitterion copolymer content in the blend membranes was around 60 wt% for the polymer used herein. We expect that this limit is based in part upon the molecular weight of the individual polymers as well as their Flory-Huggins interaction parameter, which will be the focus of subsequent investigations.

In an analogous study, we used the hydrophilic poly(ethylene glycol) (PEG,

Mn~12,000 g/mol) as an additive to PSf to prepare blend membranes (M-PEG) using the same procedure described in Section 2.4. The addition of PEG dramatically influenced the formation of pores in the support layer (Figure 3.4) due to the increased hydrophilicity and viscosity of the blend solution. These combined effects slowed the solvent/non-solvent exchange during phase inversion process, which allowed for the formation of macrovoids.

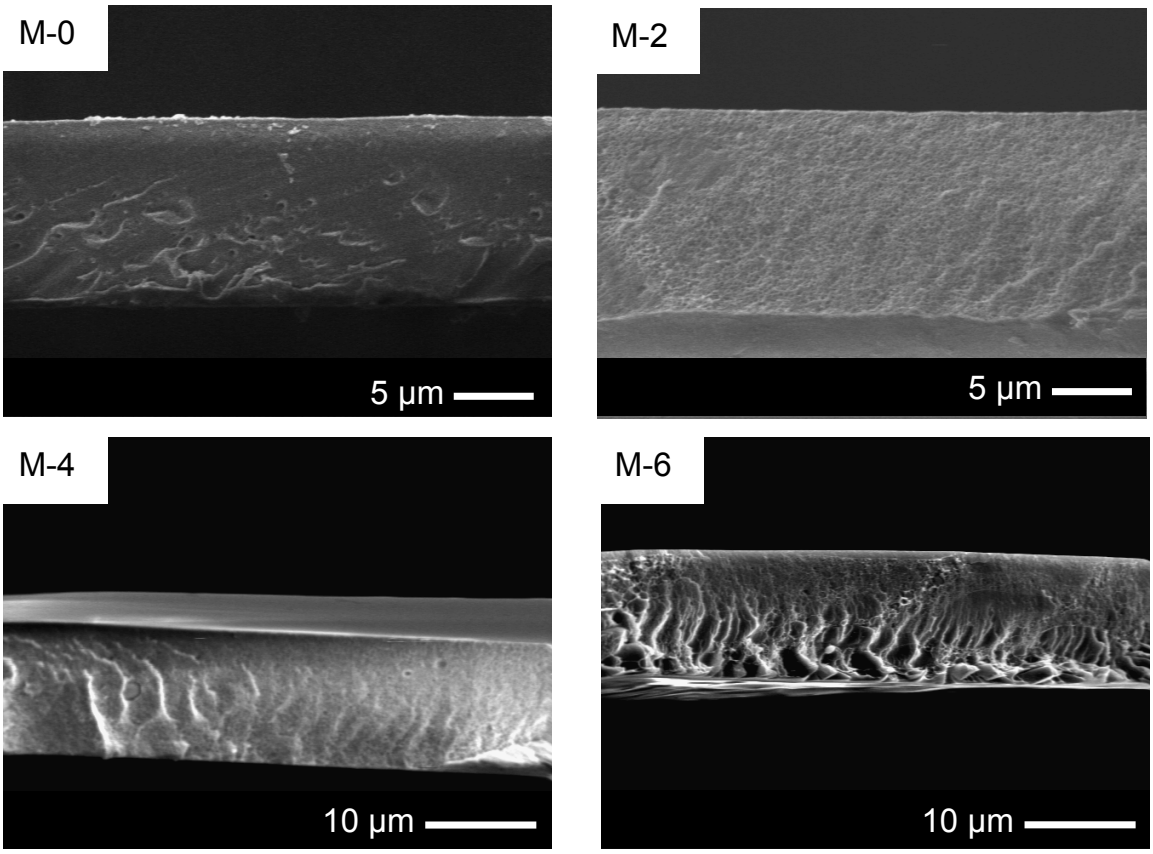

Figure 3.3. Cross-sectional SEM images of pristine PSf asymmetric membrane (M-0) and zwitterionic blend membranes with varying SBAES contents (M-2, M-4, M-6). M-0 shows a thick dense layer around 2 µm and randomly dispersed macro-pores underneath, while all the blend membranes displays a skin-layer on the top surface with thickness around 100 nm and a sponge/finger-like porous sub-layer with thickness around 15 µm. (M-0, M-2) 3500 magnification, (M-4) 2500 magnification, (M-6) 2000 magnification.

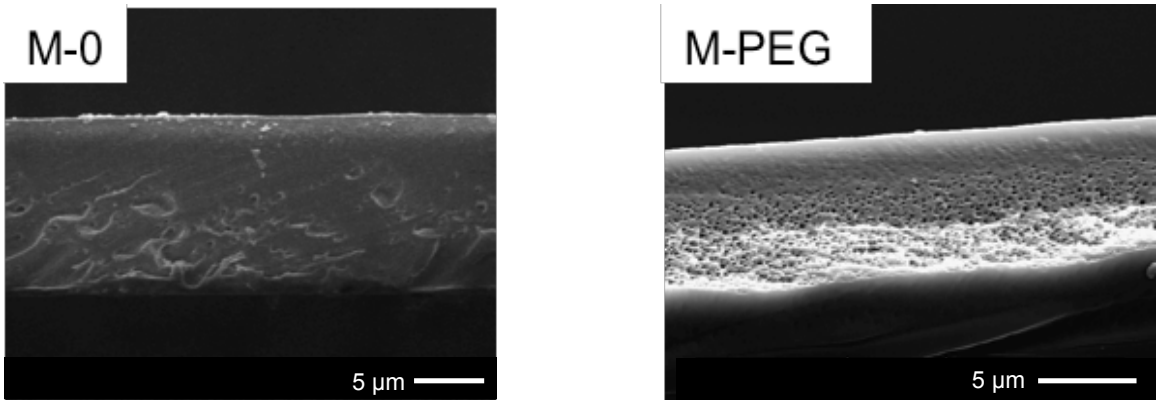

Figure 3.4. Cross-sectional scanning electron micrographs of pristine PSf membrane (M-0, left) and PSf/PEG blend membrane (M-PEG, right) with 3wt% of PEG (12,000 g/mol). M-0 shows a thick dense layer around 2 µm and randomly dispersed macro-pores underneath, and M-PEG displays a same asymmetric structure while a highly porous sub-layer with thickness around 5 µm. (M-0) 3500 magnification, (M-PEG) 5000 magnification.

3.3.3 Membrane Surface Characterizations

FT-IR spectra (Figure 3.5) showed that with increased content of zwitterion segment in the blended membranes (M-0 to M-6), there was an intensity increase of the peak at 1040 cm^{-1} attributed to the stretch vibration of the sulfonic acid group. Water contact angle (WCA) measurements were used to test the surface wettability and hydrophilicity of the membranes. As shown in Figure 3.6, the pristine PSf membrane showed the highest WCA (84 ± 2°), when compared to the WCA of the blend membranes. As expected, the WCA of the blend membranes decreased gradually with the increased amount of zwitterions in the blend membranes. It was reported that the wettability of the surface is dependent on the surface chemistry, roughness, and porosity.[142] In our case, the dense surface layer was not observed to be porous based on the AFM phase images (Figure 3.7), and the RMS roughness was measured as within 1

nm (Table 3.2.), which is much smoother than the RMS roughness of the polyamide TFC membranes (i.e. for BW30 as 68.3 nm [154]). Therefore, surface composition was the dominant factor to affect the wettability due to the initial drop in WCA from the pristine PSf membrane to that of the blend membranes. The continued decrease in WCA with added zwitterion content further substantiates the high affinity of the zwitterion functional group toward water.[155] The lower limit of WCA for the pure PAES-co-SBAES copolymer (containing 10 wt% SBAES zwitterionic segments) was also measured as the reference dashed line shown in Figure 3.6.

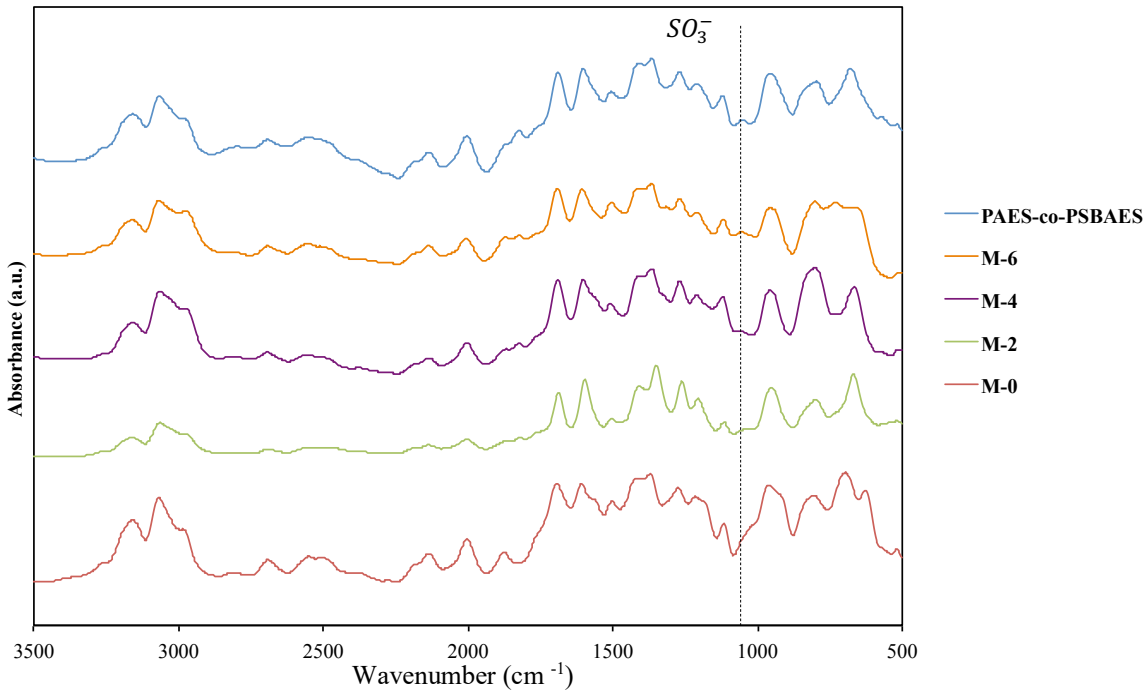

Figure 3.5. FT-IR spectra for M-0, M-2, M-4, M-6 membranes, as well as the pure PAES-co-PSBAES copolymer powder with 10 wt% of zwitterion content. An increase in zwitterion content in the blended membranes caused an intensity increase for the peak at 1040 cm^{-1} attributed to the stretch vibration of sulfonic acid group. The spectra were shifted vertically to improve clarity.

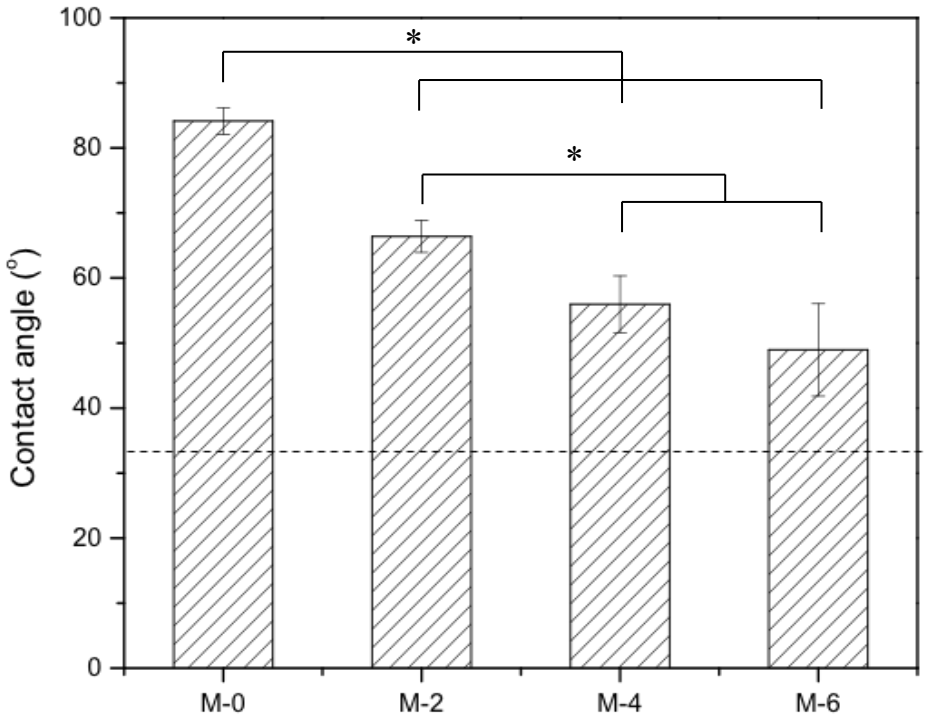

Figure 3.6. Water contact angle of the blend membranes with different SBAES contents. The dashed line indicates the water contact angle for the PAES-co-SBAES copolymer, containing 10 wt% sulfobetaine zwitterionic groups.

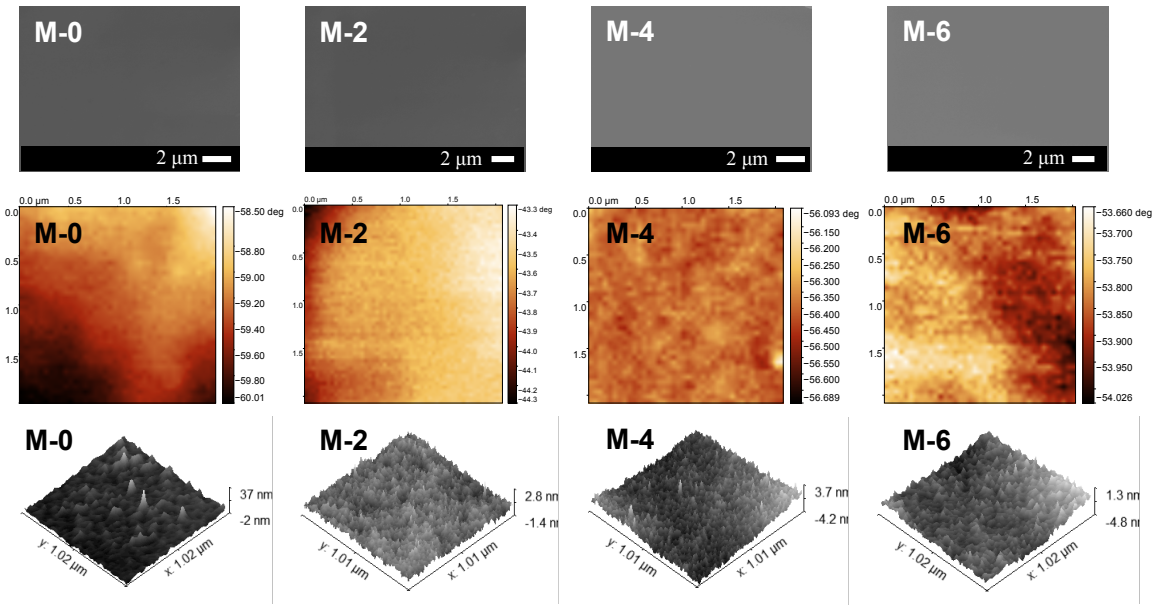

Figure 3.7. Membrane surface morphologies and surface roughness via SEM images (upper side), AFM phase images (middle) and 3D images (down side) for M-0, M-2, M-4, and M-6 membranes, respectively.

Table 3.2. Surface roughness parameter, mean-square value (RMS, or Rq), of M-0, M-2, M-4, and M-6 membranes, respectively. RMS roughness was calculated from AFM images from at least five different spots on each membrane sample.

RMS roughness (nm)			
M-0	M-2	M-4	M-6
2.95±0.97	0.41±0.04	0.96±0.30	0.82±0.18

3.3.4 Water Permeance and Salt Passage

In order to assess the membrane transport properties, dead-end stirred cell filtration experiments were performed with pure deionized water as well as sodium chloride aqueous solutions at 2.0 g/L. The membranes were pre-pressurized at 8 bar for

30 min before the filtration experiment at 8 bar. All the blend membranes showed a higher water permeance (Figure 3.8), up to 2.5 $L \cdot m^{-2} \cdot h^{-1} \cdot bar^{-1}$, when compared to the water permeance of pristine PSf membrane, which was only 0.1 $L \cdot m^{-2} \cdot h^{-1} \cdot bar^{-1}$. Furthermore, a gradual increase in water permeance was observed with the increased zwitterion content in the membranes (i.e., the water permeance for M-2 < M-4 < M-6). This finding was in agreement with the WCA measurement results discussed earlier, which decreased from 84.1° to 48.9° when the zwitterion content increased from 0 wt% to 6 wt%. Thus, the improvement in the surface hydrophilicity via the addition of the zwitterionic copolymer PAES-co-SBAES could directly enhance the pure water permeance of the membranes. Additionally, it is known that support morphology (i.e., porous layer beneath the dense active layer) could also influence the desalination membrane performance.[52,144] From the SEM images in Figure 3.3, the micro-pore size slightly increased from M-2 to M-6, while the finger-like pores became more visible at the bottom of the membranes. For the highest zwitterion content investigated, M-6, the sponge-like micro-pores were almost absent due to the presence of large, long finger-like pores. These observations correspond to the dramatic increase in water permeance shown in Figure 3.8. Especially when compared with the surface hydrophilicity of M-4, M-6 had no statistically significant decrease in terms of water contact angle, while the pure water permeance of M-6 increased dramatically due to the increase of porosity in the support layer. Therefore, the morphology here gives further proof that increased porosity of the membrane substrate layer contributes to overall membrane performance. Beyond that, the pure water permeance for native PSf membranes cast in the presence of PEG (M-PEG) was measured to be 0.14 ± 0.04 $L \cdot m^{-2} \cdot h^{-1} \cdot bar^{-1}$, and salt rejection was measured as 92.4%

± 1.4%. Compared with the filtration performance of the control membrane M-0, the M-PEG membrane showed no significant change in desalination performance due to the fact that the hydrophilic PEG molecules were extracted in the coagulation bath during the NIPS process. The comparison with the M-PEG membrane further substantiates the impact of the hydrophilic zwitterion on membrane hydrophilicity, pore formation in support layer, water permeance and salt rejection.

On the other hand, salt rejection was maintained at a high level (~98%, Figure 3.8), which is potentially applicable for brackish water desalination or nanofiltration applications. Thus, this blend membrane (without additional optimization) could be suitable as a precursor for RO-based purification.[36] The salt rejection showed no change within error margins among the blend membranes as compared with the pristine PSf membrane. This indicates that the dense selective layer formed uniformly during all membrane casting processes, despite the increased hydrophilicity and water sorption caused by the increased zwitterion content in the blend membranes. The formation of the dense selective layer was also consistent with the morphologies in SEM (Figure 3.3). In order to connect the work herein to the context of the brackish water RO desalination application, we have performed the same filtration experiments on commercial TFC RO membranes BW30. It showed (Figure 3.8) that under hydrostatic pressure of 8 bar and feed concentration of 2 g/L NaCl solution, M-BW30 had higher water permeance (3.2 $L \cdot m^{-2} \cdot h^{-1} \cdot bar^{-1}$) than M-6, but also had higher salt passage (5.2%) than the membranes herein.

Importantly, the transmembrane pressure during the dead-end filtration tests

herein was 8 bar, which is close to the current lowest feed operation pressure (6.9 bar) in commercial brackish water RO purification.[156] Despite the fact that the permeance herein is below current state-of-the-art seawater RO (SWRO) or FO desalination levels, process modeling has shown that increased water permeability would result in only negligible decreases in energy consumption and capital costs.[36,157] For example, increasing the water permeability coefficient from 3 to 10 $L \cdot m^{-2} \cdot h^{-1} \cdot bar^{-1}$ would decrease the SWRO energy requirements by less than 2%.[158] This limited difference largely stems from the single-stage operation of RO, which necessitates the use of a hydraulic pressure greater than the osmotic pressure difference between the feed and the effluent, irrespective of the membrane permeability. The use of hydraulic pressure is the main determinant of the energy used by the RO stage. Our novel blend membranes, therefore, operate at a low transmembrane pressure for desalination without a significant decrease in the transport performance. In order to connect the work herein to the context of the brackish water RO desalination application, we have performed the same filtration experiments on commercial TFC RO membranes BW30. It showed (Figure 3.8) that under hydrostatic pressure of 8 bar and feed concentration of 2 g/L NaCl solution, M-BW30 had higher water permeance (3.2 $L \cdot m^{-2} \cdot h^{-1} \cdot bar^{-1}$) than M-6, but also had higher salt passage (5.2%) than the membranes herein, which was induced by the lower operation pressure herein than the standard pressure condition (225 psi, ~15.5 bar). It should be noted that the use of a blend membrane containing pristine PSf and the zwitterion-functionalized PSf dilutes the charge content, which based on our results limits the water permeability achievable. Thus, future work will focus on optimizing the polymer properties (molecular weight and charge content) to further improve the water treatment performance.

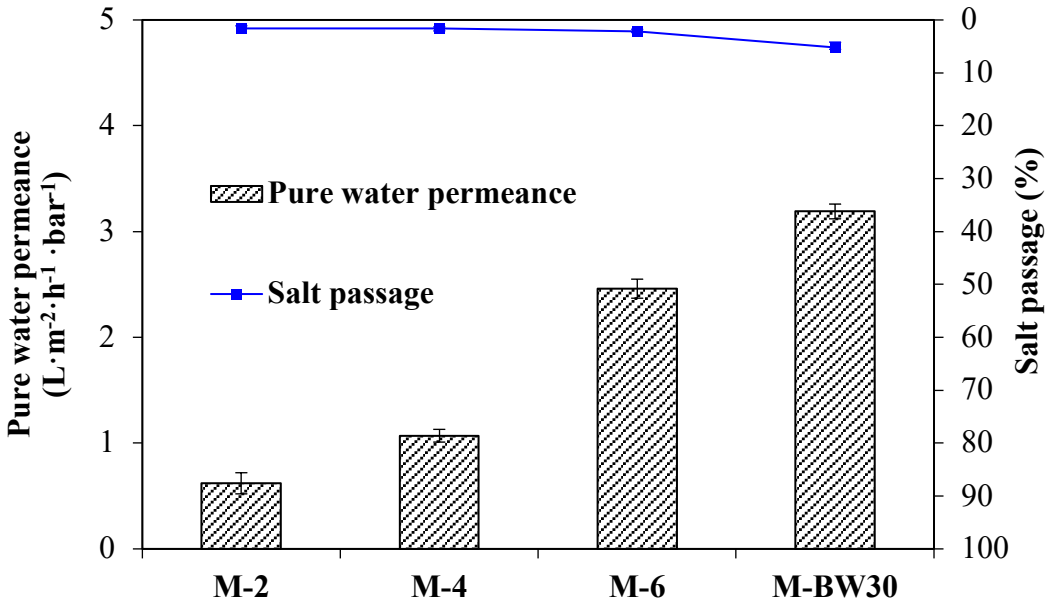

Figure 3.8. Effect of SBAES content on desalination performance for asymmetric membranes. The membranes were challenged with 2.0 g/L NaCl aqueous solution at a transmembrane pressure drop of 8 bar and a temperature of 25 °C. Data points along the top indicated salt passage (%), while the bars below indicated pure water permeance.

3.3.5 Anti-fouling Performance

Minimizing the adsorption of organic foulants and microorganisms to membrane surfaces can substantially reduce energy consumption and save costs during membrane-based desalination.[32] Zwitterionic polymers have been widely recognized for their ability to prevent the adhesion of organic molecules and bacteria on surfaces.[159–163] We tested the anti-fouling property of both PSf/PAES-co-SBAES blend membranes (M-4) and commercial M-BW30. To avoid the formation of a cake layer of large organic matter in the static filtration system, we performed the protein filtration experiments with a cross-

flow system with a solution of 0.1 g/L BSA in pH 7.0 at 200 psi and 25 °C for 12 h. The zwitterion prevented adhesion, as shown (Figure 3.9) by the high flux recovery ratio (94%) after rinsing the membranes with deionized water for 3 h. In comparison, the commercial TFC membrane (M-BW30) displayed a flux recovery ratio of only 86% after rinsing with deionized water using the same procedure. This experiment illustrated that the irreversible fouling of protein on the zwitterionic copolymer blended membrane (M-4 as of 7%) was much lower that of the current PA TFC membrane (M-BW30 as of 14%), which attributed to the antifouling nature of the amphiphilic surface and relatively low surface roughness (see analysis in Section 3.2.2).

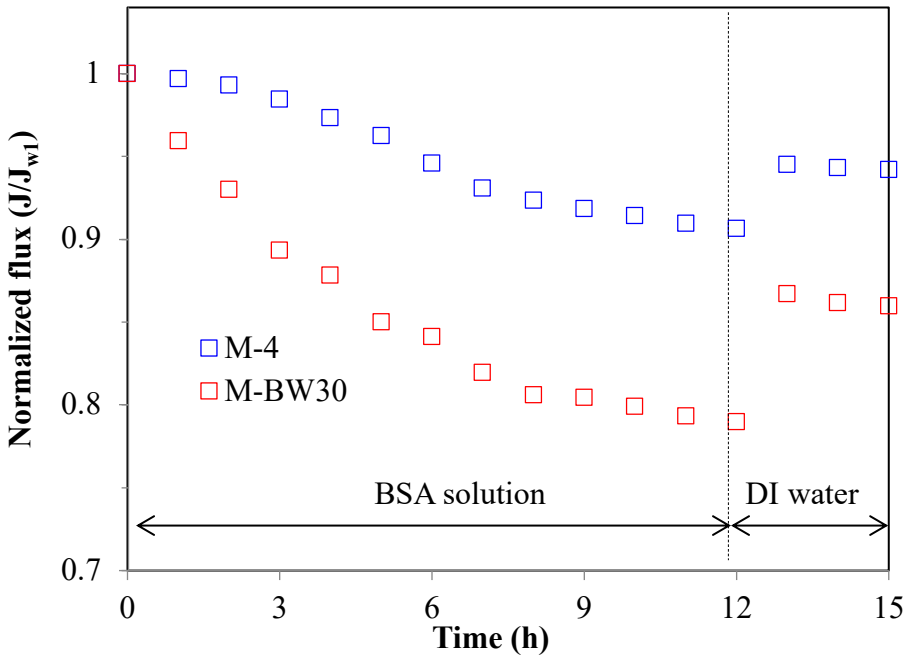

Figure 3.9. The variation of normalized water flux of M-4 and M-BW30 tested at a hydrostatic pressure drop of 200 psi, a temperature of 25 °C, challenged with a feed solution of 0.1 g/L of BSA at pH 7.0. The membranes were rinsed with deionized water for 3 h after 12 h of protein filtration, and the time was not counted in the filtration

process. Pure water flux was recorded for another 3 h after the membrane rinsing.

To further study the fouling resistance of the zwitterion-containing blend membrane, we exposed both an allyl-containing PAES/PSf blend membrane (M-A) and a zwitterionic PSBAES/PSf blend membrane (i.e. M-6) to a solution of FITC-BSA (0.05 mg/mL) in PBS at pH 7.4 for 3 h in the dark. The two blend membranes contained the same weight percent concentration of native PSf. The change in fluorescence intensity between the membranes exposed to PBS alone versus the FITC-BSA solutions is attributed to the adsorption of the fluorescent FITC-BSA onto the membranes. The intensity of fluorescence was quantitatively measured using ImageJ software. The M-A before exposure to FITC-BSA displayed a low fluorescence intensity (Figure 3.10a) commonly observed for poly(arylene ether sulfone) backbones,[164–166] while a highly increased fluorescence intensity was observed after exposure to the FITC-BSA solution (Figure 3.10b). Conversely, the SBAES-containing blend membrane (M-6) (Figure 3.10c, d) showed a very small fluorescence intensity change, thus very little adsorption of BSA was observed. This observation, summarized in Figure 3.11 as the relative change in fluorescence intensity, further proves the strong hydration capability of the zwitterionic copolymers and their ability to effectively prevent the adhesion of BSA.[38,167,168]

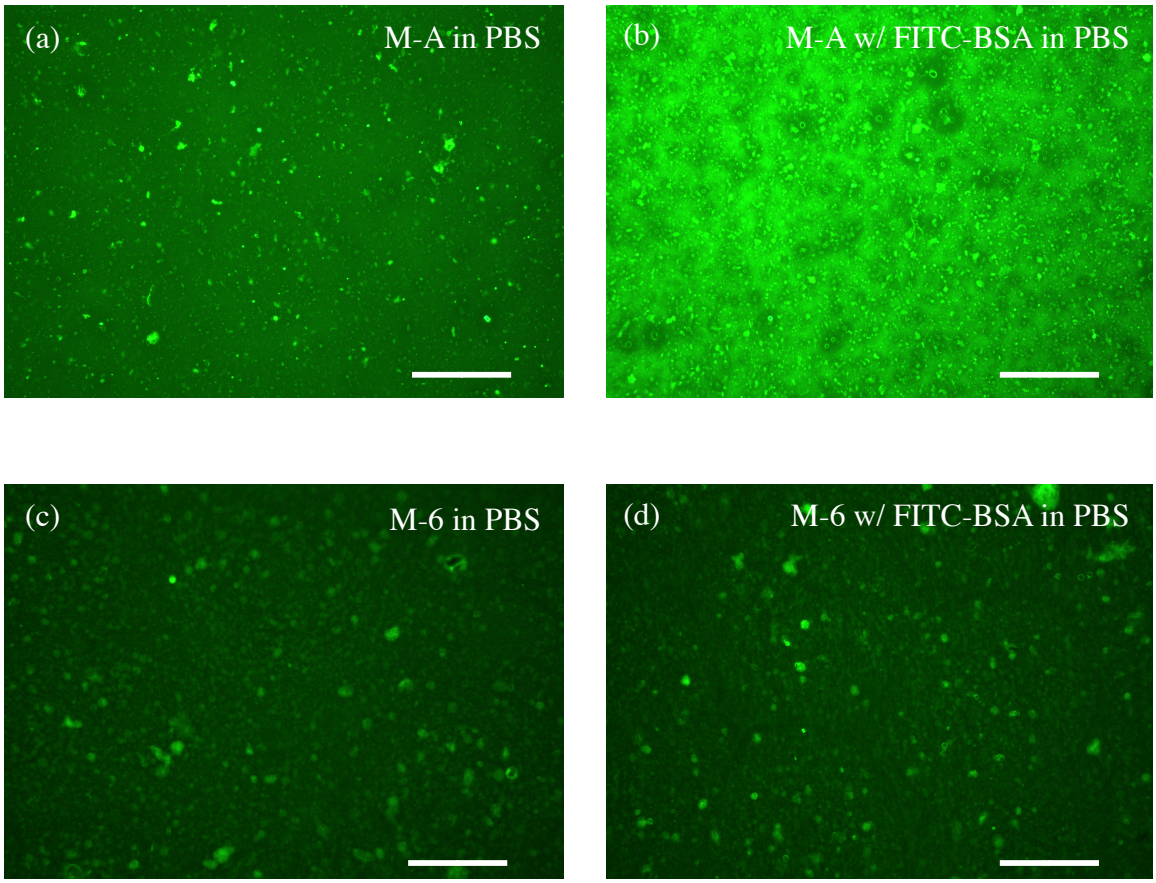

Figure 3.10. Epifluorescence microscope images of allyl-containing PAES/PSf blend membrane (M-A) and zwitterionic PAES/PSf blend membrane (M-6) following protein adhesion tests using fluorescein-conjugated BSA (FITC-BSA) in PBS with pH 7.4. M-A and M-6 exposed in PBS without (a) (c) and with FITC-BSA (b) (d), respectively. The scale bar is 100 μm.

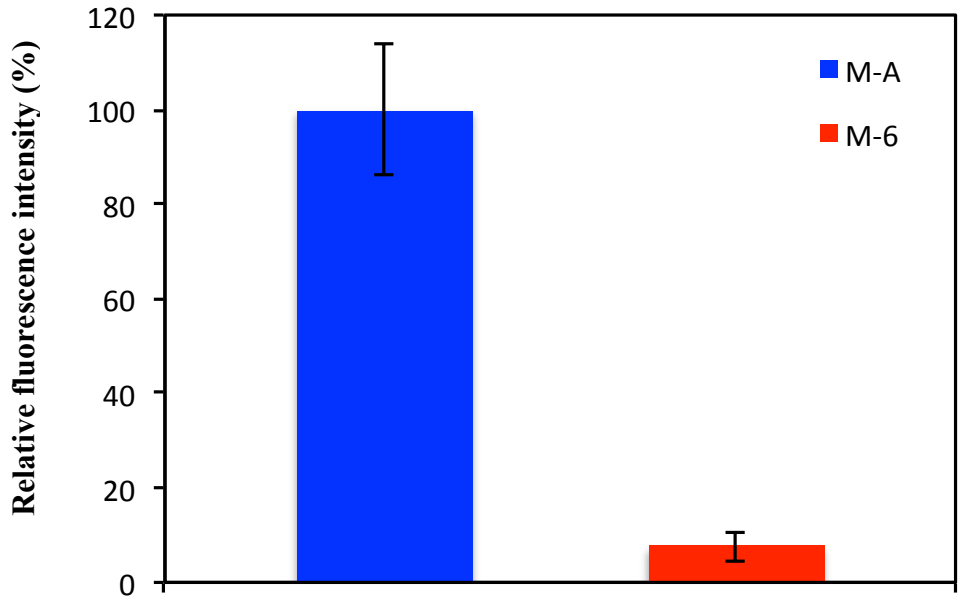

Figure 3.11. The bar graph shows the relative increase in fluorescence intensity for M-A (blend membrane containing PSf and A-PAES) and M-6 (blend membrane containing PSf and PAES-co-SBAES), respectively, after exposure to FITC-BSA. The fluorescence intensity was analyzed using ImageJ software.

3.3.6 Chemical Stability

It is widely accepted that PA-membranes exhibit a poor resistance to chlorine-mediated degradation, either due to oxidation or hydrolysis, which causes chain cleavage and other detrimental effects. In turn, the performance of PA membranes decays when exposed to oxidizing species, which limits their lifetime and increases operation costs.[43,51,169,170] To confirm the advantage of our polysulfone based blend membranes, we tested (as shown in Figure 3.12) the M-2 membrane's chlorine resistance at a 1000 ppm chlorine solution in pH of 7.1 for up to 12 h. The M-2 membrane remained the stable desalination performances until after 8000 ppm•h of chlorine exposure. Comparatively, the desalination performances of M-BW30 started to drop immediately after exposure to

chlorine (1000 ppm). Therefore, these results demonstrate the chlorine resistance that has come to be expected of PAES-based membranes.

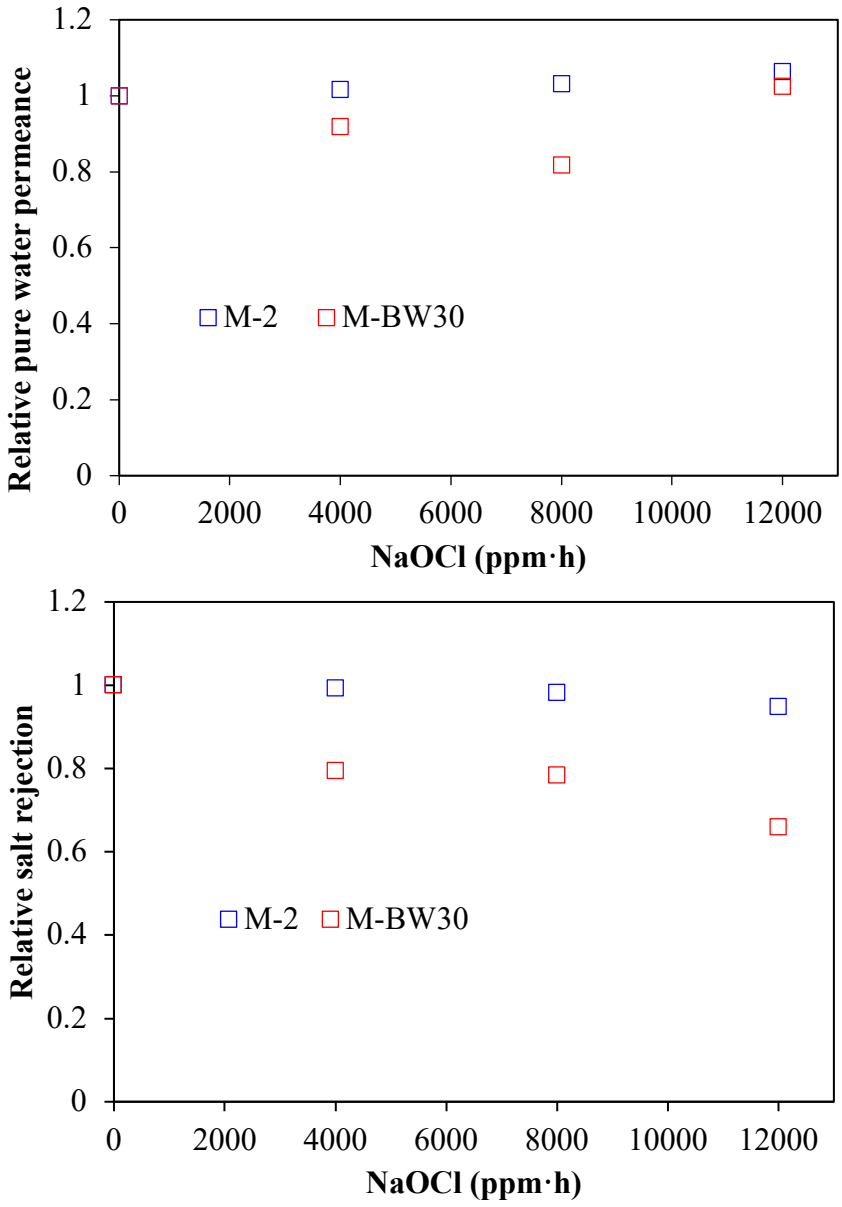

Figure 3.12. Membrane stability tests for M-2 (native PSf blended with PAES-co-PSBAES) with 2 wt% zwitterion content in the blended membrane and commercial TFC membrane BW30. After soaking the membrane in a chlorine solution (experimental details are in the main text), no loss in water permeance or salt rejection was observed until after 8000 ppm•h chlorine exposure.

3.4 Conclusions

In summary, a class of novel, fouling resistant polysulfone-based desalination membrane incorporating the zwitterionic copolymer PAES-co-SBAES into PSf was fabricated by NIPS. The SBAES segments improved the membrane surface hydrophilicity, increased porosity in support layer, and maintained a mechanically strong matrix to enable the preparation of free-standing membranes. The water permeance and fouling resistance properties of the PSf/PAES-co-SBAES blend membranes increased drastically compared to the unmodified PSf (~25x increase in water permeance and 94% flux recovery), and salt rejection was maintained at a high level (98%). Additionally, the membranes were resistant towards oxidative degradation caused by exposure to chlorine solutions. In summary, the easy synthesis, membrane fabrication–both scalable to high production capacities–and the membrane performance point towards potential materials for nano- or microfiltration, brackish water desalination, or hydrophilic membrane supports.

Chapter 4. Poly(arylene ether sulfone)s polycondensation Reaction: Kinetics and Mechanism

To be submitted as

Yi Yang, Christopher L. Muhich, Matthew D. Green, "Kinetics and Mechanisms of Polycondensation Reactions Between Aryl Halides and Bisphenol A".

4.1 Introduction

The most widely used synthetic method to produce PAES for industrial and research purposes [52,57,60–69] consists of polycondensation reactions of bisphenols with 4,4'-dichlorodiphenyl sulfone (DCDPS) or with 4,4'-difluorodiphenyl sulfone (DFDPS) in an aprotic polar solvent such as DMSO using K_2CO_3 as the base (Scheme 4.1).[70–72] The mechanism behind this polycondensation reaction is widely accepted as a classical S_NAr, in which the aryl halide is activated toward nucleophilic attack by an electron withdrawing group.[73,74] In S_NAr reactions, the rate limiting step is typically the formation of the resonance-stabilized anionic intermediate, Meisenheimer complex[76] (Scheme 4.2, 4.3), for which the reactivity of the aryl halide decreases in the order F≫Cl>Br>I based on the electronegativity of the halogen.[73] Thus, it is rational to assume that the S_NAr reaction for any aryl dihalide monomer and phenol-based nucleophile would follow a second order rate law.[74] Interestingly, in our present work, the order of the reaction for the alkyl fluoride monomer (i.e. DFDPS) was different than that for the alkyl chloride monomer (i.e. DCDPS). As expected, the reaction rate of the polymerization using the DFDPS monomer was significantly higher than that of DCDPS monomer under identical experimental conditions. Ross and co-workers have thoroughly studied the base-catalyzed S_NAr mechanism in the reaction of 2,4-dinitrochlorobenzene and allylamine, which was self-catalyzed by both the aromatic nitro and amine groups.[171–173] They showed that the reaction kinetics fit a third-order rate expression. A computational study[174] showed further evidence of base-catalyzed

Meisenheimer complex formation by the binding of the metal cation from the base with the fluoride leaving group to facilitate displacement. However, the influence of the monomer interactions with the base on the rate law order in polycondensation reactions of different aryl halides has not been systematically studied using both experimental and computational techniques. In the present work, we systematically compared the kinetics of DFDPS/BPA and DCDPS/BPA reactions during PAES synthesis, by which surprisingly a new piece of puzzle on fundamental understanding of the polycondensation mechanisms in different aryl halide monomer systems was revealed.

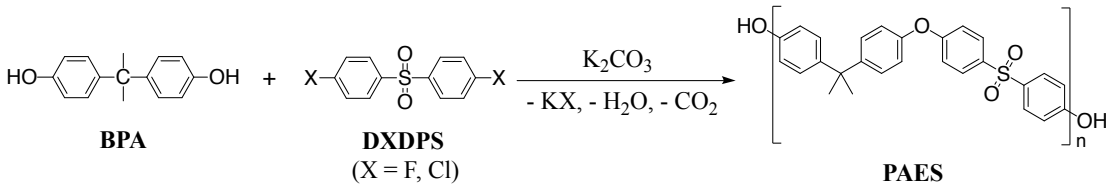

Scheme 4.1. Typical polycondensation route to prepare poly(arylene ether sulfone)s.

4.2 Experimental

4.2.1 Materials and reagents

4,4'-Dichlorodiphenyl sulfone (DCDPS, 98%) was purchased from Sigma-Aldrich and recrystallized from diethyl ether before use. 4,4'-Difluorodiphenyl sulfone (DFDPS, >98%) was purchase from Thermo Fisher Scientific Chemical and recrystallized from diethyl ether before use. Bisphenol A (BPA, ≥99%) was purchased from BDH® VMR analytical and recrystallized from acetic acid/water (1:1 v/v) before use. THF and toluene (99.8%) were purchased from Sigma-Aldrich and used after passing through M. Braun SPS-800 solvent purification system. Dimethylsulfoxide (DMSO, anhydrous, ≥99.9%) was purchased from Sigma-Aldrich and used as received.

Potassium carbonate (K_2CO_3, ≥98%) and sodium carbonate (Na_2CO_3, ≥98%) were purchased from Sigma-Aldrich and vacuum dried overnight before use. Deuterated chloroform ($CDCl_3$, 99.8 atom% D, 0.03% (v/v) TMS) was purchased from BDH® VMR analytical and used as received.

4.2.2 Synthesis of poly(arylene ether sulfone)s

The poly(arylene ether sulfone)s (PAES) were synthesized via traditional polycondensation reaction. One kinetic study of DCDPS/BPA system is provided as an example. BPA (1.049 g, 4.605 mmol), DCDPS (1.406 g, 4.899 mmol), K_2CO_3 (0.667 g, 4.835 mmol) were added to a three-neck, 250-mL flask equipped with a condenser, Dean Stark trap, nitrogen inlet/outlet, and a mechanical stirrer. DMSO (24 mL) and toluene (6 mL) were added to the flask to dissolve the monomers. The solution was heated under reflux at 140 ˚C for 1~6 h until the toluene-water azeotrope and toluene was completely removed from the reaction mixture. The reaction continued for 48 h at 140 ˚C. The reaction mixture was cooled to room temperature and filtered to remove the precipitated salt. Then the clear solution was diluted with THF, passed through a 0.45 μm Teflon® filter, and precipitated by addition to stirring DI water. The polymer was filtered and dried under vacuum at 100 ˚C for 24 h.

4.2.3 Polymer structure characterizations

^{1}H-NMR spectroscopy was performed on a Varian 400 MHz spectrometer using deuterated chloroform (CDCl3) to analyze the polymer's chemical structure. Samples contained 20 mg of dried polymer dissolved in CDCl3. The chemical shifts are given in

ppm downfield from tetramethylsilane (TMS).

In order to determine the molecular weight of the copolymers, size exclusion chromatography (SEC) was performed using a Waters Alliance e2695 HPLC system, with Styragel® HR5 and HR4 7.8×300mm (THF) columns in series, interfaced to a light scattering detector (miniDAWN TREOS) and an Optilab T-rEX differential refractive index (dRI) detector. The mobile phase was THF Optima (inhibitor-free) at a flow rate of 1.0 mL min^{-1}, and samples were calibrated against Pressure Chemical Company low dispersity polystyrene standards of 30 kDa and 200 kDa using Astra v6.1 software. Then, ~1.0 mg mL^{-1} filtered solutions of polymer in THF were prepared for SEC.

4.2.4 Computational investigations (contributed from efforts of Prof. Christopher L. Muhich)

Density functional theory (DFT) calculations using the M06-2X functional, a 6-311G**(+) basis set, and DMSO implicit solvent were used to calculate the reaction mechanism of the Aryl halide condensation reaction through both second and third order mechanisms. Truncated monomers were used to represent the polymer, as shown in Figure 4.11, with Na rather than K to save computational time.

4.3 Results and Discussion

4.3.1 Off-set stoichiometry effects on molecular weight

After synthesis of the PAES homopolymers, the chemical structure was first confirmed via ^{1}H-NMR spectra (Figure 4.1) before the following works.

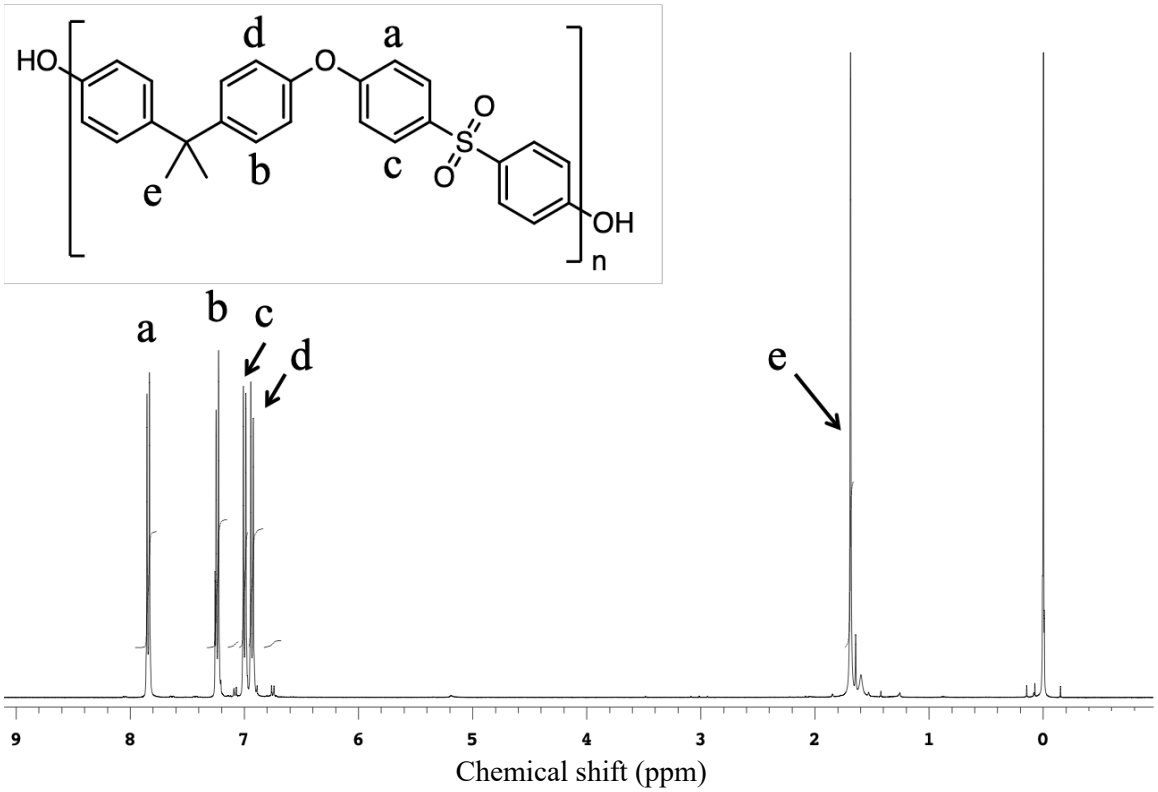

Figure 4.1. ^{1}H-NMR spectra ($CDCl_3$, 400 MHz) of a representative poly(arylene ether sulfone).

In a polycondensation reaction between bifunctional A-A and B-B monomers where the stoichiometric ratio (r) is 1:1, the Carothers equation predicts an infinite degree of polymerization and molecular weight.[175–177] However, in the present work, high molecular weight was not achieved at a 1:1 stoichiometry. To determine the optimal non-stoichiometric ratio to achieve high molar mass polymers, therefore, we first conducted a series of polycondensations of BPA and DCDPS, as well as BPA and DFDPS at various molar ratios. Initial reactions were performed on DCDPS and BPA system and are shown in Figure 4.2a. When DCDPS and BPA reacted at 180 ˚C for 48 h with a stoichiometric ratio (r = 1), a number average molecular weight (Mn) of 17.3 kDa and molecular weight

distribution (Đ) of 1.21 was obtained, which is much lower than a Đ of 2.0 for a polycondensation product at full conversion. An excess of DCDPS was then fed to the reaction under identical reaction conditions (i.e., solvent/monomer concentration, temperature), and the highest molecular weights were observed at r = 0.94 ~ 0.97. In this case, an excess of DCDPS has the consequence that monomers or oligomers have two ArCl end groups. We predict that a fraction of the excess –Cl group is hydrolyzed to a –OH group, which achieves a 1:1 stoichiometry in situ allowing for complete conversion and a high molecular weight. The same phenomenon, an increased Xn via stoichiometric imbalance, was observed in the polymerization with DFDPS (Figure 4.2b, at 140 ˚C for 4 h), where the highest Mn (33 kDa) and PDI (1.93) was observed at r = 0.94. Thus, an optimal stoichiometry ratio of 1:0.94 DXDPS:BPA was utilized for all systems in the following kinetics study.

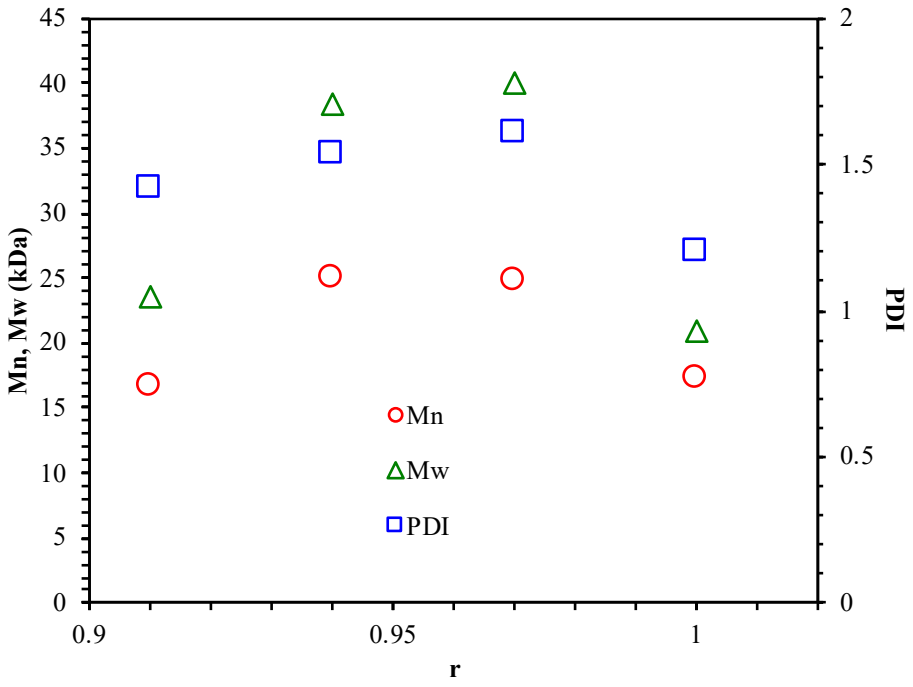

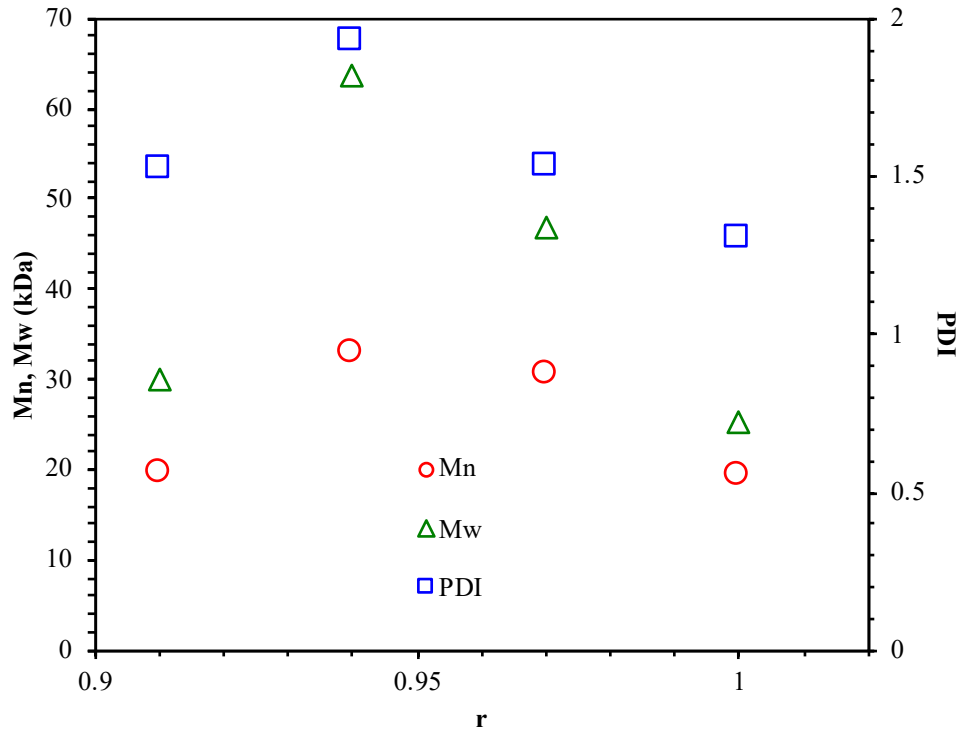

Figure 4.2. The surprising effect of DXDPS:BPA stoichiometry on the molecular weight and Đ obtained during polycondensations: (a) DCDPS/BPA at 180 ˚C for 48 h, and (b) DFDPS/BPA at 140 ˚C for 4 h.

4.3.2 Kinetics of DCDPS/BPA and DFDPS/BPA polycondensation reactions

The reaction conversion for each aryl halide was monitored as a function of time. Aliquots were collected from the reactor until the reaction reached completion, molecular weight were monitored via SEC (shown in Figure 4.3 and Figure 4.4, respectively). The number averaged molecular weight vs. reaction conversion plots (Figure 4.5) indicated that DCDPS/BPA system and DFDPS/BPA system showed typical step-growth polymerization behavior. The reaction conversion for each aryl halide was monitored as a function of time (Figure 4.6). Importantly, it took around 4 h for the DFDPS/BPA polycondensation to reach the high conversion plateau, while the DCDPS/BPA reaction took up to 48 h under identical experimental conditions. Next, the conversion data was

linearized using integer rate law expressions. The DCDPS/BPA polymerization showed linearity when fit with a second order rate expression, as seen in Figure 4.7a. This corroborates previous literature[63] that describes the mechanism of the condensation polymerization to form PAES via the S_NAr mechanism (Scheme 4.2). In the DFDPS/BPA reaction, the reaction rate constant is significantly higher than that of the DCDPS/BPA system under identical experimental conditions due to the relatively higher electronegativity and smaller size of fluorine.[62] Interestingly, the DFDPS/BPA polymerization has a reaction order higher than second order (Figure 4.7b). Viswanathan and McGrath[178] studied the reaction of DCDPS/BPA in DMAc/K_2CO_3. They observed non-linear kinetics when plotting versus 1/C with an apparent reaction order less than 2. They rationalized this result based on the partially heterogeneous nature of K_2CO_3. In the present work, however, a linear second order kinetic plot was observed in the DCDPS/BPA reaction, while the DFDPS/BPA reaction displayed a reaction order > 2. Therefore, the mechanism for the DFDPS/BPA polycondensation is independent of the limited solubility of K_2CO_3 and is different than the classical S_NAr mechanism of the DCDPS/BPA reaction.

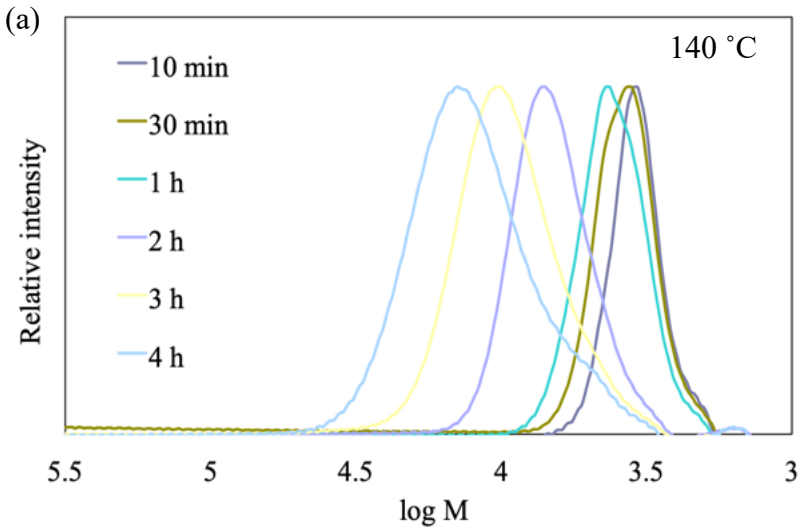
(a)
140 ˚C
10 min
30 min
1 h
2 h
3 h
4 h
Relative intensity
5.5
5
4.5
4
3.5
3
log M

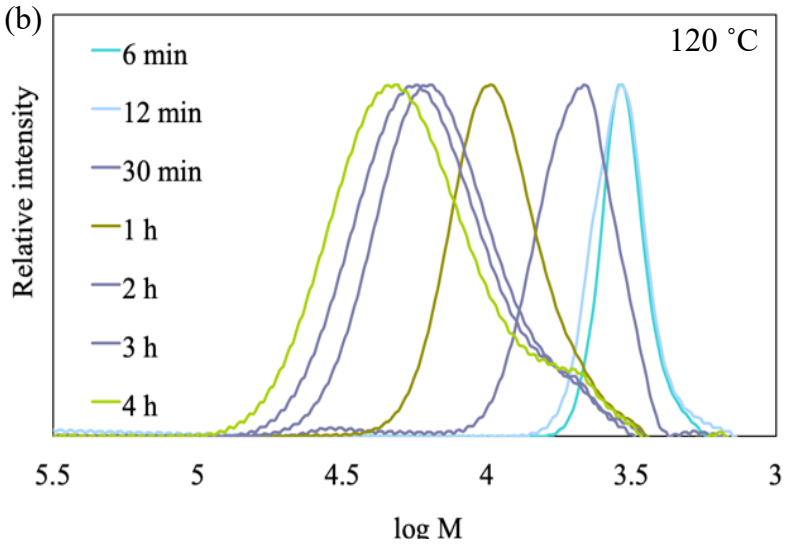
(b)
120 ˚C
6 min
12 min
30 min
1 h
2 h
3 h
4 h
Relative intensity
5.5
5
4.5
4
3.5
3
log M

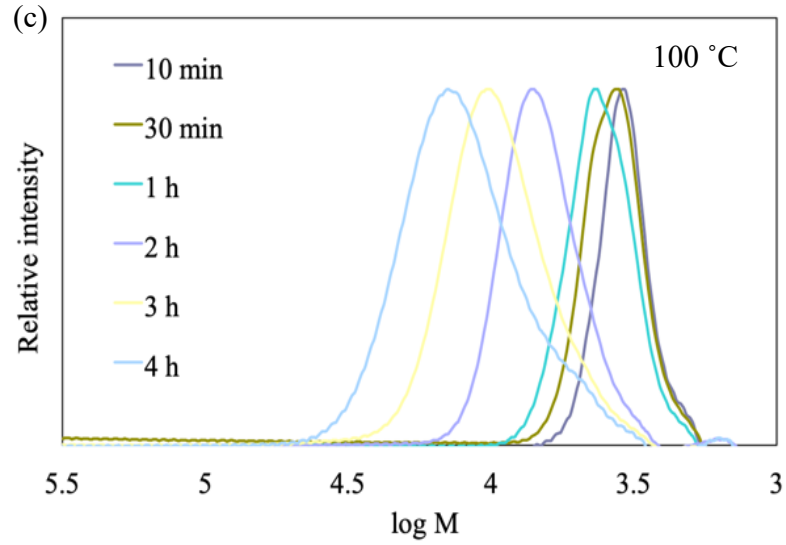
(c)
100 ˚C
10 min
30 min
1 h
2 h
3 h
4 h
Relative intensity
5.5
5
4.5
4
3.5
3
log M

Figure 4.3. Size exclusion chromatography traces of poly(arylene ether sulfone)s from DFDPS/BPA polycondensation reactions with potassium carbonate as the base as a function of time at (a) 140 ˚C, (b) 120 ˚C, and (c) 100 ˚C.

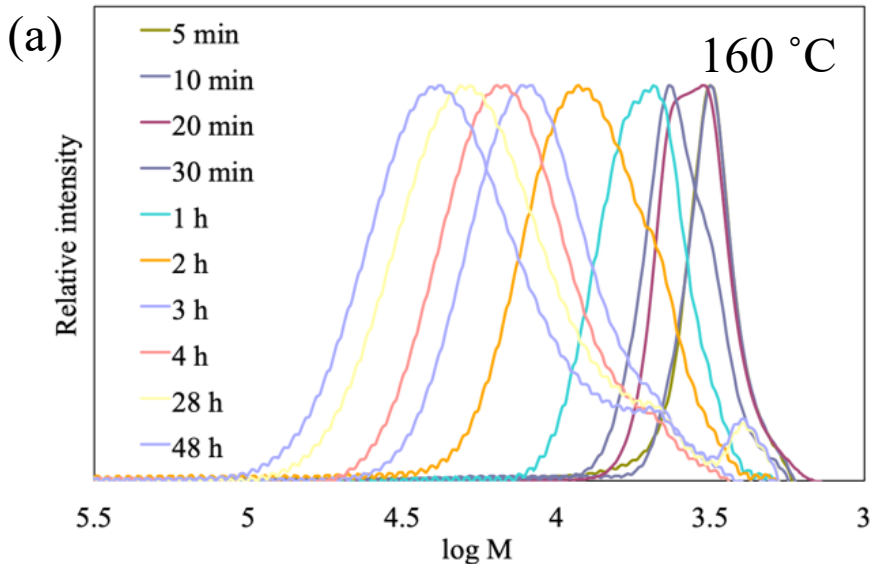

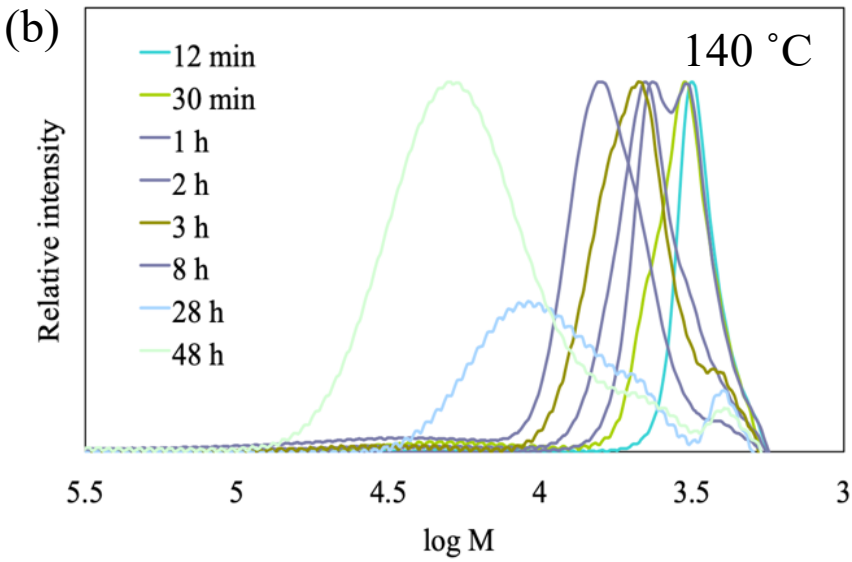
(b)
140 ˚C
12 min
30 min
1 h
2 h
3 h
8 h
28 h
48 h
Relative intensity
5.5
5
4.5
4
3.5
3
log M

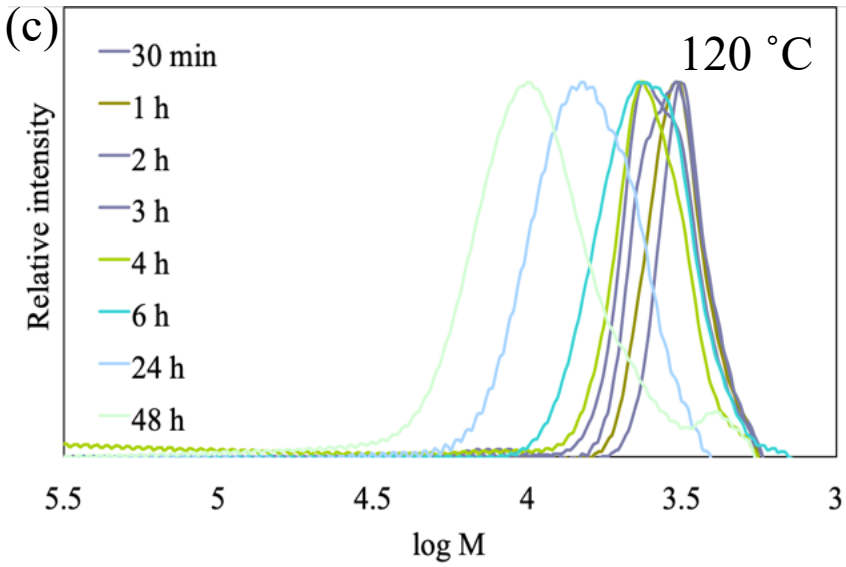
(c)
120 ˚C
30 min
1 h
2 h
3 h
4 h
6 h
24 h
48 h
Relative intensity
5.5
5
4.5
4
3.5
3
log M

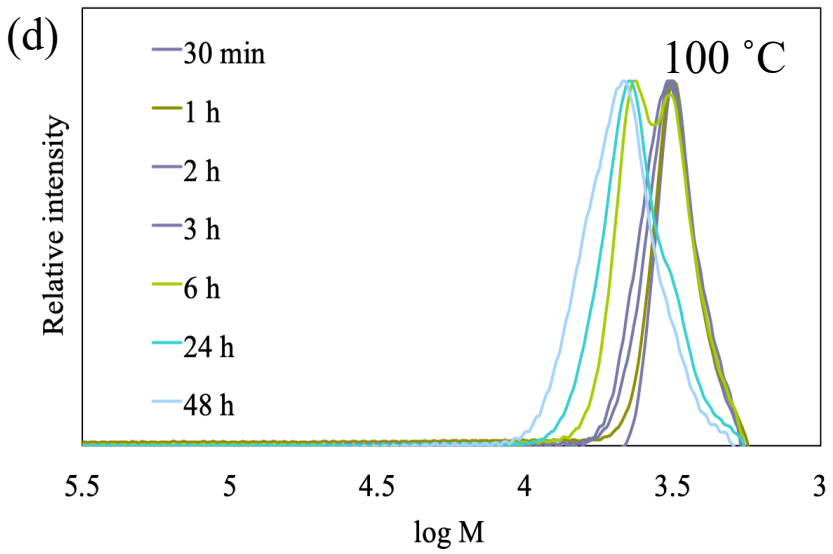

Figure 4.4. Size exclusion chromatography traces of poly(arylene ether sulfone)s from the DCDPS/BPA polycondensation with potassium carbonate as the base as a function of time at (a) 160 ˚C, (b) 140 ˚C, (c) 120 ˚C, and (d) 100 ˚C.

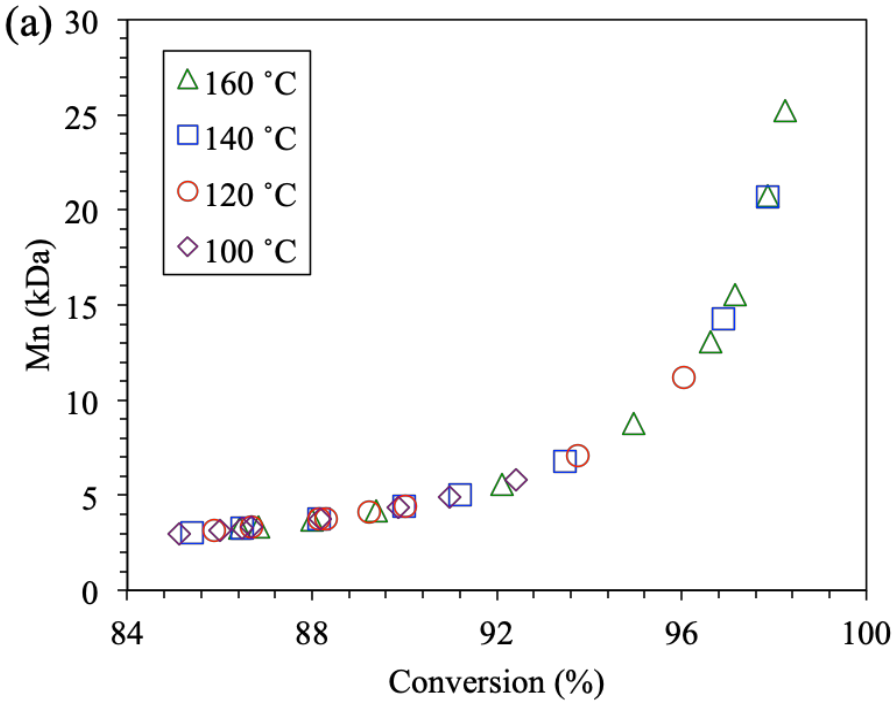

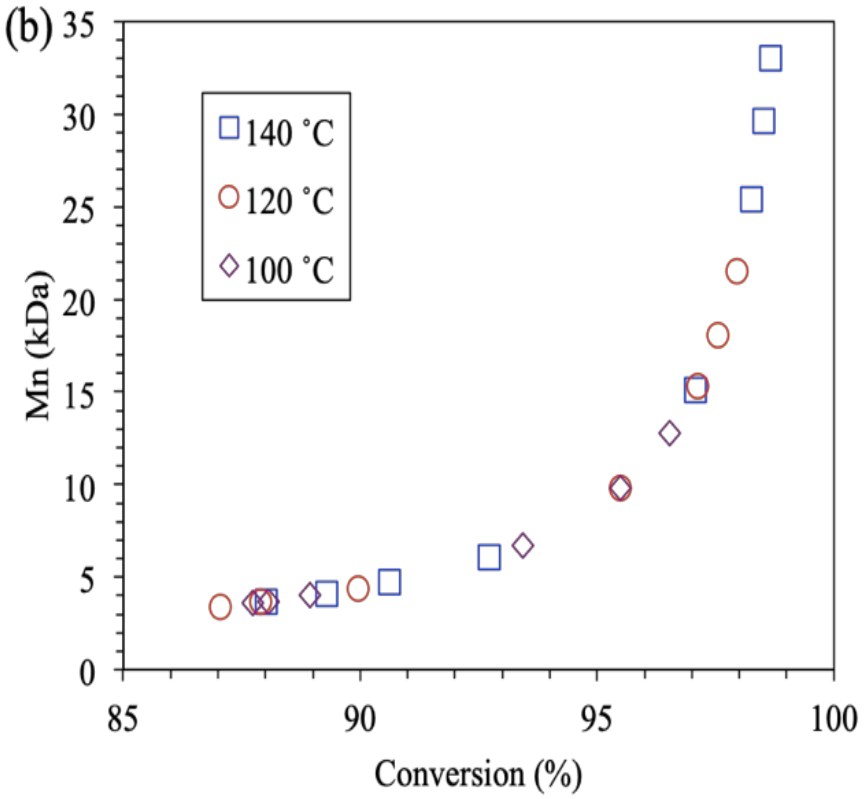

Figure 4.5. Number average molecular weight (Mn) vs. reaction conversion plots for the polycondensation of: (a) DCDPS/BPA, and (b) DFDPS/BPA at various temperatures with potassium carbonate as the base. The plots in both DCDPS/BPA system and DFDPS/BPA system showed typical step-growth polymerization behavior.

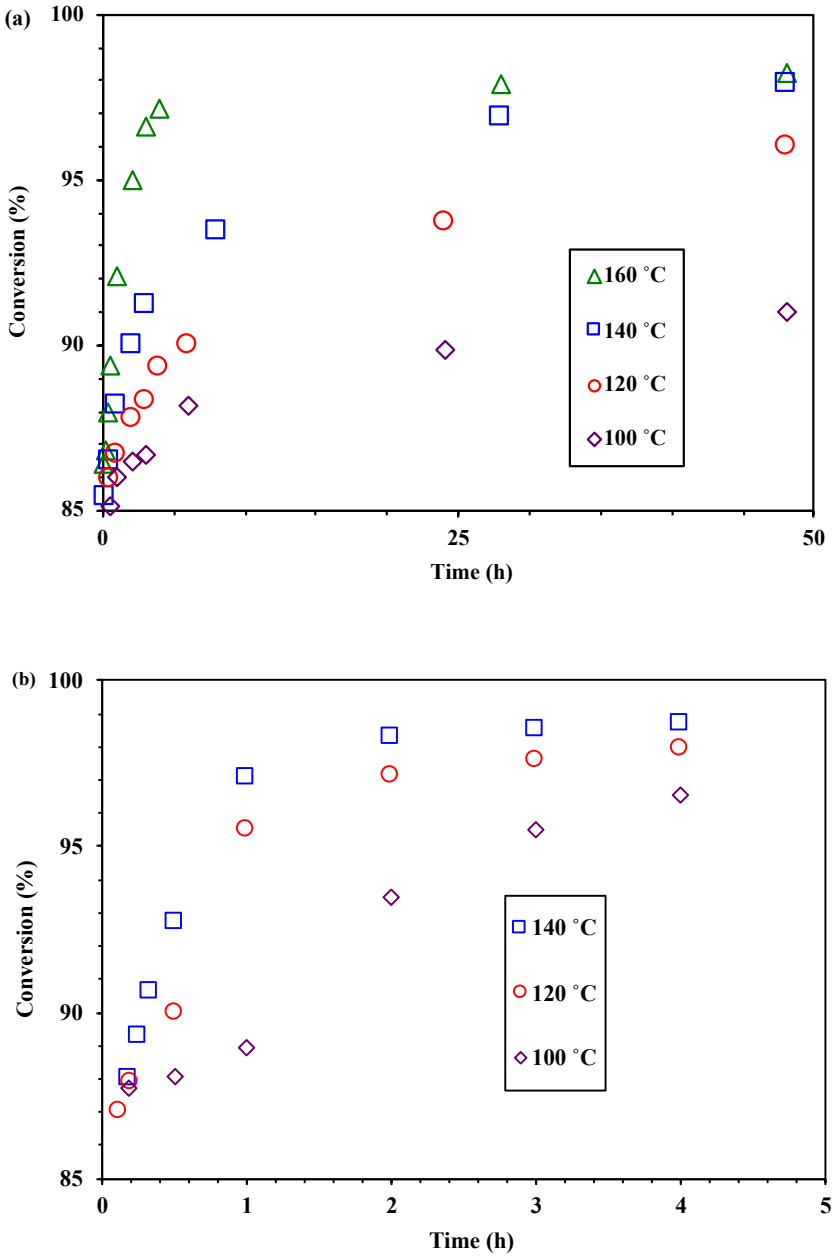

Figure 4.6. Plots of conversion vs. reaction time for the polycondensation of: (a) DCDPS/BPA, and (b) DFDPS/BPA at various temperatures with potassium carbonate (K2CO3) as the base.

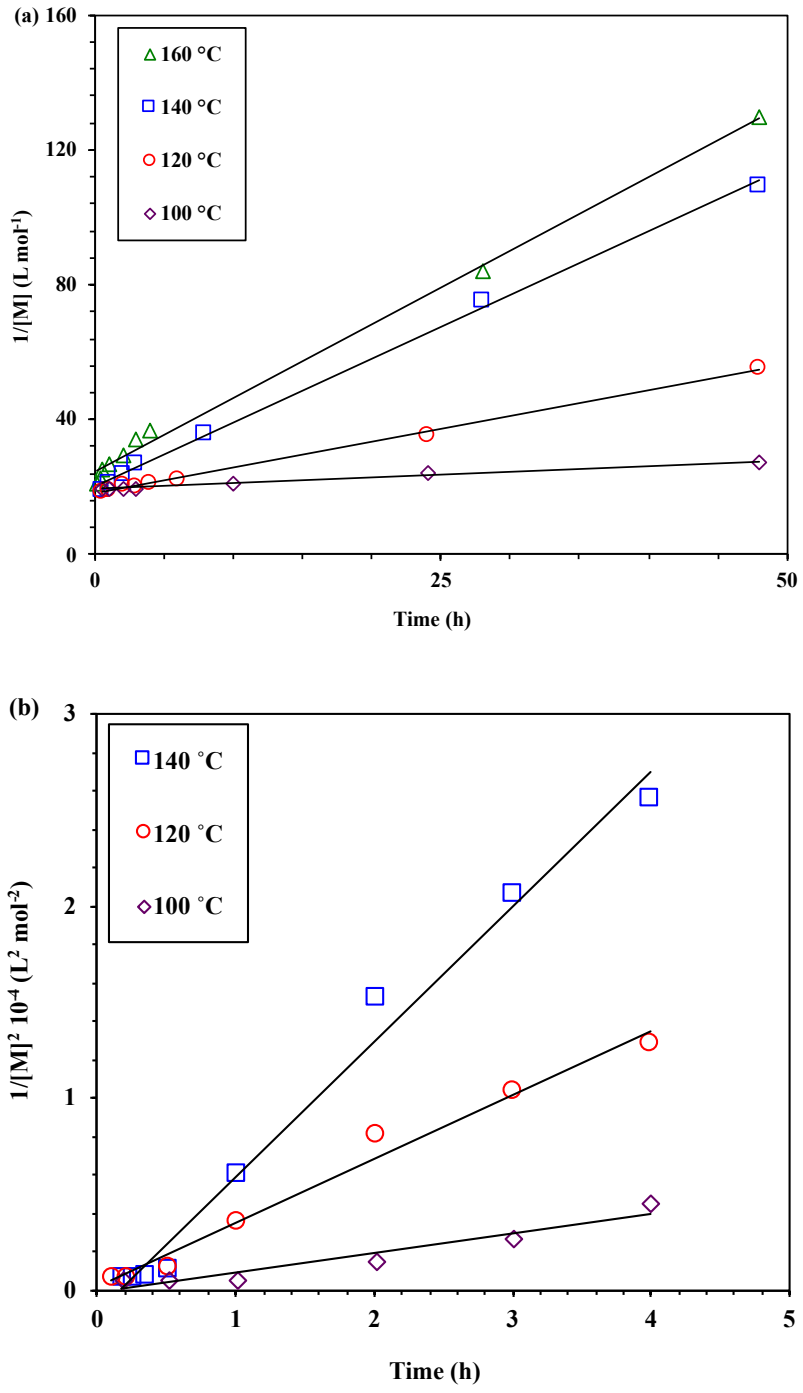

Figure 4.7. Linearized kinetic plots of: (a) second order reaction for polycondensation of DCDPS/BPA, and (b) third order reaction for polycondensation of DFDPS/BPA at various temperatures with K_2CO_3 as the base.

Polycondensation reactions with sodium carbonate as the base were performed for

both DCDPS/BPA and DFDPS/BPA (Figure 4.8 - 4.10). The reaction rate of the polymerization with sodium carbonate is relatively lower than reactions that used potassium carbonate under identical experimental conditions. Two contributing factors are the relatively low solubility of sodium carbonate in DMSO and the lower reactivity of sodium phenolate compared to potassium phenolate. Importantly, the DFDPS/BPA reaction followed the same 2.5-order rate expression at lower conversions and a third-order rate expression at higher conversion. Similarly, a good fit to a second-order rate law for the DCDPS/BPA reaction was observed with sodium carbonate. Thus, it is confirmed that the change of the alkali metal in the base, in this case, is still compatible with the proposed mechanisms.

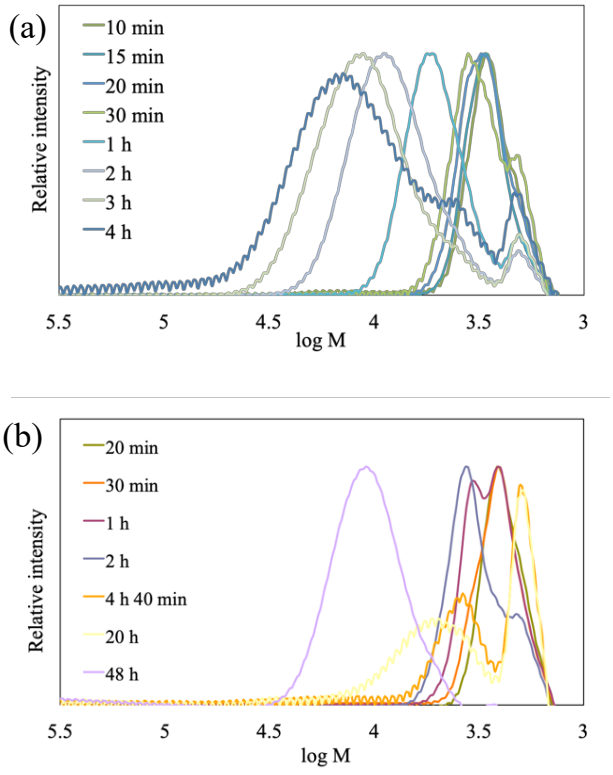

Figure 4.8. Size exclusion chromatography traces of poly(arylene ether sulfone)s from

(a) the DFDPS/BPA polycondensation with sodium carbonate as the base as a function of time at 140 ˚C, and (b) the DCDPS/BPA polycondensation with sodium carbonate as the base as a function of time at 160 ˚C.

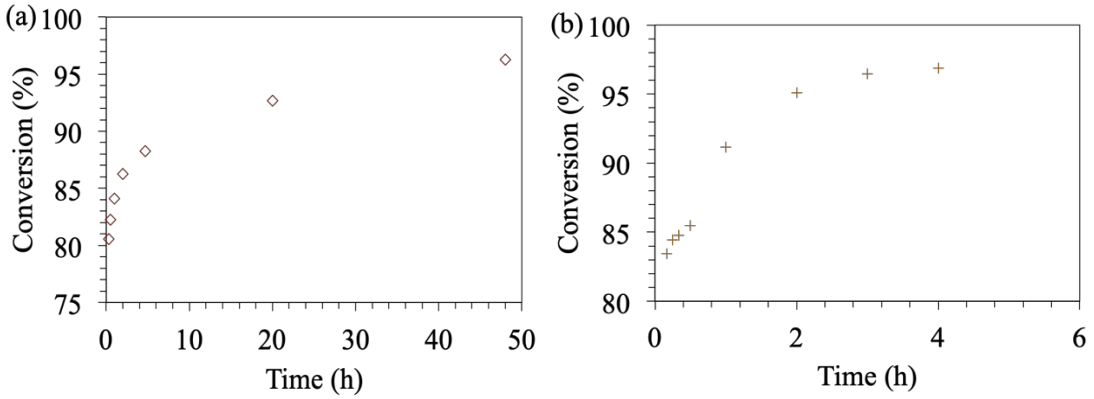

Figure 4.9. Conversion vs. reaction time plots for the polycondensation of: (a) DCDPS/BPA with sodium carbonate as the base at 160 ˚C, and (b) DFDPS/BPA system with sodium carbonate as the base at 140 ˚C.

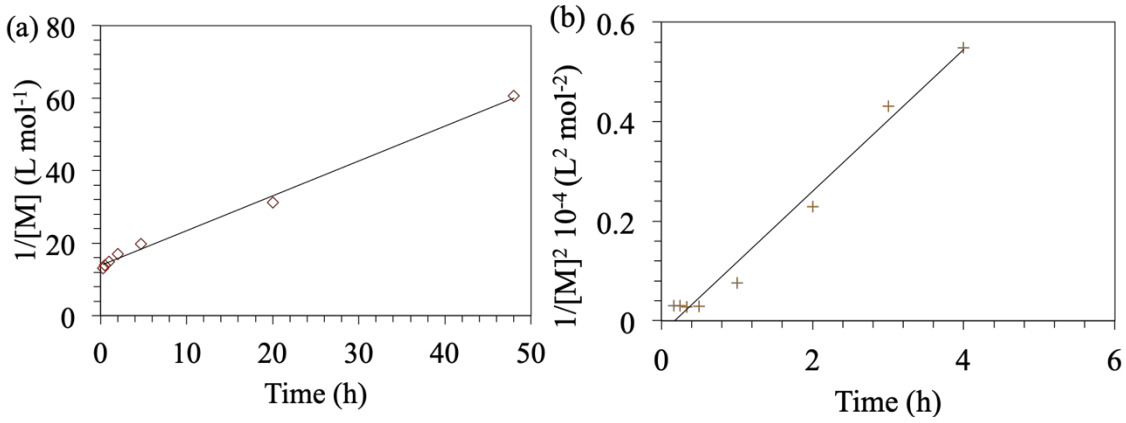

Figure 4.10. Linearized kinetic plots of: (a) second order reaction for the polycondensation of DCDPS/BPA with sodium carbonate as the base at 160 ˚C, and (b) third order reaction for the polycondensation of DFDPS/BPA with sodium carbonate as the base at 140 ˚C.

4.3.3 Mechanisms of DCDPS/BPA and DFDPS/BPA polycondensation reactions

4.3.3.1 Proposed mechanisms from energy barriers calculations

With respect to the experimental observation of an increased reaction order, a mechanism for DFDPS/BPA polymerization is proposed in Scheme 4.3, which is supported by the DFT calculation results (Figure 4.11) in later discussion. In this mechanism, the reaction between ArF and phenolate (PhO-) proceeds through the formation of a three-body complex, in what we call a cation-activated SNAr pathway. The potassium cation, classified as a hard atom, can exist as a free ion or as a charge complex, called species B in both forms for the following expressions (Eq. 1-5). The fluorine atom (bonded to carbon) is also a hard atom and a strong electron donor and interacts with the potassium ion(s). Previous computational work showed that there is a strong binding,[179,180] associating metal counterion bounded to a cresolate with ArF, as a two-body intermediate ArF•••B, to facilitate displacement of the halide during nucleophilic attack from the bound cresolate. In our study, however, the DFT calculations on the relative formation energies of the intermediate complex suggest that the formation of a single three-body ArX•••2B complex (-131 kJ/mol) is strongly favorable over forming two-body ArX•••B complexes (-23 kJ/mol), based on their similar complex formation activation barrier for each path (52 kJ/mol and 59 kJ/mol). In this way, the relatively small size of fluorine and the increased electrophilic ability of ArF, being activated by one of the complexed potassium cations, would further facilitate the nucleophilic attack by the PhO^- from another associated B.[181] More interestingly as the DFT results showed, the activation barrier for the three-body ArCl•••2NaB reaction is 85 kJ/mol, which is significantly higher than that of the two-body ArCl•••NaB complex (68.3 kJ/mol) and the reaction will thus proceed through the energetically favorable two-

body path, as in agreement with second-order kinetics seen experimentally.

In all cases, this proposed mechanism elucidated that the reactions are driven by a change in both enthalpy and entropy, confirmed by the Arrhenius plots (Figure 4.12) based on the experiments. The activation energy (E_a) decreased about 17 kJ/mol for the DFDPS/BPA reaction compared to the DCDPS/BPA reaction. Also, the pre-exponential factor (A) for the DFDPS/BPA reaction (i.e., $A_{DFDPS/BPA}$) was nearly three orders of magnitude higher than $A_{DCDPS/BPA}$, suggesting that it is unlikely that the activated ArCl is attacked by a third free nucleophile due to the steric effect in solvent medium. Table 4.1 summarizes the relevant kinetic data for the series of experiments with both monomers.

After the C-O and C-F bonds have formed and broken, respectively, the Na^+ cation of the NaX product is still complexed to the Ar-O-Ph molecule. It is uphill in energy by ~40 kJ/mol to break this complex for structures considered. If a second NaB is present, i.e. in the three-body case, a second de-coupling reaction must occur to from the final NaF (143 kJ/mol) or NaCl (125 kJ/mol) from NaX●●●NaB. The strong complexing between NaX and NaB suggests that until NaX crystalizes and forms a solid, it acts to bind and thus trap NaB reactants.

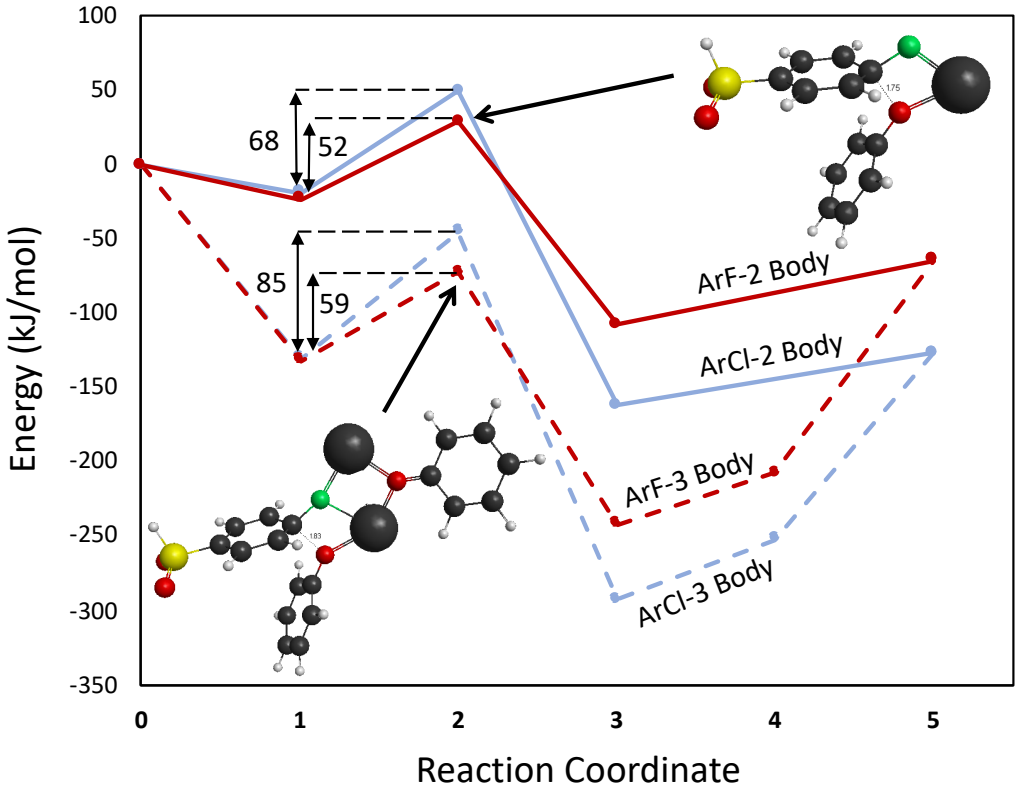

Figure 4.11. Schematic representation of reaction profiles for ArF with NaB in a two-body complex pathway (solid line) and a three-body complex pathway (dashed line). The reaction coordinates are: 1) complexed reactants, 2) transition state, 3) complexed products, 4) ArF-NaB complex, 5) fully de-complexed products – Ar-O-Ph and NaF.

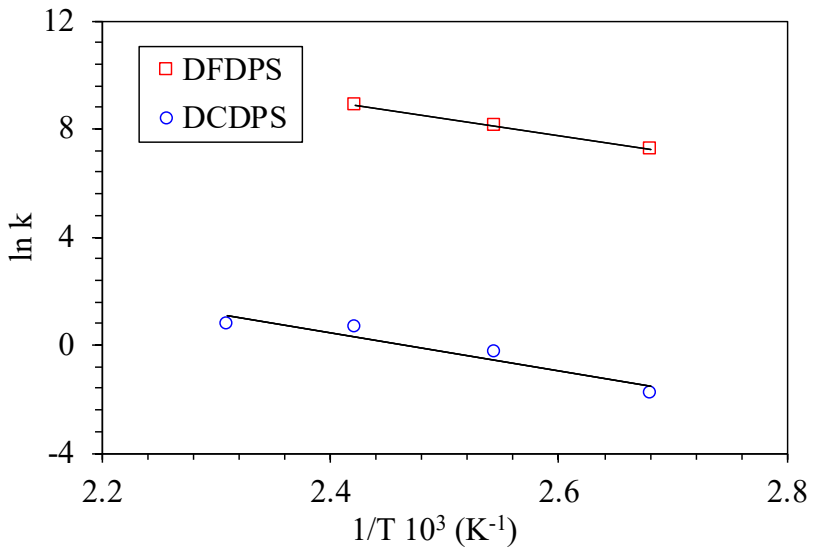

Figure 4.12. Arrhenius plots for the rate constants of polycondensation reactions of DFDPS/BPA (red square) and DCDPS/BPA (blue circle), both with K_2CO_3 as the base.

Table 4.1. Kinetic data for the polycondensation of DFDPS/BPA and DCDPS/BPA with K_2CO_3 as the base.

Monomers	Temperature (˚C)	Reaction time (h)	Conversion (%)	k		ln A	E_a (kJ mol^{-1})
DFDPS + BPA	140	4	98.7	7023	L^2 mol^{-2} h^{-1}	24.14	52.44
	120		97.9	3289			
	100		96.5	1366			
DCDPS + BPA	160	48	98.2	2.19	L mol^{-1} h^{-1}	17.33	69.78
	140		97.9	1.89			
	120		96.0	0.76			
	100		93.2	0.17			

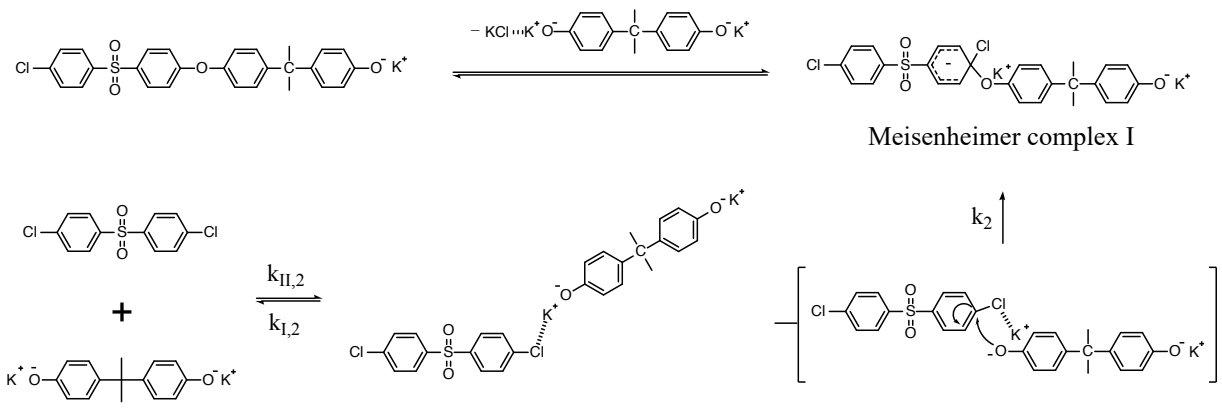

Scheme 4.2. S_NAr mechanism for the polycondensation of PAES with ArCl and K^+PhO^-.

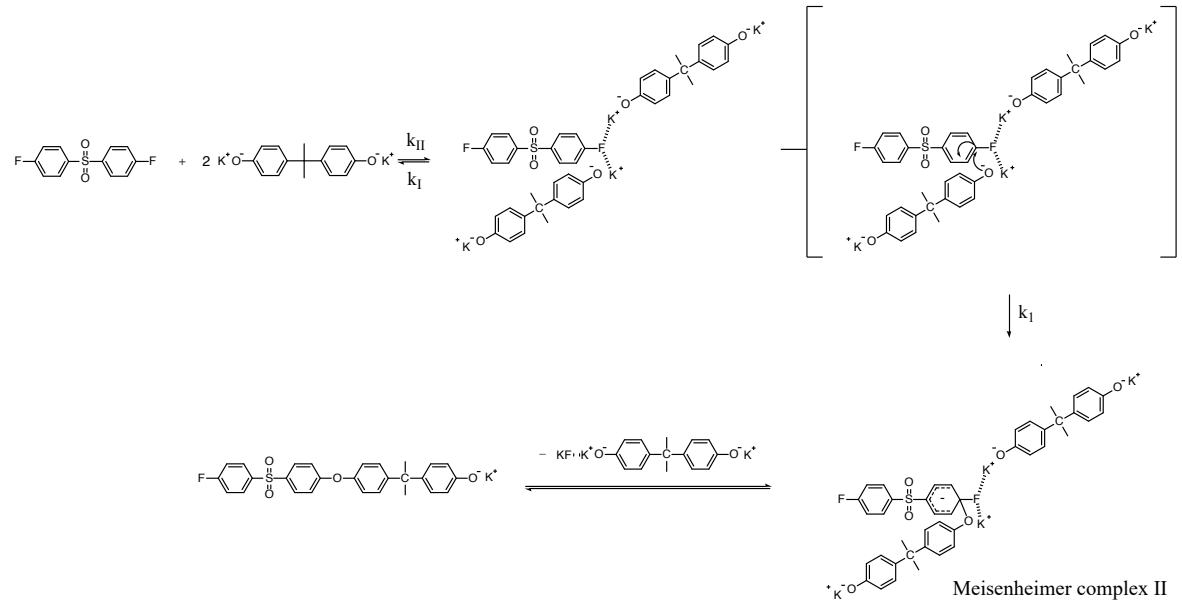

Scheme 4.3. Potassium-activated S_NAr mechanism for the polycondensation of PAES from ArF and K^+PhO^-.

4.3.3.2 Mechanism confirmations from rate law

Based on the energy barrier calculations from both DFT results and the experiments,

therefore, the ArF/BPA reaction proceeds via the formation of a complex ArF•••2B, which is in rapid equilibrium with ArF and two Bs (at least one of the two Bs is in a complexed form, K^+PhO^-), following with nucleophilic attack by the K^+PhO^-. The ArCl/BPA reaction proceeds by single one potassium activated reaction. Specifically, the rapid equilibrium constant $K_{a,1}$ and $K_{a,2}$ for the formation of three-body complex and two-body complex are expressed as

$$\boldsymbol{K_{a,1}} = \frac{\boldsymbol{k_{I,1}[ArF\cdots 2B]}}{\boldsymbol{k_{II,1}[ArF][B]^2}} \quad (1)$$

$$\boldsymbol{K_{a,2}} = \frac{\boldsymbol{k_{I,2}[ArF\cdots B]}}{\boldsymbol{k_{II,2}[ArF][B]}} \quad (2)$$

where $k_{I,1}$ and $k_{II,1}$, $k_{I,2}$ and $k_{II,2}$, are the reverse and forward rate constants, respectively, in the potassium activation step in ArF•••2B case and ArCl•••B case, respectively. The concentration of the complex is thus a function of the concentrations of ArX and B.

The reaction rate is then directly proportional to the concentrations of the activated complex

$$\mathrm{r} = -\frac{d[M]}{dt} = k_1[ArF \cdots 2B] \quad (3)$$

$$\mathrm{r} = -\frac{d[M]}{dt} = k_2[ArF \cdots B] \quad (4)$$

where k_1 and k_2 are the rate constants, with units of $Lmol^{-1}h^{-1}$, of the rate limiting step when the Meisenheimer complex II is formed in the DFDPS/BPA reaction (Scheme 4.3) and DCDPS/BPA reaction (Scheme 4.2), respectively.

Combined with Eq. 1, Eq. 3 then can be expressed as

$$\mathbf{r} = -\frac{d[M]}{dt} = \boldsymbol{k_1 K_{a,1}} \frac{k_{II,1}}{k_{I,1}} [\boldsymbol{ArF}][\boldsymbol{B}]^2 \quad (5)$$

Combined with Eq. 2, Eq. 4 then can be expressed as

$$\mathbf{r} = -\frac{d[M]}{dt} = \boldsymbol{k_1 K_{a,2}} \frac{k_{II,2}}{k_{I,2}} [\boldsymbol{ArF}][\boldsymbol{B}] \quad (6)$$

It is important to note a deviation from the third order rate law fit was observed in the DFDPS/BPA polymerization at conversions < 90%. According to Flory,[182] the failure to fit the data over the low-conversion region is attributed to the large decrease in the polarity of the reaction as the polar anionic phenol groups are replaced by the less polar ether groups with the simultaneous removal of water at the initial stage of the reaction. This decrease in polarity along the reaction may potentially induce a change in the order of reaction, which is corroborated by our experimental data shown in Figure 2b. Specifically, the change in the order of reaction from 2.5 in the low conversion region (Figure 5) to a reaction order of 3 in the high conversion region corresponds to a change from activation of C-F bonds by one free potassium cation from the three-body [ArF•••2B] complex in the high polarity medium to activation of C-F bonds by one of the paired K^+PhO^- complexes from [ArF•••2B] in the relatively low polarity medium. The free potassium cation is a more effective activator than the paired K^+PhO^- in the high polarity, low conversion region, where the concentration of free potassium cation ($[K^+]$) is also relatively high. $[K^+]$ is given by

$$[K^+]=(K_{K^+PhO^-}[K^+PhO^-])^{1/2} \quad (7)$$

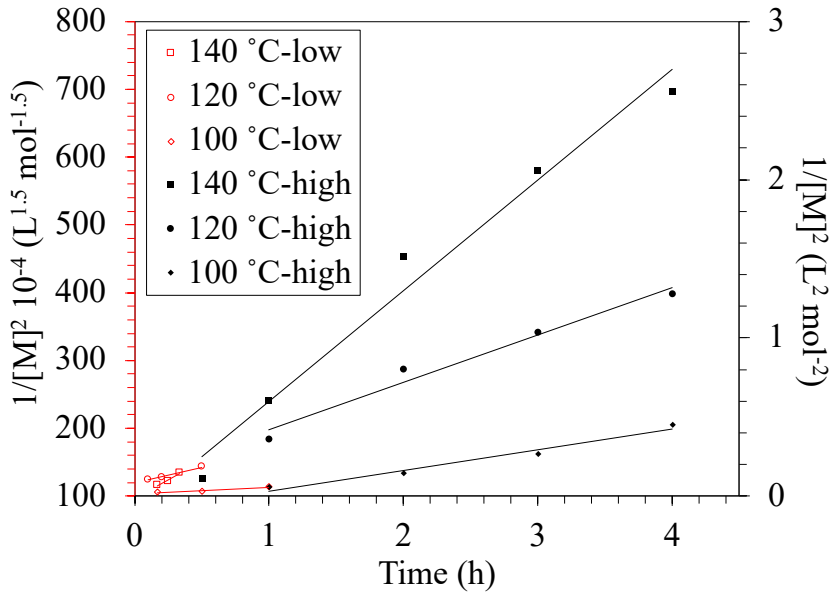

Figure 4.13. Linearized kinetic plot of the DFDPS/BPA polycondensations at conversions <90% (hollow markers) fit to 2.5-order rate expression (red line), and at conversions >90% (solid markers) fit to a third-order rate expression (black line) at various temperatures with K_2CO_3 as the base.

where $K_{K^+PhO^-}$ is the ionization constant for K^+PhO^-. Combining Eq. 5 and Eq. 7 the reaction rate of the DFDPS/BPA polymerization at low conversion follows an overall 2.5 order rate law, given by

$$\mathbf{r = -\frac{d[M]}{dt} = k_1 K_{a,1} \frac{k_{II,1}}{k_{I,1}} (K_{K^+PhO^-})^{\frac{1}{2}} [ArF][K^+PhO^-]^{3/2}} \quad (8)$$

while at high conversion in the relatively less polar reaction medium, the reaction rate of DFDPS/BPA system follows the third-order reaction kinetics expressed as

$$\mathbf{r = -\frac{d[M]}{dt} = k_1 K_{a,1} \frac{k_{II,1}}{k_{I,1}} [ArF][K^+PhO^-]^2} \quad (9)$$

4.4 Conclusions

We have reported the kinetics and mechanisms of S_NAr of ArCl through a second-order rate law and the kinetics and mechanisms of S_NAr of ArF through a third-order rate law. The C-F bond is activated by free alkali cation or alkali-phenolate complexes from the energetically favorable three-body [ArF•••2B] complex, producing a third order rate law and alternate mechanism, while the C-Cl bond is activated by an alkali-phenolate complexes to favorably form two-body [ArCl•••B] complex, producing a second order rate law and alternate mechanism. This conclusion is supported both by experimental observation and computational calculation for both potassium-activated reactions and sodium-activated reactions. Our results not only provide additional fundamental understanding of polycondensation mechanisms for aryl halide monomers, but they also support the importance of C-X interactions with dissociated alkali ions and alkali-containing charge complexes. Further exploration on the polycondensation medium effects on the overall reaction behaviors, as well as the applications of this discovery to other synthetically practical systems is under investigation.

Chapter 5: Zwitterionic Poly(arylene ether sulfone) Copolymers PART 2: Structure and Material Optimization and Structure-Property Relationship Study

To be submitted as

Yi Yang, Alexis Hocken, Matthew D. Green, "Synthesis and characterizations of High Molecular Weight Linear Zwitterionic Poly(arylene ether sulfone) Copolymers for Desalination Membranes".

5.1 Introduction

Zwitterionic polymers have shown promising hydrophilicity nature and stabilities for biofouling resistant in desalination applications,1–12 surfacants,13 etc.. The hydration free energy of the zwitterionic form amino acid, i.e., are higher in magnitude, indicating stronger hydration capability, than the neutral form.14 Compared with the commercial polyamide based reverse osmosis membranes, which intrinsically contains the vulnerable amide bond that is susceptible to chlorine attack, poly(arylene ether sulfone)s (PAES) based membranes showed excellent resistance against degradation due to the chemistry nature of the backbones.15–17 Additionally, zwitterions improve anti-fouling on the membrane surfaces due to their high intrinsic hydrophilicity, which was proposed to form a hydration layer via strong electrostatic interaction between zwitterions and water molecules. This hydration layer provides a steric repulsive barrier to prevent the adsorption of organic molecules and bacteria on the substrate surface.18,19 Beyond that, the rigid PAES backbone in the meantime restricts membrane swelling which is induced by the hydrophilicity of the zwitterion side groups, so as to maintain

the overall perm-selectivity and mechanical strength. Therefore, it is crucial to obtain the high molecular weight zwitterionic PAES for optimal and well-controlled membrane performances, especially mechanical integrity.

A variety of PAES based amphiphilic polyelectrolytes have been synthesized using surface grafting pendant zwitterionic side chains on PAES substrates,20–26 block copolymerization of PAES and other sulfobetaine containing segments.25,27–29. However, very few works have been done on direct amphiphilic modifications on PAES backbone as random copolymers, which comparatively induced less chance for intermolecular interactions among the zwitterionic segments. Zhang and coworkers30,31 prepared zwitterionic PAES via the polycondensation between phenolphthalein with pendant tertiary amine (TA) monomer and difunctional aryl halides to form a cardo PAES-TA backbone, followed by the reaction with sodium bromoethanesulfonate to form the cardo sulfobetaine poly(arylene ether sulfone) (PES-SB). Although this carbo PES-SB random copolymers based membrane showed decreased water contact angle after the incorporation of sulfobetaine group, the hydrophilicity improvement would still be limited due to the strong inter- and/or intramolecular interaction between ammonium group and sulfonate group, and the limited IEC (~ 1 mmol/g). Casey and coworkers32 found that the polyzwitterion brushes swelling behavior is strongly dependent on polymer chain grafting density, which had an optimal intermediate region to avoid the formation of inter- and intramolecular zwitterion complexes for the highest water uptake. It is necessitated and urgent, therefore, to improve IEC limits and control the charge content precisely via novel structure designs.

In the present work, we report the new zwtterionic PAES random copolymers with controllable charge density, as well as well-controlled high molecular weight linear structure for

comparable thermomechanical stability and processibility. Without the incorporation of "bulky" cardo groups on the PAES backbone, we substituted with the allyl-containing bisphenol (DABA) monomer in the polycondenstion reaction with 4,4'-difluorodiphenyl sulfone (DFDPS). Because of the sensitivity of the pendant allyl groups to crosslinking side products under the traditional reaction conditions, we explored the effects of reaction parameters, i.e. stoichiometry, temperature and reaction concentration, on the molecular weight and crosslinking extent, and then applied the optimal conditions for preparation of a series of high molecular weight, high conversion, and linear allyl-PAES (A-PAES) copolymer structures. Then we attached tertiary amine (TA) as the side group via photo-initiated radical thiol-ene click reaction33 between the pendant allyl group and 2-(dimethylamino) ethanethiol, which was fast and efficient. Then it was followed with introduction of sulfonate group via ring-opening of 1,3-propane sultone to fully form two sulfobetaine side groups on each active repeat unit. The structures of the synthesized A-PAES, TA-PAES, PAES-co-SBAES copolymers with various active repeat units ranging from 25 mol% to 100 mol% and the non-functionalized PAES as the control were characterized with respect to constitution, molecular weight, and dispersity index value (Đ) by 1H-NMR spectroscopy and SEC, respectively, showing the success of the herein described synthesis strategy. The effects of charge contents of the series of as-made zwitterionic PAES films on their Tg, thermal stability (Tonset), mechanical properties (Young's modulus, ultimate compressive strength, etc.) were discussed as well. The potential of the presented novel zwitterionic PAES copolymers is emphasized by efficient and controllable synthesis route for mechanically strong membrane performances in the future.

5.2 Experimental

5.2.1 Materials and reagents

4,4'-Difluorodiphenyl sulfone (DFDPS, >98%) was purchase from Thermo Fisher Scientific Chemical and recrystallized from diethyl ether before use. Bisphenol A (BPA, ≥99%) was purchased from BDH® VMR analytical and recrystallized from acetic acid/water (1:1 v/v) before use. 2,2'-Diallylbisphenol A (DABA, 85%) was purchased from Sigma-Aldrich and distilled from tetrahydrofuran (THF) under vacuum before use. THF and toluene (99.8%) were purchased from Sigma-Aldrich and used after passing through M. Braun SPS-800 solvent purification system. Dimethylsulfoxide (DMSO, anhydrous, ≥99.9%), Dimethylformamide (DMF, ≥99.8%), 1,3-propane sultone (1,3-PS), 2-(Dimethylamino) ethanethiol, and 2,2-Dimethoxy-2-phenylacetophenone (DMPA, 99%) were purchased from Sigma-Aldrich and used as received. Potassium carbonate (K_2CO_3, ≥98%) was purchased from Sigma-Aldrich and vacuum dried overnight before use. Deuterated chloroform ($CDCl_3$, 99.8 atom% D, 0.03% (v/v) TMS) was purchased from BDH® VMR analytical and used as received.

5.2.2 Instrumentation

^{1}H-NMR spectroscopy was performed on a Varian 400 MHz spectrometer using deuterated chloroform ($CDCl_3$) to determine the copolymer chemical structures. Samples were prepared as 20 mg of dried polymer dissolved in deuterated chloroform. Chemical shifts are given in ppm downfield from tetramethylsilane (TMS).

In order to determine the molecular weight of the copolymers, size exclusion chromatography (SEC) was performed using a Waters Alliance e2695 HPLC system interfaced to a light scattering detector (miniDAWN TREOS) and an Optilab T-rEX differential refractive index (dRI) detector. The mobile phase was THF Optima (inhibitor-free) at a flow rate of 1.0 mL

min-1, and samples were calibrated against Pressure Chemical Company low dispersity polystyrene standards of 30 kDa and 200 kDa using Astra v6.1 software. Then, ~1.0 mg·mL-1 filtered solutions of polymer in THF were prepared for SEC.

Thermogravimetric analysis (TGA) was performed using a TA instruments TGA 2950. Measurements were carried out under nitrogen at a heating rate of 10 ˚C/min.

The glass transition temperature (T_g) was characterized using differential scanning calorimetry (DSC, Q2000 from TA Instruments). Samples of ~5 mg in hermetically sealed aluminum pans were first heated to 220 ˚C and then cooled to -50 ˚C before heating to 250 ˚C. The heating and cooling rate was set to 5 ˚C/min and 10 ˚C/min, respectively. The reported values of T_gs were taken from the second heating scan.

An Instron E3000 was used to perform compression testing of the series of PAES-co-SBAES-XX copolymer films, as well as uncharged PAES-0 film. A dry sample was used for each test. The samples were cut into rectangles and then compressed at a strain rate of 0.1500 mm/min at 23 ˚C until the load force reached to the limit (5 kN).

5.2.3 Synthesis of allyl-modified poly(arylene ether sulfone) (A-PAES) copolymers

The allyl-containing poly(arylene ether sulfone) copolymer was synthesized via conventional polycondensation of poly(arylene ether sulfone)s28 with modified reaction conditions. All the series of A-PAES copolymers were synthesized in the same fashion with an off-set stoichiometry of r = 0.94 between phenol group and aryl halide group, except with different BPA/DABA ratios for corresponding targeted functionality contents (i.e., for A-PAES-25, the feed molar ratio among DFDPS, BPA and DABA monomers was 100:70.5:23.5). Take

A-PAES-75 as an example herein. BPA (0.792 g, 3.476 mmol), DABA (3.212 g, 10.428 mmol), DFDPS (3.757 g, 14.791 mmol), and K_2CO_3 (2.015 g, 14.599 mmol) were added to a three-neck, 250-mL flask equipped with a condenser, Dean Stark trap, nitrogen inlet/outlet, and a mechanical stirrer. DMSO (50 mL) and toluene (15 mL) were added to the flask to dissolve the monomers. The solution was heated under reflux at 135 °C for ~3 h while the toluene-water azeotrope and toluene residue was completely removed from the reaction mixture. The reaction was continued under static nitrogen atmosphere for another 1~4 h at 135 °C. The reaction mixture was cooled to room temperature and diluted with 200 mL of THF. It was filtered to remove the salt, and was precipitated by addition to stirring DI water. The polymer was filtered and dried under vacuum at 100 °C for 24 h. Then, the polymer was dissolved in THF, passed through a 0.45 μm Teflon® filter, then isolated by precipitation in DI water. The product (A-PAES-75) was freeze-dried at -89 °C under vacuum for 24 h.

5.2.4 Synthesis of tertiary amine-modified PAES (TA-PAES) copolymers

The synthesized A-PAES-75 copolymer (5 g, 14.805 mmol of allyl group), 2-(dimethylamino) ethanethiol (20.975 g, 10 equiv.), and DMPA (1.134 g, 0.3 equiv.) were dissolved in DMF (100 mL) to perform a post-polymerization modification via the thiol-ene click reaction. The reactor flask was purged with nitrogen for 15 min. Irradiation with UVGL-15 compact UV lamp (365 nm) was carried out for 2 h at 23 ˚C. The solution was concentrated using a rotary evaporator, and the polymer was then isolated by precipitation in DI water, and the product was freeze-dried at -89 °C under vacuum for 24 h.

5.2.5 Synthesis of PAES-co-SBAES copolymers

To a solution of TA-PAES-75 (5 g, 11.346 mmol of TA group) in DMF (100 mL), 1,3-propane sultone (2.772 g, 2 equiv.) was added. The solution was stirred at room temperature for 1 h and at 60 °C for 12 h. The solution was concentrated using a rotary evaporator, and the remaining solution was diluted with DMF (5 mL) and dialyzed against DMF in a dialysis tube (1 kDa MWCO) for 3 days. The DMF outside the dialysis tube was exchanged with fresh DMF every 2 h over the first 10 h and then every 6 h until completion. The polymer was then isolated by precipitation in DI water, and the product was freeze-dried at -89 °C under vacuum for 24 h.

5.2.6 Film Preparation

The free-standing, uniform, dense polymer films were prepared by dope casting. The PAES-co-SBAES-XX copolymers, or PAES-0, (25 wt%) were dissolved in DMF. Next, the polymer solution was filtered through a 0.45 μm Teflon® filter, then the filtered solution was cast onto a mylar sheet. The cast films were first dried in an oven at 80 ˚C for 24 h, and then under vacuum at 110 ˚C for 48 h to further remove the solvent residual. The film was peeled from the mylar sheet and soaked in deionized water overnight to extract residual solvent. All film samples were freeze-dried at -89 ˚C under vacuum at least overnight before tests.

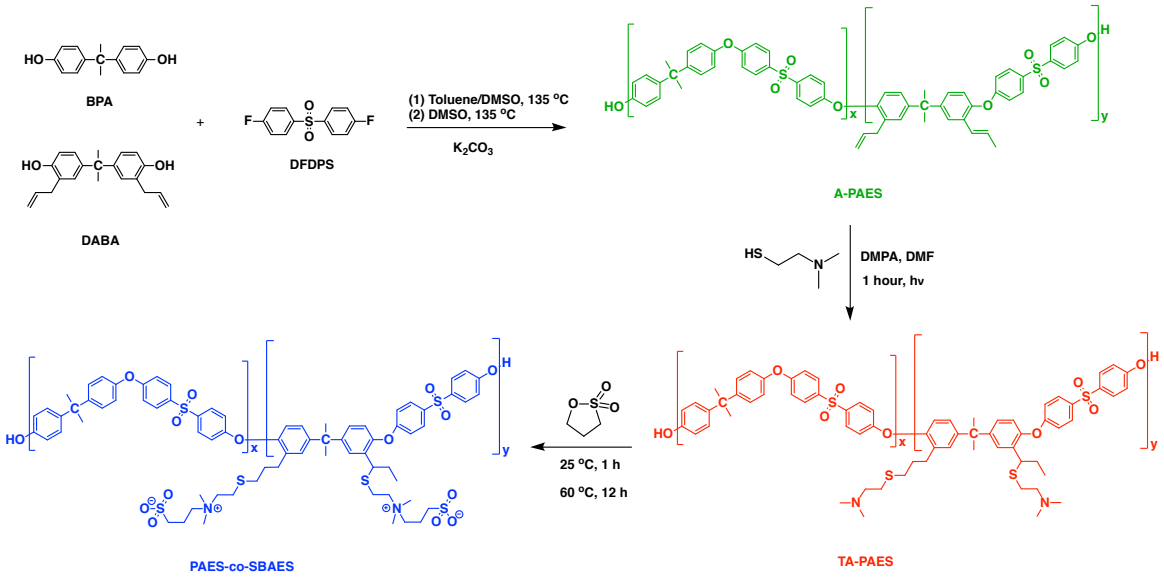

Scheme 5.1. Synthesis route of zwitterionic PAES-co-SBAES-XX (XX = 0~100).

5.3 Results and discussions

5.3.1 Synthesis of high Mw linear allyl-containing poly(arylene ether sulfone) (A-PAES) copolymers

The A-PAES copolymers (Scheme 5.1) were synthesized via the S_NAr polycondensation reactions34–38 using a highly reactive aryl halide monomer, DFDPS, and both bisphenol A (BPA) and DABA as the non-allyl-containing and allyl-containing nucleophile monomers, respectively. Off-set stoichiometry of DFDPS and BPA/DABA was set to 1:0.94 for optimized molecular weight and complete conversion, based on our previous study that showed the effect of the non-stoichiometry on compensating the hydrolysis side reactions of the aryl halides, as result of improvement of reaction conversions and molecular weight. The allyl functional group contents along the polymer backbone were precisely controlled by the feed ratio of BPA and DABA. Take the 75 mol% allyl-containing repeat unit (A-PAES-75) as an example, DFDPS (1

equiv.) was reacted with BPA (0.235 equiv.) and DABA (0.705 equiv.) in an aprotic polar solvent, Dimethyl sulfoxide (DMSO), and toluene at 135 ˚C under nitrogen flow until all the toluene was completely removed, then the reaction was continued for 4~8 h to achieve the target molecular weight. To obtain high molecular weight and to avoid side reactions, i.e., crosslinking reaction of allyl groups, which normally occurred under high temperatures or even other moderate conditions.39,40 To obtain the high conversion of the reactions and avoid crosslinking side reaction, we studied the effect of the concentration of reaction solution on crosslinking side reactions. We monitored via SEC measurements (Figure 5.1) for three different reaction batches conducting in high (Figure 5.1a), medium (Figure 5.1b), and low (Figure 5.1c) reaction solution concentrations of 0.47, 0.52, 0.64 mmol/L (total amount of monomers in the DMSO/toluene solvents after toluene-water azeotrope was completely removed from the reaction mixture at the first 3h of reactions), respectively. The reactions were conducted under the identical temperature (135 ˚C) and stoichiometry (DFDPS:BPA:DABA = 1:0.235:0.705). We observed that only the highly concentrated reaction batch started showing up a light scattering shoulder after 6 h of the reaction, and the most diluted reaction batch showed an extremely slow kinetics without light scattering shoulder (crosslinking structure) detectable even after 42 h of the reaction. The reaction batch conducting in a medium concentration, on the other hand, proceeded in a reasonable reaction time without any crosslinking reaction when it reached 98.6% of conversion after 4 h of the reaction. Thus, an optimal reaction concentration of 0.52 mmol/L was utilized for all systems in the following polycondensation synthesis.

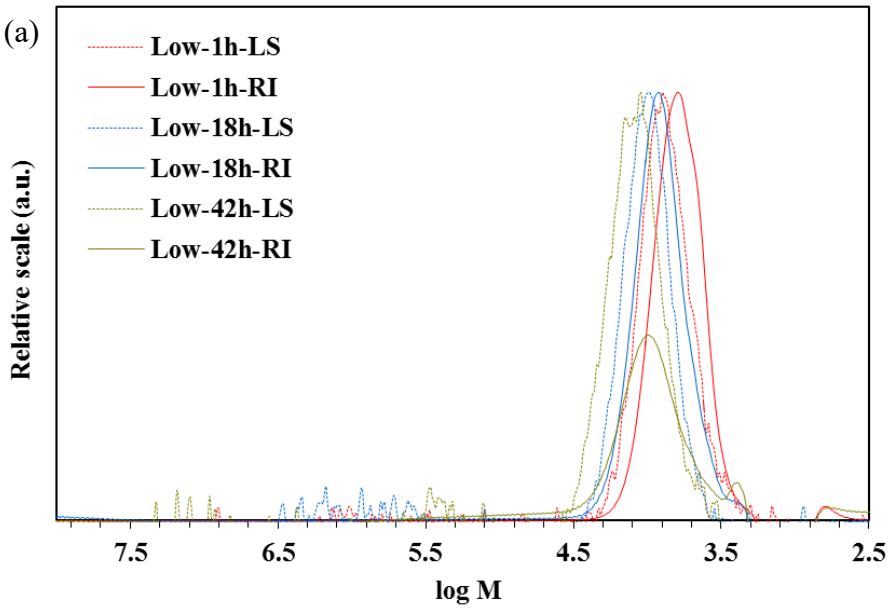
(a)
Low-1h-LS
Low-1h-RI
Low-18h-LS
Low-18h-RI
Low-42h-LS
Low-42h-RI
Relative scale (a.u.)
7.5
6.5
5.5
4.5
3.5
2.5
log M

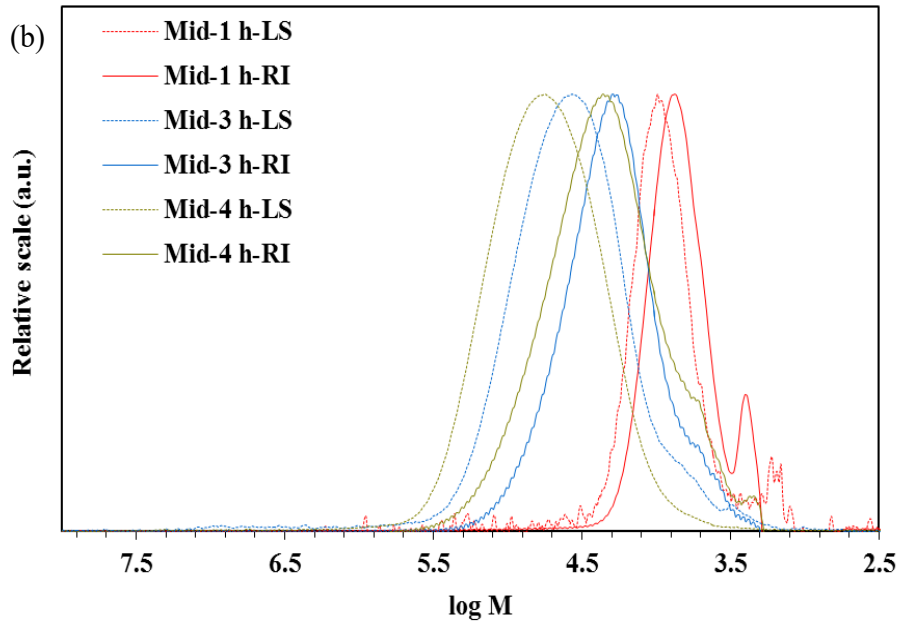
(b)
Mid-1 h-LS
Mid-1 h-RI
Mid-3 h-LS
Mid-3 h-RI
Mid-4 h-LS
Mid-4 h-RI
Relative scale (a.u.)
7.5
6.5
5.5
4.5
3.5
2.5
log M

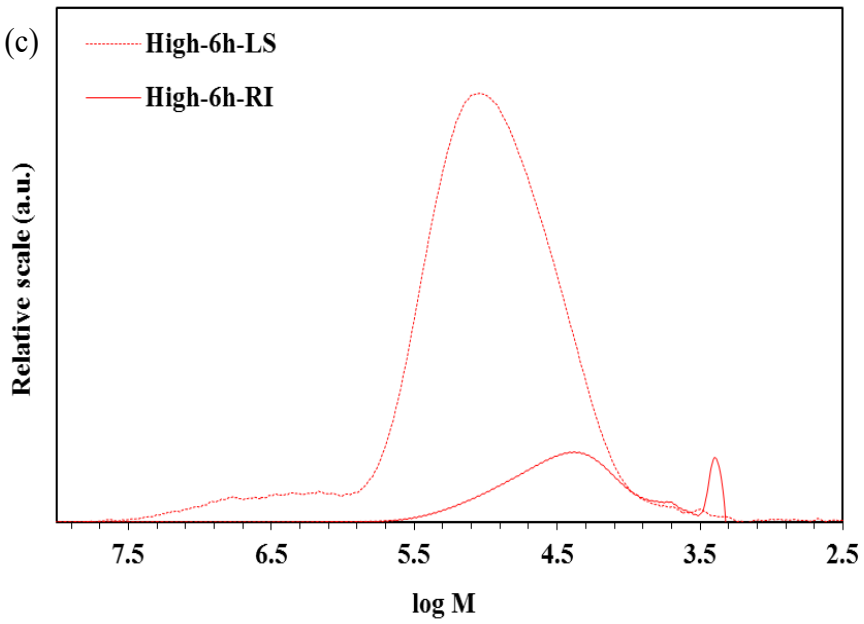

Figure 5.1. Size exclusion chromatography traces of allyl-modified poly(arylene ether sulfone) copolymer (A-PAES-75) synthesized under 135 ˚C reaction temperature. Polymer molecular weights were measured by light scattering (LS) detector (dashed line) and refractive index (RI) detector (solid line), for the reaction batch in (a) low concentration, (b) medium concentration, (c) high concentration condition, and (d) a summary of the measured data, respectively. Reaction under high concentration induced cross-linking side reaction detected via LS shoulder peak at high Mw range, while the reaction in low concentration underwent non-crosslinking side reaction but in an extremely slow kinetics. The reaction in medium concentration can proceed in a reasonable reaction rate and crosslinking-free fashion.

A series of the A-PAES copolymers with various allyl side group contents (0, 25 mol%, 50 mol%, 75 mol%, and 100 mol%, namely A-PAES-XX, where XX indicates the molar fraction of allyl-containing segments) were synthesized in the identical fashion as described above, and were analyzed by SEC measurements in THF calibrated with polystyrene standards and via 1H-NMR spectroscopy in chloroform-d. The corresponding spectra is shown in Figure 5.2 and Figure 5.3, respectively. The obtained A-PAES copolymers had well-controlled and consistent

number average molecular weight (Mn) of 33.7±0.7 kg mol-1, weight average molecular weight (Mw) of 63.7±1.1 kg mol-1 and Đ up to 1.89±0.03, indicating the excellent control over the polycondensations to reach high molecular weight and the full conversion.

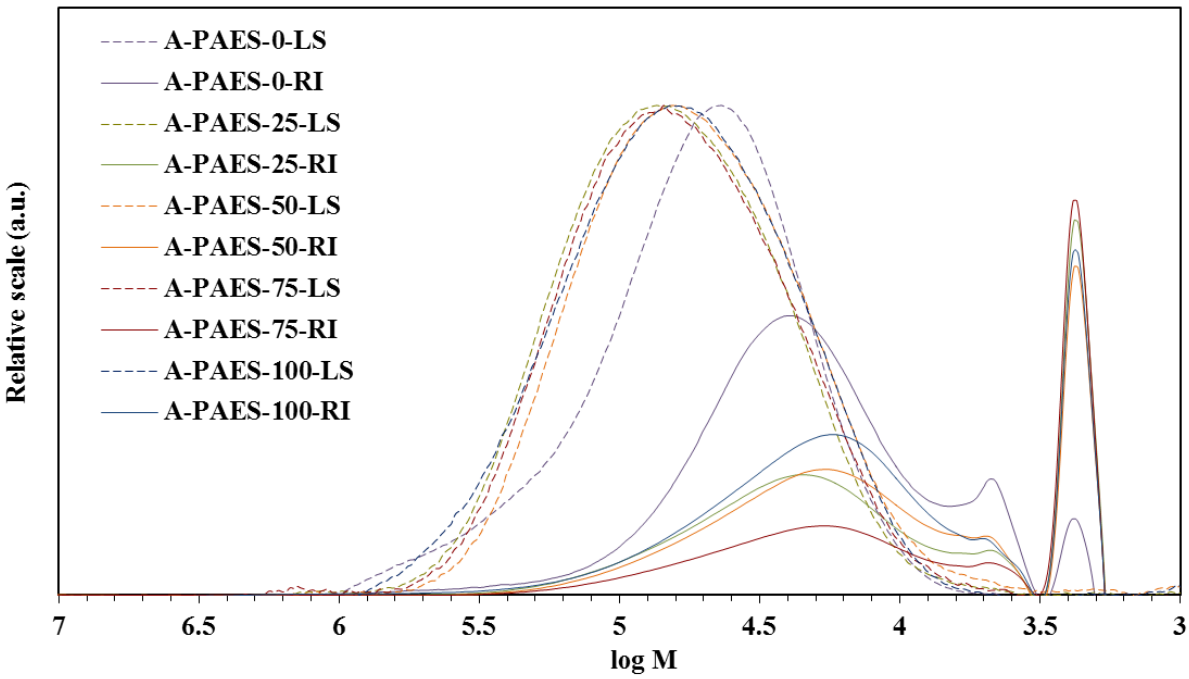

Figure 5.2. Size exclusion chromatography traces of allyl-modified poly(arylene ether sulfone) copolymer (A-PAES-XX, XX = 0~100) measured by light scattering (LS) detector (dashed line) and refractive index (RI) detector (solid line).

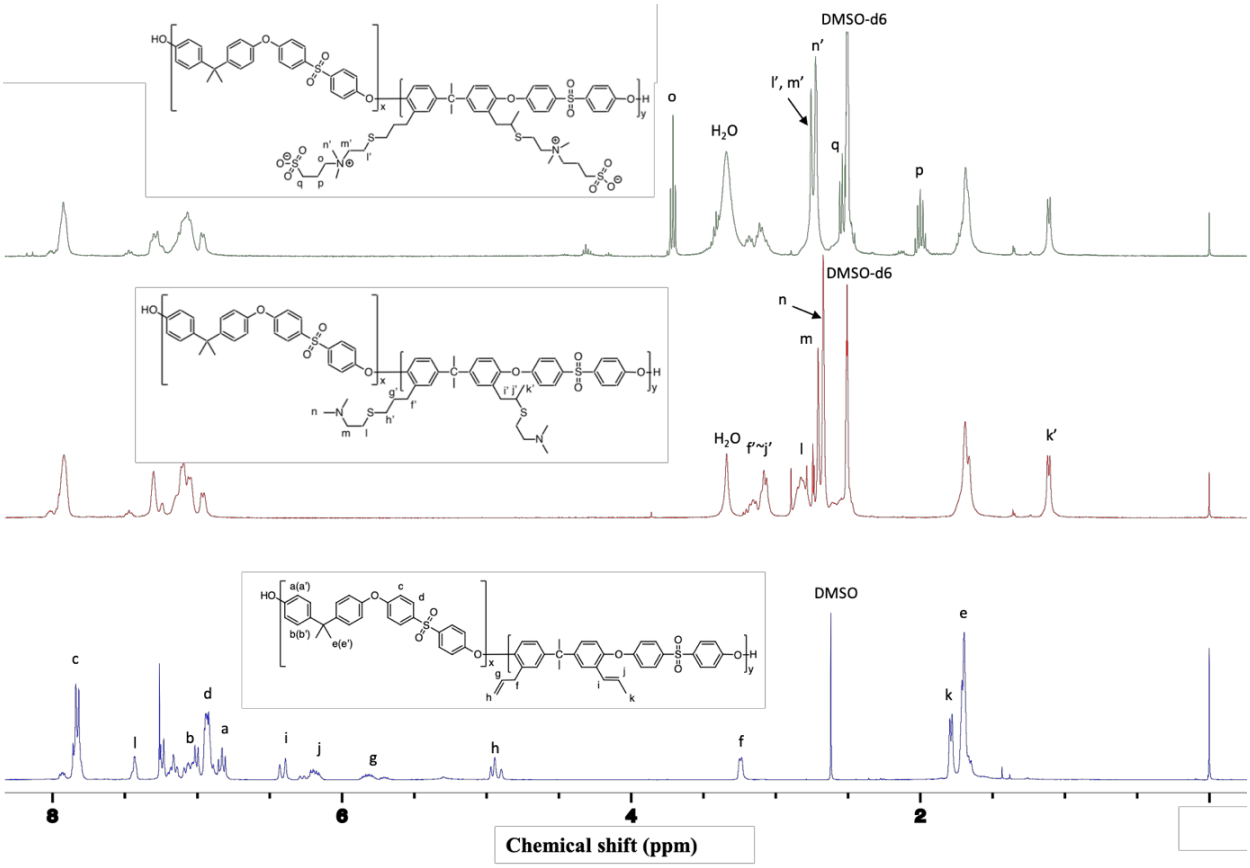

Figure 5.3. ^{1}H-NMR spectra of A-PAES copolymers (bottom), tertiary amine-modified PAES (TA-PAES) copolymers (middle), and zwitterionic PAES-co-SBAES copolymers (top), respectively. Plots indicate successful copolymerization of PAES-co-SBAES with an SBAES content of 75 mol%.

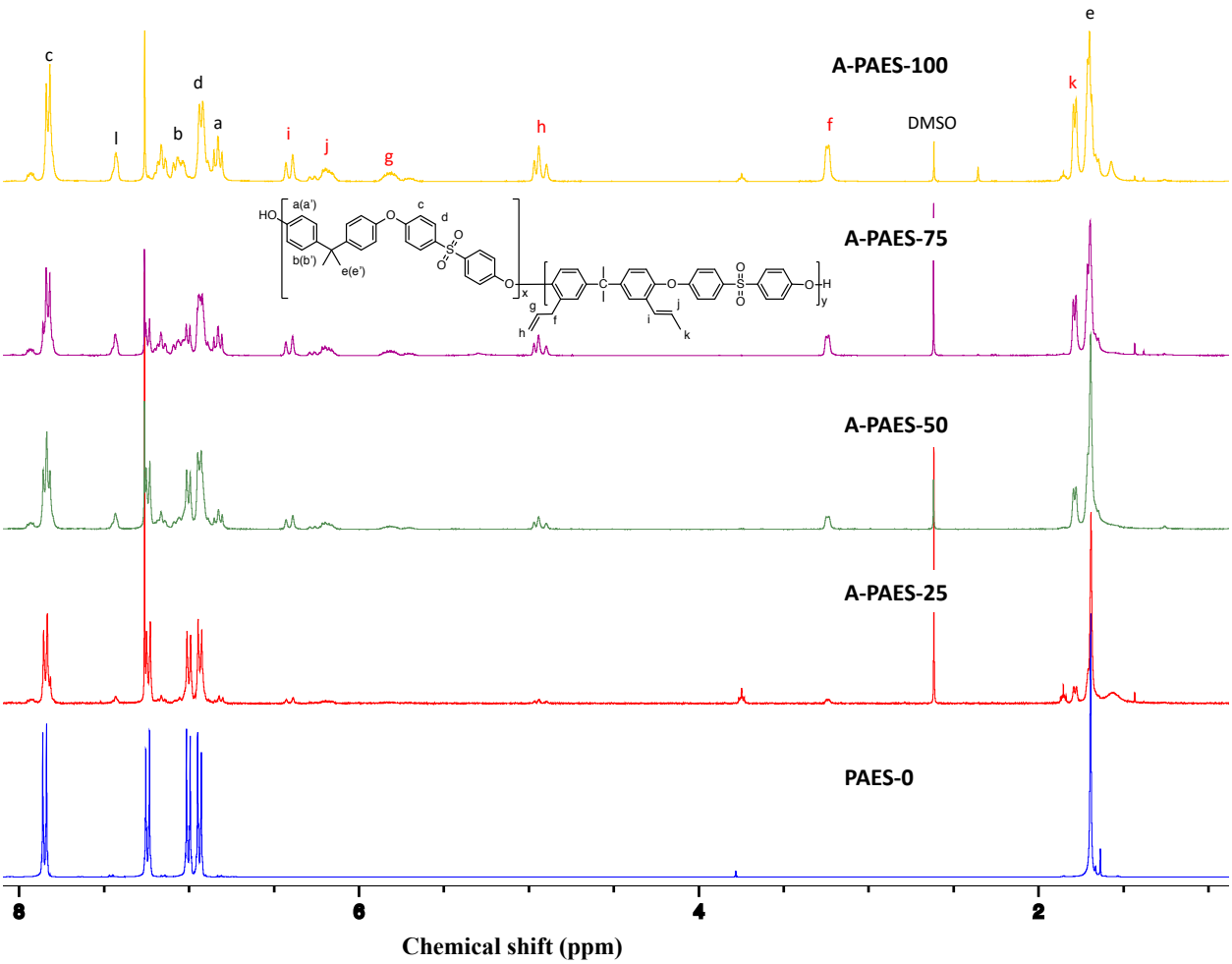

Figure 5.4. ^{1}H-NMR spectra of A-PAES-XX copolymers (XX = 25, 50, 75, 100) and unfunctionalized PAES-0. Plots indicate successful copolymerization of A-PAES with allyl functionalized segment contents of 25 mol%, 50 mol%, 75 mol%, and 100 mol%, respectively.

The composition of the A-PAES and the degree of functionalization (DF) of the pendant allyl group on the PAES backbone were determined by ^{1}H-NMR spectroscopy (Figure 5.3 and Figure 5.4). Upon the incorporations of DABA monomer in the polycondensations, the peaks arising from the protons on $–CH_2CH=CH_2$ (signal f, g, and h, respectively) showed up at 3.2, 5.8, and 4.9 ppm, respectively, and its isomerized form $–CH=CHCH_3$ (signal i, j, and k, respectively) showed up at 6.4, 6.2, and 1.8 ppm, respectively, indicating the successful incorporation of allyl-

containing segments on the backbone. It is worth to mention that the isomerization of allyl group would maintain the reactivity for the post-functionalizations below, even it typically happed once the reaction temperature is above 80˚C. The total integral of the peaks from signal f~k , relatively compared with the integral of the reference peak from the diphenyl sulfone (i.e. signal c), was used to assess the contents of pendant allyl group covalently bonded with the PAES backbone. The integral ratio between peak f~h and i~k was quite useful to assess the isomerization extent. The calculated allyl-containing repeat unit contents are compiled in Table 5.1, and are nicely consistent with the feed ratios of 0, 25, 50, 75, and 100 mol%, respectively, indicating the success of the synthesis strategy for controllable active allyl group contents.

Table 5.1 Summary of number-averaged molecular weight, weight-averaged molecular weight, and dispersity of A-PAES-XX from various monomer stoichiometric ratios, measured from NMR and SEC.

DABA:BPA (stoichiometry)	A-PAES content (NMR) (%)	Mn (kDa)	Mw (kDa)	PDI
0:100	0	34.9	64.7	1.84
25:75	22	32.9	62.4	1.90
50:50	45	33.2	62.5	1.88
75:25	72	34.3	63.7	1.86
100:0	100	33.3	65.0	1.95

5.3.2 Post-polymerization functionalization to prepare poly(arylene ether sulfone)-co-(sulfobetaine arylene ether sulfone) (PAES-co-SBAES) copolymers

A series of zwitterionic PAES-co-SBAES copolymers were synthesized by two-step post-

functionalization of A-PAES copolymers. Firstly, the allyl moieties of the A-PAES copolymers were functionalized with thiol, i.e., 2-(dimethylamino) ethanethiol, by thiol-ene-click reaction to obtain tertiary amine groups as part of the side group, as given in Scheme 5.1. Upon the functionalization, the peaks arising from the allyl group and its isomer (signal f~k in Figure 5.3) vanished after the thiol-ene click reaction, and the new peaks showed up at 2.67~3.2 ppm and 1.1 ppm, respectively, indicating the successful functionalization with 2-(dimethylamino) ethanethiol and full conversion into the corresponding PAES copolymers having tertiary amine groups. The overall integral of the new peaks (signal f'~k' and l~n) was calculated and compared with the overall integral of the peak f~k to confirm the assumption on the structure. Thus, the isomerized allyl groups–as part of the PAES side groups–did not affect the functionalization. The synthesized TA-PAES series with various TA-containing segment contents (named as TA-PAES-XX in Figure 5.2b, where XX indicates the molar fraction of TA-containing segments) were analyzed by ^{1}H-NMR spectroscopy in DMSO-d_6 (shown in Figure 5.5).

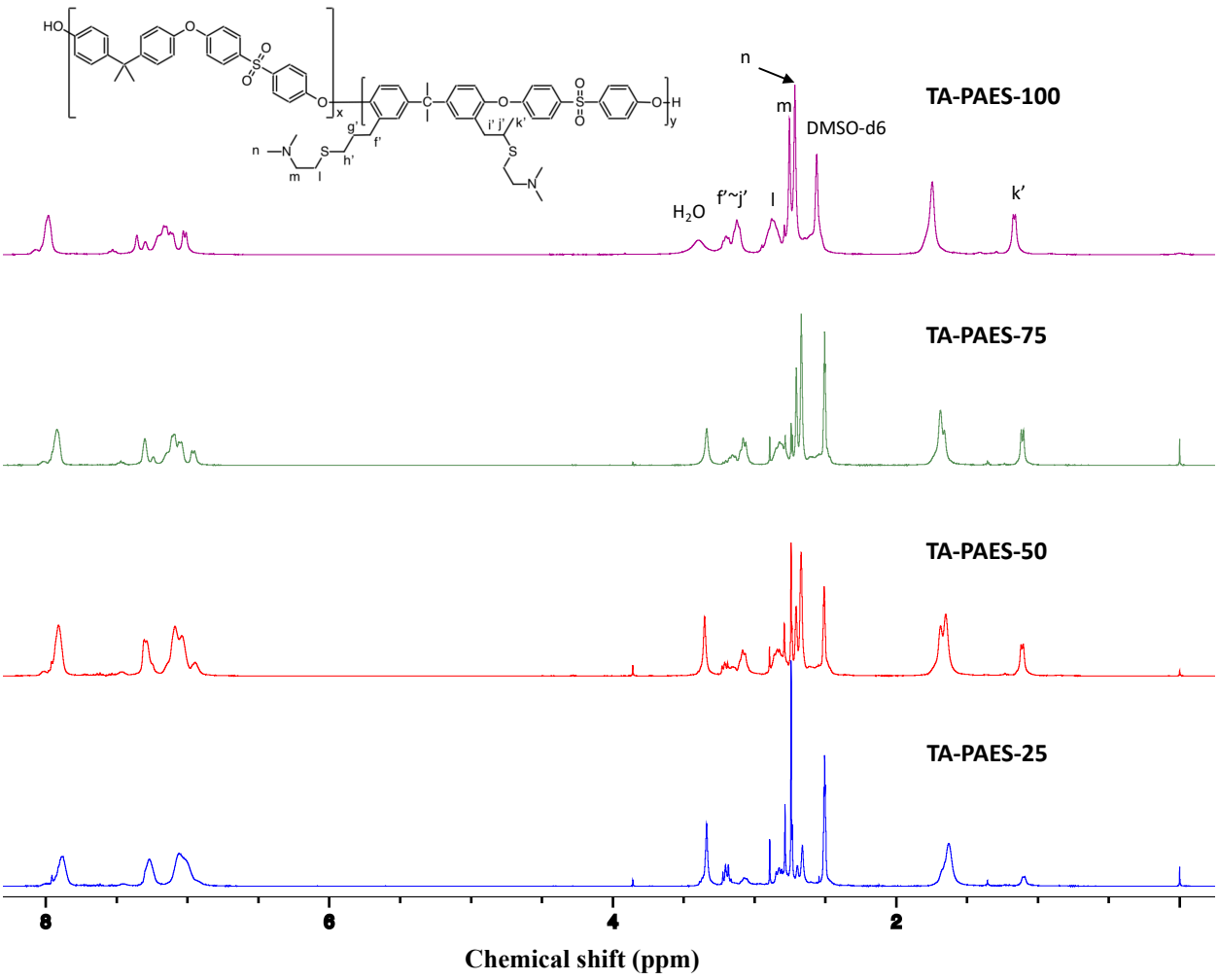

Figure 5.5. [1]H-NMR spectra of TA-PAES-XX copolymers (XX = 25, 50, 75, 100). Plots indicate successful copolymerization of TA-PAES with tertiary amine functionalized segment contents of 25 mol%, 50 mol%, 75 mol%, and 100 mol%, respectively.

We utilized the simple ring-opening reaction of 1,3-propane sultone by the tertiary amine attached to the polymer backbone to incorporate the sulfonate group and form the sulfobetaine functionality (Scheme 5.1). 1H NMR spectroscopy in DMSO-d6 was employed to analyze the zwitterionic PAES copolymers. The corresponding NMR spectra are shown in Figure 5.3 and Figure 5.6.

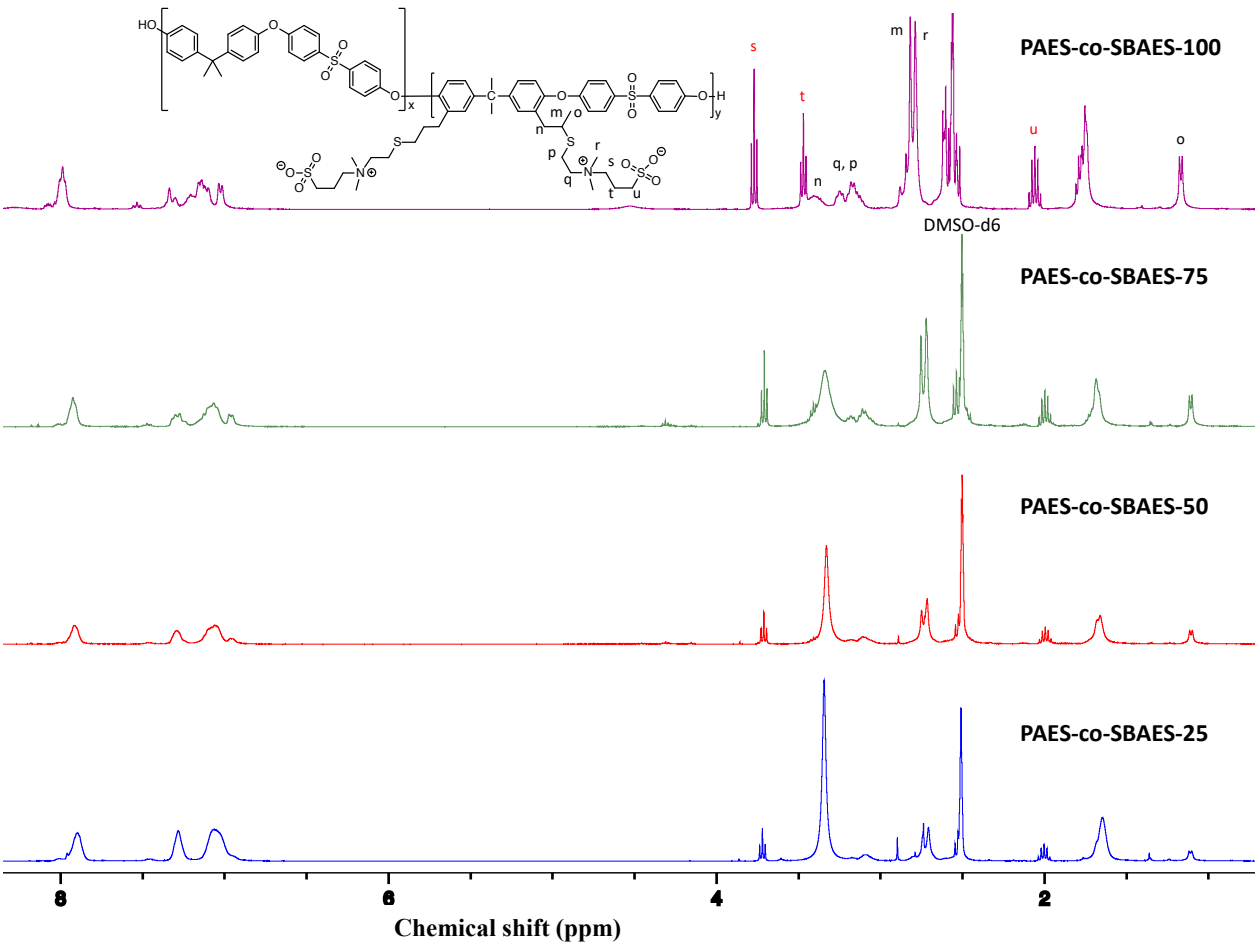

Figure 5.6. ^{1}H-NMR spectra of PAES-co-SBAES-XX copolymers (XX = 25, 50, 75, 100). Plots indicate successful copolymerization of PAES-co-SBAES with sulfobetaine functionalized segment contents of 25 mol%, 50 mol%, 75 mol%, and 100 mol%, respectively.

The peaks arising from the $–CH_2CH_2N(CH_3)_2$ (signal l, m, n in Figure 5.3) shifted from 2.70, 3.08, 2.67 ppm to 2.75, 3.11, 2.72 ppm, respectively, collaboratively with the new instinct signals at 3.71, 2.53, and 1.99 ppm, indicating the successful incorporation of sulfobetaine. Moreover, the integral of the peak from signal o, p, q was in agreement with the overall integral of the peak from signal l', m', n', confirming the effectiveness and full conversion of the ring-opening reaction. So far, the use of the reaction conditions (135 ˚C, r=0.95, in medium

concentration) during the polymerization, which induced the formation of allyl isomers, did not affect the post-polymerization functionalization and therefore demonstrates the efficient synthesis strategy. The stepwise post-polymerization functionalization of high molecular weight linear A-PAES copolymers, with quantitative control over the incorporation of sulfobetaine as the side group of the PAES backbone, were achieved as mentioned above. Within the next sections, the series of zwitterionic PAES-co-SBAES (namely PAES-co-SBAES-XX, where XX indicates the molar fraction of SBAES segments) copolymers and the series of uncharged A-PAES copolymers will both be used for the preparation of dense films for the further characterizations.

5.3.3 Thermal analysis

A high thermal stability of polymeric membranes is a crucial property required for many membrane applications, such as the thermally-driven pervaporation, which operates at high temperatures.41 Figure 5.7 shows the TGA and the corresponding DTA traces recorded for the series of zwitterionic PAES-co-SBAES copolymers under nitrogen at a heating rate of 10 ˚C/min. As seen, the control sample, uncharged PAES (PAES-0), exhibited one-step weight loss temperature at about 500 ˚C, associated with the degradation of the PAES backbone. In comparison with PAES-0, the zwitterionic copolymers (PAES-co-SBAES-XX) with similar range of molecular weight showed multi-step weight losses: a starting decomposition temperature at about 250 ˚C, which was attributed to the decomposition of the quaternary ammonium groups, following with the second weight loss step at about 330 ˚C and the third weight loss step at about 420 ˚C, associated with the degradation of sulfonate group and the cleavage of C-S bonds, respectively, and then polymer backbone degradation occurred at higher

temperatures (~500 ˚C).30,42 The magnitude of the step in TGA trace, or the intensity of the peak in DTA trace, was directly correlated with the corresponding degraded component content. Thus, as shown in Figure 5.7 with the increase of the zwitterionic charge contents of the PAES copolymers from 0 to 100 mol%, both the increases of weight loss step of each pendant side group and the decrease of the weight loss step of the polymer backbone confirmed the compositions of the synthesized series as expected. Due to the relatively thermal instability of the quaternary ammonium groups, compared with the charge-free PAES, the PAES-co-SBAES copolymer series exhibited a lower starting decomposition temperature at about 220 ˚C, and 5% weight loss at about 250 ˚C ($T_{D,\,5\%}$), which could already satisfy the requirement of the thermal stability for water treatment membranes applications.

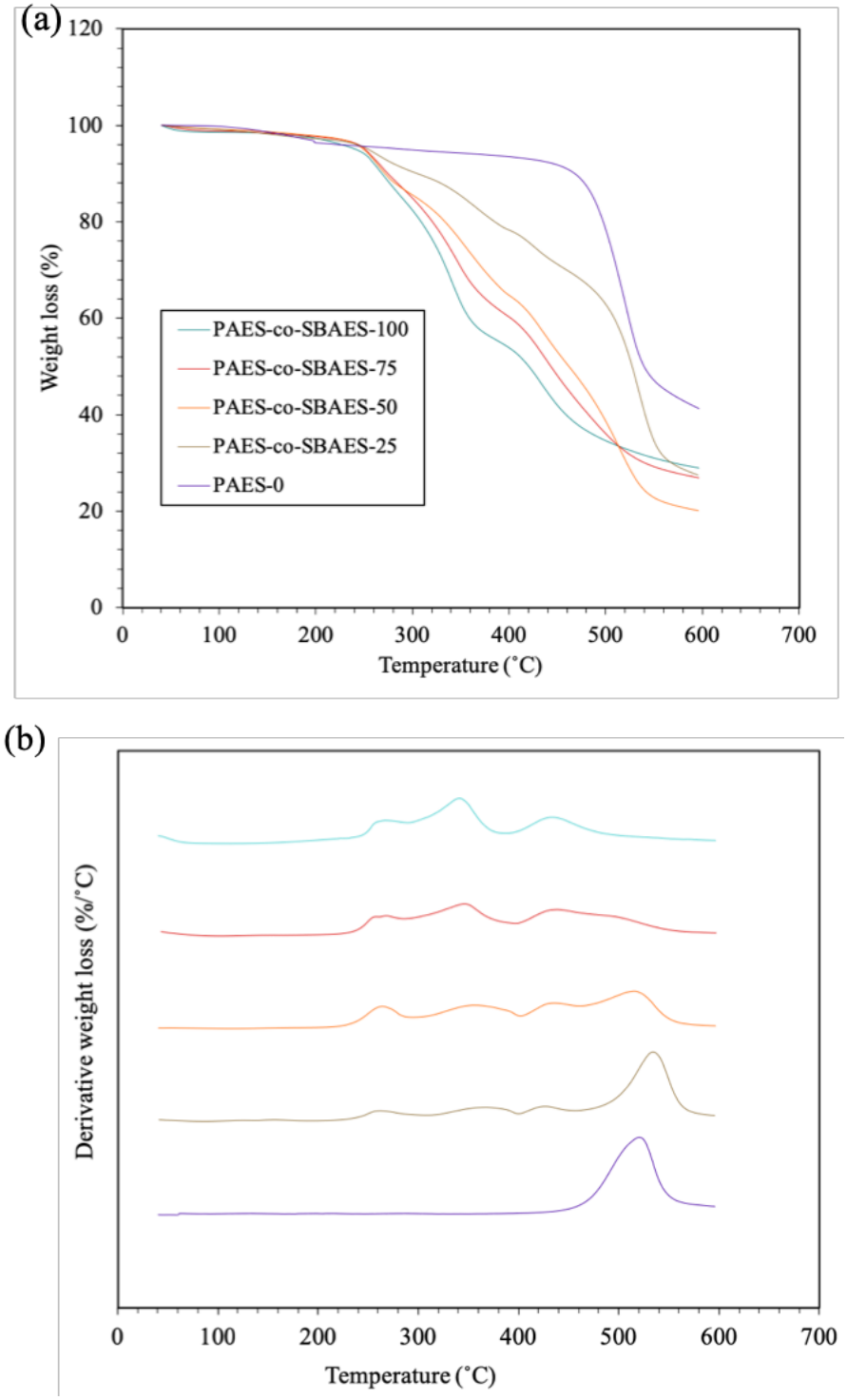

Figure 5.7. (a) Thermogravimetric analysis traces and the corresponding (b) differential thermal analysis traces of zwitterionic poly(arylene ether sulfone) copolymers (PAES-co-SBAES-XX, XX = 25~100), as well as the uncharged PAES (PAES-0).

To better understand the morphology of this novel zwitterionic copolymers, we measured

Tgs of the series of uncharged A-PAES and charged PAES-co-SBAES polymer films with DSC. Figure 5.8 shows the DSC heating traces recorded after annealing at high temperature (240 °C) for A-PAES-XX (Figure 5.8a) and at 220 ˚C for PAES-co-SBAES-XX (Figure 5.8b), respectively. As seen in Figure 5.8a, the glass transition of the A-PAES copolymers were all registered in lower T_gs than the value of the neat PAES at T_g = 170 ˚C. The initial incorporation of 25 mol% A-AES resulted no significant change of T_g. Further incorporation of allyl groups lowered the T_g of the copolymer significantly from 167 ˚C to 132 ˚C, indicating a plasticizing effect of the allyl group, which is increases free volume and facilitates the segmental mobility overall. Interestingly, after substituting with sulfobetaine side group, the copolymers, PAES-co-SBAES-XX, exhibits a splitting of T_g into an relatively lower T_g (i.e., $T_{g,1}$) than that of A-PAES with same content of pendant functionality (i.e., Tg,1 of PAES-co-SBAES-50 = 100 ˚C was lower than T_g of A-PAES-50 = 160˚C), and additional transitions started showing up at approximately $T_{g,2}$ = 240 ˚C, $T_{g,3}$ = 270 ˚C, respectively, as SBAES segment content increased up to 50 mol%, while the transition temperature ranges appear too close to the degradation temperature of the polymers to enable accurate interpretations. The splitting of T_g in amphiphilic polymers suggested that there was phase separation morphology for highly charged copolymer systems (i.e. IEC ≥ 1.45), where the lowest T_g was normally ascribed to the amorphous polymer matrix (i.e., uncharged PAES segments), while the relatively high T_g(s) were ascribed to the charged polymer phases due to the formation of physically crosslinking domains by the strong electrostatic interactions among the zwitterionic functionalities.43–45Attempts to analyze the morphology and any potential microphase separation are discussed below.

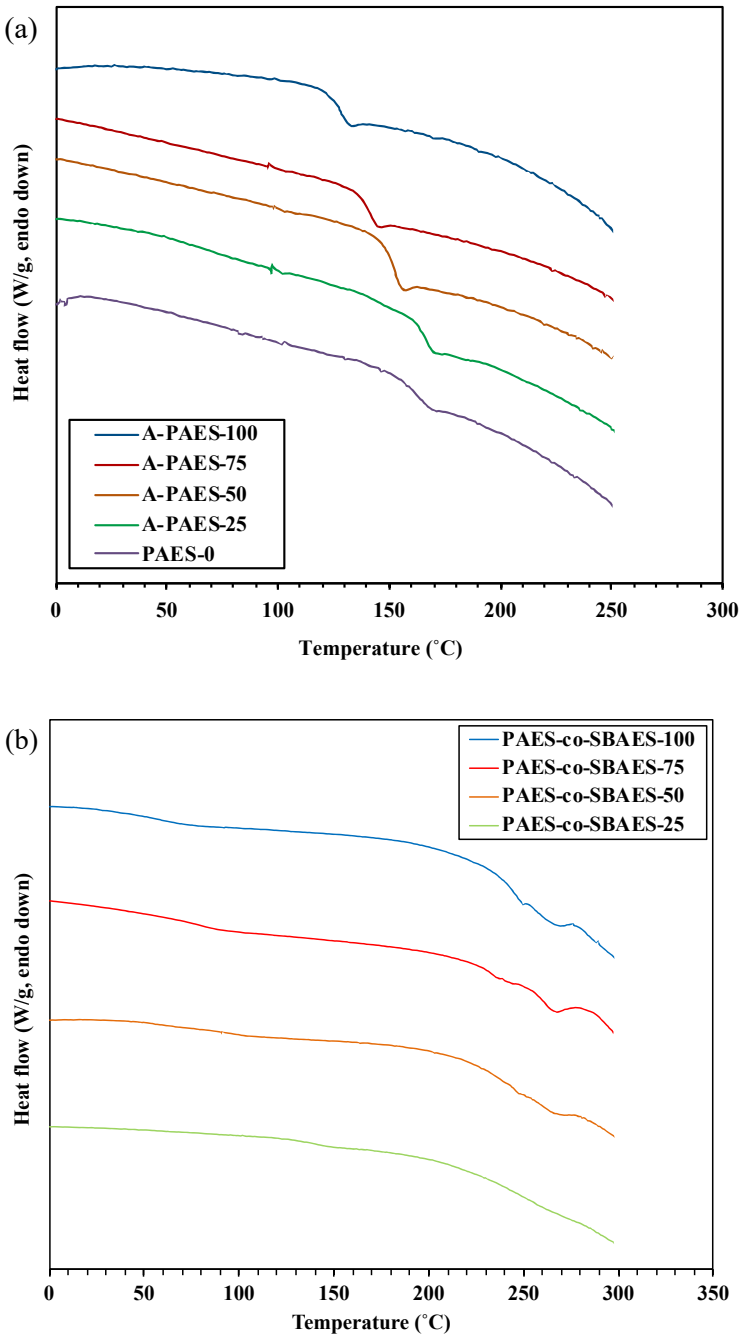

Figure 5.8. Differential scanning calorimetry temperature scan traces of (a) A-PAES-XX (XX = 0~100) copolymers, and (b) PAES-co-SBAES-XX (XX = 0~100) copolymers after annealing at 220 ˚C.

Notably, $T_{g,1}$ decreased drastically from 140 ˚C to 70 ˚C with the increased amount of

SBAES segment from 25 mol% to 100 mol%, indicating the length of the segments in uncharged amorphous domain became shorter–with higher segmental mobility–when there are more charged segments aggregating in the other separated domains. With the respect to the $T_{g,2}$ and $T_{g,3}$ at about 240 ˚C and 270 ˚C, respectively, showing up after SBAES contents ≥ 50 mol%, we speculated that it started forming intra- and/or intermolecular electrostatic interactions when the charge content went high enough and induced the charge aggregations.

5.3.4 X-ray Scattering

Figure 5.9 displays the room temperature X-ray scattering profiles for the series of PAES-co-SBAES-XX (XX = 0, 25, 50, 75, 100) copolymers. For charge-free PAES, a distinct high-angle scattering peak at q = 1.3 Å^{-1}, corresponding to a spacing $2\pi/q$ = 4.7 nm, primarily arises from amorphous backbone scattering. It is inferred that PAES-0 is completely amorphous and homogenous as evidenced by the absence of sharp unit cell reflections, which is consistent with the absence of a crystallization peak in the DSC curve (Figure 5.8a). The peak shifting slightly to a higher angle, or a smaller spacing, as a function of zwitterionic charge content, proved that increasing ionic content forces the polymer backbone-to-backbone spacing to be tightened, which is even more dominant than the steric effect on the spacing due to the addition of the pendent groups.

We observed that a new peak at $_q$ = 0.8 Å^{-1}, corresponding to a spacing of 7.8 Å ($d_{i,1}$), shows up after the zwitterionic charge is incorporated into the system, and the intensity of this peak started increasing when the charge content raised from 25 mol% to 75 mol%, then depressed slightly when it comes to the fully charged system (PAES-co-SBAES-100). Another new peak at q = 0.4 Å^{-1}, corresponding to a spacing of 16.2 Å ($d_{i,2}$), starts increasing gradually in

intensity with the increased zwitterionic charge content from 50 mol% to 100 mol%. Therefore, we hypothesize that the peak ($q_{i,1}$ = 0.8 Å^{-1}) is the intramolecular aggregate scattering peak for the charged copolymers (PAES-co-SBAES-XX, XX = 25, 50, 75, 100), while as the charge density keeps increasing, intermolecular ionic aggregation (at peak $q_{i,2}$ = 0.4 Å^{-1}) rises and eventually becomes more dominant than the intramolecular aggregation (Figure 5.9 and Figure 5.10). The low-angle upturn all shows up in each X-ray scattering profile, and is only indicative of random, long-range heterogeneity, the nature of which remains unclear but is ubiquitous to all ionomers.[183] This speculation is supported by the consistent tendency observed on the characteristic peaks of $T_{g,2}$ and $T_{g,3}$ in DSC curves (Figure 5.8b). Specifically, we speculated that the addition of zwitterionic charge first results in increased intensity of the highest glass transition temperature ($T_{g,3}$) plateau, which consistently corelates with intramolecular interacted aggregate with the most limited segmental mobility. When the zwitterionic charge content increased up to 50 mol% and higher, the intensity of the relatively lower glass transition temperature ($T_{g,2}$) plateau increases correspondingly, from which we speculated that intermolecular interaction rises, which nicely consists with the X-ray scattering results discussed above.

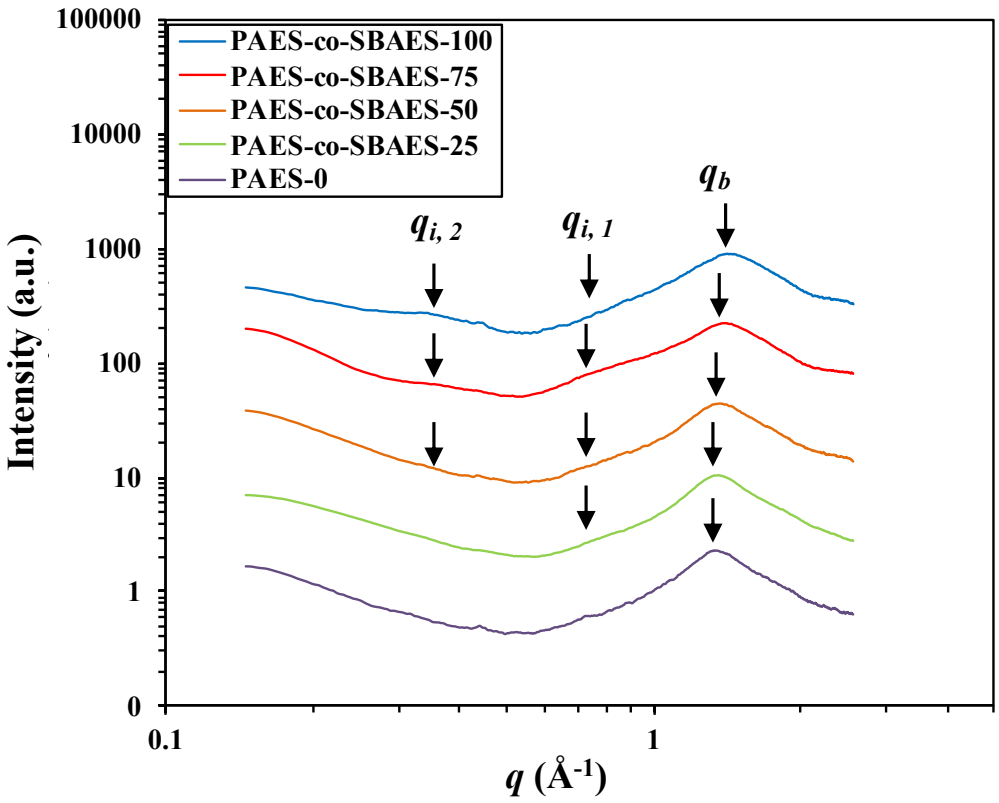

Figure 5.9. X-ray scattering intensity at room temperature as a function of scattering wavevector q for PAES-co-SBAES-XX (XX = 25, 50, 75, 100) and the control PAES-0. The data were exponentially smoothed with damping factor of 0.9, and the scales were shifted on the log scale for clarity.

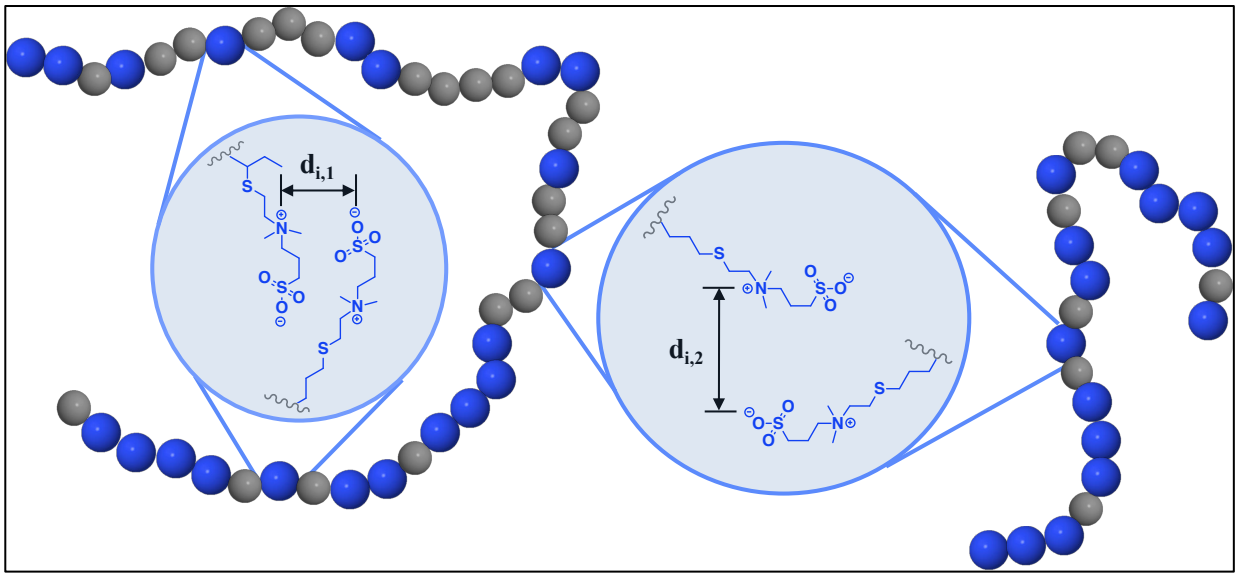

Figure 5.10. Schematic of two characteristic length scales as measured by X-ray scattering for PAES-co-SBAES-XX (XX = 25, 50, 75, 100), where $d_x = 2\pi/q_x$ and x is intramolecular (i,1) or intermolecular (i,2).

5.3.5 Mechanical property of the zwitterionic PAES copolymers

Polymeric materials have been well-known for their processability and scalability in various membrane applications, but for RO process specifically, the commercial PA based RO membranes are still being active only as a thin layer on top of a mechanically strong support layer.46–48 A robust and free-standing desalination membrane, therefore, provides much higher opportunities for easier scalability in terms of membrane casting techniques. The mechanical properties of the zwitterionic PAES copolymers were determined using a static strain rate compression test (Figure 5.11). The data plotted are representative of five individual runs for each SBAES segment content. Upon visual inspection, the sample had not yielded or deformed; these observations were consistent throughout the tensile testing. From the stress-strain curves, the Young's modulus were obtained as around 1 GPa as the slope of the stress-strain curve at low strain and showed no statistically significant difference as a function of the zwitterion contents (Figure 5.11).

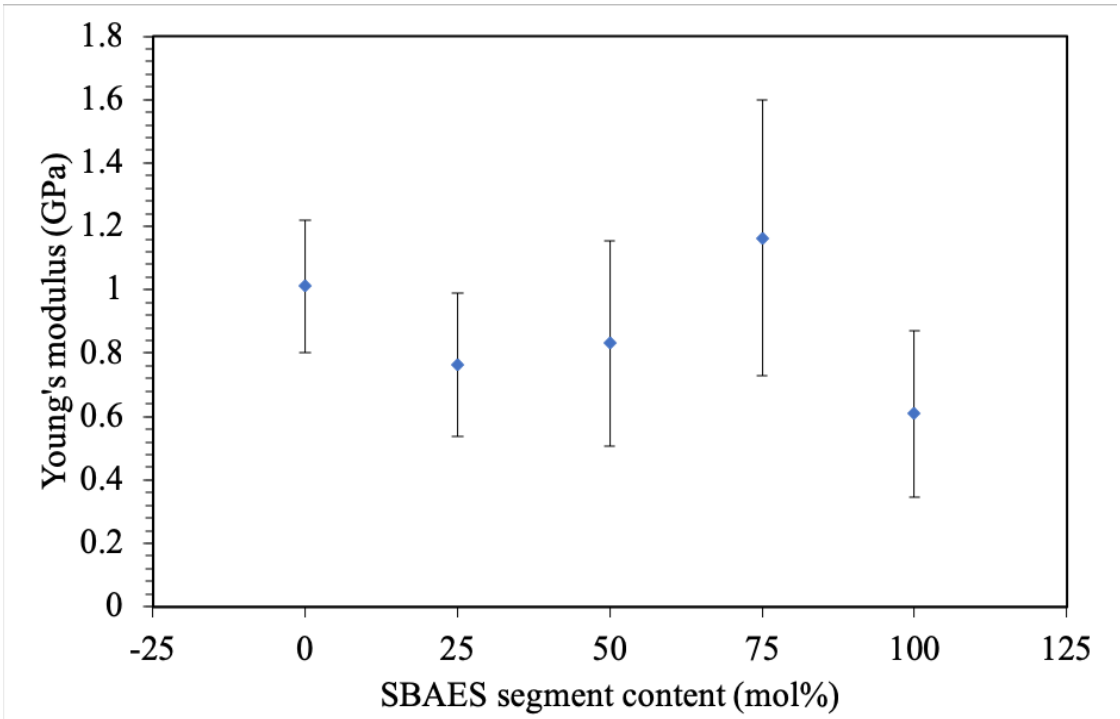

Figure 5.11. Young's modulus of the as-made PAES-co-SBAES-XX (XX = 0~100) copolymers based dense films.

5.4 Conclusion

Zwitterionic poly(arylene ether sulfone)s-based polymers showed promising capabilities on saline water desalination process, and had impressive chlorine resistance and anti-fouling properties even with relatively low loading of zwitterion charges. Optimized copolymer structures were proposed in this work for controlled high molecular weight (Mw ~ 65 kDa) and charge content (0~100 mol%), via off-set stoichiometry during polycondensations, following with thiol-ene click reaction and ring-opening of sultone to introduce the sulfobetaine functional groups. The effects of the reaction conditions on molecular weight and the crosslinking side-reaction of allyl groups were discussed. The series of zwitterionic PAES films were characterized on their thermal and mechanical properties (i.e. glass transition temperature (T_g),

degradation temperature ($T_{D,\,5\%}$), Young's modulus). The effects of the charge density on the phase separation morphology were further investigated via correlating the separated T_gs from DSC and the intermolecular and/or intramolecular ion aggregation behaviors detected from X-ray scattering, while additional validation is needed to confirm the phase separation behavior as speculated above.

Chapter 6: Conclusions and Recommendations

6.1 Concluding remarks

In this dissertation work, we firstly demonstrated a novel synthesis method to prepare an amphiphilic copolymer poly(arylene ether sulfone-co-sulfobetaine arylene ether sulfone) (PAES-co-SBAES), which was blended with native polysulfone (PSf) to prepare free standing, anti-fouling, and chemically robust membranes for the potential as a path forward for desalination. The hydrophilic SBAES segments gave the modified membranes with high surface hydrophilicity and high porosity in support layer, while the rigid PAES backbone and PSf provided mechanically strong matrix for the free-standing membranes. The water permeance and anti-fouling properties of the PSf/PAES-co-SBAES blend membranes were both drastically improved without compromising the salt rejection, which maintained in a high level. NIPS process in corporation of solvent evaporation for formation of an asymmetric membrane consisting of a defect-free dense thin layer on top of porous support is a feasible and consistent process that does not stray too far from conventional asymmetric membrane castings. Complete control over the solution conformation and the effect the zwitterions have upon the membrane morphology are still challenges to overcome, yet the current state-of-art still leaves spaces for this membrane technique in terms of easy fabrication and performance stability/durability as for a promising potential for brackish water desalination application. This work provided a valuable and scalable strategy to fabricate desalination membranes via the introduction of zwitterionic segments in a rigid polysulfone matrix.

An exciting finding of this dissertation work on the path for the structure design and optimization was that we discovered a new mechanism on polycondensation reactions of aryl

halides and bisphenol A. Based on our experiments on kinetics study and computational calculations, Aryl chlorides (ArCl) or aryl fluorides (ArF) were used in polycondensation reactions to form PAES. Interestingly, the kinetics of the ArF reaction fit a third-order rate law, which is attributed to the activation of the carbon-fluorine bond by two potassium cations (at least one bounded to phenolate), which associate as a strong three-body complex. The ArCl monomer instead follows a second-order reaction kinetics, where a potassium cation activated two-body complex was formed at the initial state of aromatic nucleophilic substitution (S_NAr) pathway. These metal cation-activated complex act as the predominant reactants during the attack by the nucleophile. In combination of experiments on reaction kinetics and the computational results by calculation with density functional theory (DFT) methods, the present work extends the fundamental understanding of polycondensation mechanisms for two aryl halide systems and highlights the importance of the CX--potassium interaction(s) in the S_NAr reaction. Such a finding may have ramifications across polycondensation research groups for enabling the better understanding of the fundamentals and also better controllability on chemical process parameters.

This dissertation also served as one of the first studies for optimizing the charged copolymer structures for linear high molecular weight and thus superior performances and scalability potentials. In this work, we developed a series of reaction parameters to controllably tailor the molecular weights and conversions of functionalized copolymers, which would enable the engineered parameters, i.e. reaction concentration, stoichiometric ratio, reaction temperature, monomer species, etc., for the targeted polymer structures and properties. This optimized synthetic route was rooted in thermodynamic fundamentals and would help identify which independent parameters are most critical when considering both kinetically favorable pathway on

polymer chain growth and thermodynamically favorable pathway on cross-linking side reaction. Even more excitingly after the optimized structure had been controllably obtained, the structure-property relationships were elucidated yielding a better understanding of the microstructure in the charged polymers which can enable the design of high-performance desalination membranes.

6.2 Future directions and recommendations

This thesis describes significant progress towards the possibility of using zwitterionic poly(arylene ether sulfone)s membrane platform as a promising desalination strategy. Preliminary desalination performances in terms of water flux and salt rejection pointed towards the possibility of using these membranes in brackish groundwater RO or NF desalinations. In addition, the membranes were estimated to be energetically favorable due to easy fabrication process, fouling resistance, and chemical stability. After the further explorations on the polymer structure optimizations, their fundamental synthetic mechanism, and the corresponding structure-micromorphology studies, the following recommendations may provide further insight for future work related to the development of high-performance desalination membrane platforms.

6.2.1 Fundamentally understanding of structure-property relationships

With the achievement on the linear high molecular weight zwitterionic charged PAES copolymers with tailorable charge density, it is a worthwhile option to further learn the relationships between charged structure and water/ion transport fundamentals. Herein it can be a clear guidance to potentially enhance the future membrane performances.[82,184–192] Specifically, how zwitterion or other charged functionalities associates with the confirmation of dope solution

and how the micromorphology of the polymers correlates to the small molecules/ions transport behaviors. These two questions can be answered in the future by investigating solution-diffusion model with combination of free-volume theory from experimental perspective.

6.2.2 Membrane development and platform exploration

In terms of future improvement of desalination membrane performances with the optimal structures designed, couple potential issues may be addressed as well. One is the ion aggregation behavior that is typically observed in unneutrally charged polymer systems and can reduce the effective charge functionalities, and thus the corresponding membrane properties.[193–204] Another opposite possibility is that even the current synthetic strategy can achieve charge density up to 100 mol% and the potential ion aggregation may not diminish the membrane performances dominantly, the swelling of the membranes by high charge loadings is undesired from practical stand of the point. An option is to incorporate chemical modifications on the polymers, such like crosslinking, or other membrane fabrication techniques.[129,205–210]

On the other hand, the current membrane design is mainly focused on using to desalination in RO process. While with a good choice of process platform, zwitterionic poly(arylene ether sulfone)s based membranes can also be developed for pervaporation (PV) applications, based on some preliminary results in our work that showed promising membrane transport properties of the zwitterion functionalized PAES copolymers under PV mode.

6.2.3 Estimating energetic consumption of the novel membranes

The primary goal of this work is to develop a competitive and scalable membrane technique for seawater RO desalinations. Therefore, extensive work is needed to estimate energy/cost of membrane processes and desalination. Most notably, the work here will focus on estimation of energy penalties and processing costs of the NIPS membrane for desalination and comparison to other technologies. Specifically, the intrinsic energy penalties include the consumption from the various synthetic parameters (i.e. the targeted molecular weight and charge density)[211] and process parameters (i.e. the amount of the feed solution, the applied pressure profile, and reusability).[212,213] In addition, when it comes to extension for large-scale applications such as spiral wound[214,215] and hollow fiber desalination plants[5,216,217], auxiliary energy penalties are also necessary to be considered. Pretreatment and post-treatment expenses for RO desalination cycle will also have a substantial reduction when considering biofouling, scaling, and membrane deterioration diminished by superior membrane performances. This overall estimation of energy consumption for desalination, cooperating with single-step NIPS casting technique for our free-standing charged polysulfone-based membranes, will guide future research by pointing to areas within the chemistry and processes that can be optimized, either energetically, or from a capital expenditures perspective.

REFERENCE

(1) Shannon, M. A.; Bohn, P. W.; Elimelech, M.; Georgiadis, J. G.; Marĩas, B. J.; Mayes, A. M. Science and Technology for Water Purification in the Coming Decades. *Nature*. 2008, pp 301–310. https://doi.org/10.1038/nature06599.

(2) Semiat, R. Energy Issues in Desalination Processes. *Environmental Science and Technology*. 2008, pp 8193–8201. https://doi.org/10.1021/es801330u.

(3) Anderson, M. A.; Cudero, A. L.; Palma, J. Capacitive Deionization as an Electrochemical Means of Saving Energy and Delivering Clean Water. Comparison to Present Desalination Practices: Will It Compete? *Electrochimica Acta*. 2010, pp 3845–3856. https://doi.org/10.1016/j.electacta.2010.02.012.

(4) Schiermeier, Q. The Parched Planet: Water on Tap. *Nature* **2014**, *510* (7505), 326–328. https://doi.org/10.1038/510326a.

(5) Greenlee, L. F.; Lawler, D. F.; Freeman, B. D.; Marrot, B.; Moulin, P. Reverse Osmosis Desalination: Water Sources, Technology, and Today's Challenges. *Water Research*. 2009, pp 2317–2348. https://doi.org/10.1016/j.watres.2009.03.010.

(6) Brown, R. D. Northern Hemisphere Snow Cover Variability and Change , 1915 – 97. *J. Clim.* **2000**, *13* (2000), 2339–2355. https://doi.org/10.1175/1520-0442(2000)013<2339:NHSCVA>2.0.CO;2.

(7) Singh, R. Worldwide Water Crisis. *Journal of Membrane Science*. 2008, pp 353–354. https://doi.org/10.1016/j.memsci.2008.01.016.

(8) Maupin, M. A.; Kenny, J. F.; Hutson, S. S.; Lovelace, J. K.; Barber, N. L.; Linsey, K. S. *Estimated Use of Water in the United States in 2010 Circular 1405*; 2010; Vol. 1405. https://doi.org/http://dx.doi.org/10.3133/cir1405.

(9) Oki, T.; Kanae, S. Global Hydrological Cycles and World Water Resources. *Science*. 2006, pp 1068–1072. https://doi.org/10.1126/science.1128845.

(10) Gleick, P. Water in Crisis: Paths to Sustainable Water Use. *Ecol. Appl.* **1998**, *8* (August), 571–579. https://doi.org/10.1890/1051-0761(1998)008[0571:WICPTS]2.0.CO;2.

(11) Döll, P.; Hoffmann-Dobrev, H.; Portmann, F. T.; Siebert, S.; Eicker, A.; Rodell, M.; Strassberg, G.; Scanlon, B. R. Impact of Water Withdrawals from Groundwater and Surface Water on Continental Water Storage Variations. *J. Geodyn.* **2012**, *59–60*, 143–156. https://doi.org/10.1016/j.jog.2011.05.001.

(12) Wang, Q.; Li, S.; Jia, P.; Qi, C.; Ding, F. A Review of Surface Water Quality Models. *ScientificWorldJournal.* **2013**, *2013*, 231768. https://doi.org/10.1155/2013/231768.

(13) Aeschbach-Hertig, W.; Gleeson, T. Regional Strategies for the Accelerating Global

Problem of Groundwater Depletion. *Nature Geoscience*. 2012, pp 853–861. https://doi.org/10.1038/ngeo1617.

(14) Gleeson, T.; Wada, Y.; Bierkens, M. F. P.; Van Beek, L. P. H. Water Balance of Global Aquifers Revealed by Groundwater Footprint. *Nature* **2012**, *488* (7410), 197–200. https://doi.org/10.1038/nature11295.

(15) Karl, T. R.; Melillo, J. M.; Peterson, T. C. *Global Climate Change Impacts in the United States*; 2009; Vol. 54.

(16) Webb, R. H.; Leake, S. A. Ground-Water Surface-Water Interactions and Long-Term Change in Riverine Riparian Vegetation in the Southwestern United States. In *Journal of Hydrology*; 2006; Vol. 320, pp 302–323. https://doi.org/10.1016/j.jhydrol.2005.07.022.

(17) Elimelech, M.; Phillip, W. A. The Future of Seawater Desalination: Energy, Technology, and the Environment. *Science (80-.).* **2011**, *333* (6043), 712–717. https://doi.org/10.1126/science.1200488.

(18) Ratnayaka, D. D.; Brandt, M. J.; Johnson, K. M. *Water Supply*; 2009. https://doi.org/10.1016/B978-0-7506-6843-9.00026-3.

(19) Song, X.; Liu, Z.; Sun, D. D. Energy Recovery from Concentrated Seawater Brine by Thin-Film Nanofiber Composite Pressure Retarded Osmosis Membranes with High Power Density. *Energy Environ. Sci.* **2013**, *6* (4), 1199. https://doi.org/10.1039/c3ee23349a.

(20) Lee, K. P.; Arnot, T. C.; Mattia, D. A Review of Reverse Osmosis Membrane Materials for Desalination-Development to Date and Future Potential. *Journal of Membrane Science*. 2011, pp 1–22. https://doi.org/10.1016/j.memsci.2010.12.036.

(21) Wentz, F. J.; Ricciardulli, L.; Hilburn, K.; Mears, C. How Much More Rain Will Global Warming Bring? *Science (80-.).* **2007**, *317* (5835), 233–235. https://doi.org/10.1126/science.1140746.

(22) Henthorne, L.; Boysen, B. State-of-the-Art of Reverse Osmosis Desalination Pretreatment. *Desalination*. 2015, pp 129–139. https://doi.org/10.1016/j.desal.2014.10.039.

(23) UN Water. *Coping With Water Scarcity - Challenge of the Twenty-First Century*; 2007.

(24) Gleick, P. H. Water in Crisis: Paths to Sustainable Water Use. *Ecol. Appl.* **1998**. https://doi.org/10.1890/1051-0761(1998)008[0571:WICPTS]2.0.CO;2.

(25) Afonso, M. D.; Jaber, J. O.; Mohsen, M. S. Brackish Groundwater Treatment by Reverse Osmosis in Jordan. *Desalination* **2004**. https://doi.org/10.1016/S0011-9164(04)00175-4.

(26) Alkhudhiri, A.; Darwish, N.; Hilal, N. Membrane Distillation: A Comprehensive Review. *Desalination*. 2012, pp 2–18. https://doi.org/10.1016/j.desal.2011.08.027.

(27) Shao, P.; Huang, R. Y. M. Polymeric Membrane Pervaporation. *Journal of Membrane*

Science. 2007, pp 162–179. https://doi.org/10.1016/j.memsci.2006.10.043.

(28) Ong, Y. K.; Shi, G. M.; Le, N. L.; Tang, Y. P.; Zuo, J.; Nunes, S. P.; Chung, T. S. Recent Membrane Development for Pervaporation Processes. *Prog. Polym. Sci.* **2016**, *57*, 1–31. https://doi.org/10.1016/j.progpolymsci.2016.02.003.

(29) Cath, T. Y.; Childress, A. E.; Elimelech, M. Forward Osmosis: Principles, Applications, and Recent Developments. *Journal of Membrane Science*. 2006, pp 70–87. https://doi.org/10.1016/j.memsci.2006.05.048.

(30) Lee, K. P.; Arnot, T. C.; Mattia, D. A Review of Reverse Osmosis Membrane Materials for Desalination-Development to Date and Future Potential. *J. Memb. Sci.* **2011**, *370* (1–2), 1–22. https://doi.org/10.1016/j.memsci.2010.12.036.

(31) Baker, R. W. *Membrane Technology and Applications*; 2012. https://doi.org/10.1016/S0958-2118(96)90133-0.

(32) Imbrogno, J.; Keating, J. J.; Kilduff, J.; Belfort, G. Critical Aspects of RO Desalination: A Combination Strategy. *Desalination* **2017**, *401*, 68–87. https://doi.org/10.1016/j.desal.2016.06.033.

(33) Valladares Linares, R.; Li, Z.; Sarp, S.; Bucs, S. S.; Amy, G.; Vrouwenvelder, J. S. Forward Osmosis Niches in Seawater Desalination and Wastewater Reuse. *Water Research*. 2014. https://doi.org/10.1016/j.watres.2014.08.021.

(34) Zhu, A.; Rahardianto, A.; Christofides, P. D.; Cohen, Y. Reverse Osmosis Desalination with High Permeability Membranes — Cost Optimization and Research Needs. *Desalin. Water Treat.* **2010**. https://doi.org/10.5004/dwt.2010.1763.

(35) Yin, J.; Deng, B. Polymer-Matrix Nanocomposite Membranes for Water Treatment. *J. Memb. Sci.* **2015**, *479*, 256–275. https://doi.org/10.1016/j.memsci.2014.11.019.

(36) Werber, J. R.; Osuji, C. O.; Elimelech, M. Materials for Next-Generation Desalination and Water Purification Membranes. *Nat. Rev. Mater.* **2016**, *1* (5), 16018. https://doi.org/10.1038/natrevmats.2016.18.

(37) Ma, R.; Ji, Y. L.; Weng, X. D.; An, Q. F.; Gao, C. J. High-Flux and Fouling-Resistant Reverse Osmosis Membrane Prepared with Incorporating Zwitterionic Amine Monomers via Interfacial Polymerization. *Desalination* **2016**, *381*, 100–110. https://doi.org/10.1016/j.desal.2015.11.023.

(38) Ye, G.; Lee, J.; Perreault, F.; Elimelech, M. Controlled Architecture of Dual-Functional Block Copolymer Brushes on Thin-Film Composite Membranes for Integrated "Defending" and "Attacking" Strategies against Biofouling. *ACS Appl. Mater. Interfaces* **2015**, *7* (41), 23069–23079. https://doi.org/10.1021/acsami.5b06647.

(39) Yang, R.; Xu, J.; Ozaydin-Ince, G.; Wong, S. Y.; Gleason, K. K. Surface-Tethered Zwitterionic Ultrathin Antifouling Coatings on Reverse Osmosis Membranes by Initiated

Chemical Vapor Deposition. *Chem. Mater.* **2011**, *23* (5), 1263–1272. https://doi.org/10.1021/cm1031392.

(40) McCutcheon, J. R. Avoiding the Hype in Developing Commercially Viable Desalination Technologies. *Joule* **2019**. https://doi.org/10.1016/J.JOULE.2019.03.005.

(41) Sablani, S.; Goosen, M.; Al-Belushi, R.; Wilf, M. Concentration Polarization in Ultrafiltration and Reverse Osmosis: A Critical Review. *Desalination* **2001**. https://doi.org/10.1016/S0011-9164(01)85005-0.

(42) Herzberg, M.; Elimelech, M. Biofouling of Reverse Osmosis Membranes: Role of Biofilm-Enhanced Osmotic Pressure. *J. Memb. Sci.* **2007**. https://doi.org/10.1016/j.memsci.2007.02.024.

(43) Verbeke, R.; Gómez, V.; Vankelecom, I. F. J. Chlorine-Resistance of Reverse Osmosis (RO) Polyamide Membranes. *Prog. Polym. Sci.* **2017**, *72*, 1–15. https://doi.org/10.1016/j.progpolymsci.2017.05.003.

(44) Glater, J.; Hong, S. kwan; Elimelech, M. The Search for a Chlorine-Resistant Reverse Osmosis Membrane. *Desalination* **1994**. https://doi.org/10.1016/0011-9164(94)00068-9.

(45) Shin, D. H.; Kim, N.; Lee, Y. T. Modification to the Polyamide TFC RO Membranes for Improvement of Chlorine-Resistance. *J. Memb. Sci.* **2011**. https://doi.org/10.1016/j.memsci.2011.04.045.

(46) Gohil, J. M.; Suresh, A. K. Chlorine Attack on Reverse Osmosis Membranes: Mechanisms and Mitigation Strategies. *Journal of Membrane Science*. 2017. https://doi.org/10.1016/j.memsci.2017.06.092.

(47) Phillip, W. A.; Schiffman, J. D.; Elimelech, M. High Performance Thin-Film Membrane. **2010**, *44* (10), 3812–3818.

(48) Zodrow, K.; Brunet, L.; Mahendra, S.; Li, D.; Zhang, A.; Li, Q.; Alvarez, P. J. J. Polysulfone Ultrafiltration Membranes Impregnated with Silver Nanoparticles Show Improved Biofouling Resistance and Virus Removal. *Water Res.* **2009**, *43* (3), 715–723. https://doi.org/10.1016/j.watres.2008.11.014.

(49) Tang, L.; Livi, K. J. T.; Chen, K. L. Polysulfone Membranes Modified with Bioinspired Polydopamine and Silver Nanoparticles Formed in Situ to Mitigate Biofouling. *Environ. Sci. Technol. Lett.* **2015**, *2* (3), 59–65. https://doi.org/10.1021/acs.estlett.5b00008.

(50) Zhao, C.; Xue, J.; Ran, F.; Sun, S. Modification of Polyethersulfone Membranes - A Review of Methods. *Prog. Mater. Sci.* **2013**, *58* (1), 76–150. https://doi.org/10.1016/j.pmatsci.2012.07.002.

(51) Park, H. B.; Freeman, B. D.; Zhang, Z. B.; Sankir, M.; McGrath, J. E. Highly Chlorine-Tolerant Polymers for Desalination. *Angew. Chemie - Int. Ed.* **2008**, *47* (32), 6019–6024. https://doi.org/10.1002/anie.200800454.

(52) Ren, J.; O'Grady, B.; deJesus, G.; McCutcheon, J. R. Sulfonated Polysulfone Supported High Performance Thin Film Composite Membranes for Forward Osmosis. *Polym. (United Kingdom)* **2016**, *103*, 486–497. https://doi.org/10.1016/j.polymer.2016.02.058.

(53) Kumar, M.; Ulbricht, M. Novel Ultrafiltration Membranes with Adjustable Charge Density Based on Sulfonated Poly(Arylene Ether Sulfone) Block Copolymers and Their Tunable Protein Separation Performance. *Polym. (United Kingdom)* **2014**, *55* (1), 354–365. https://doi.org/10.1016/j.polymer.2013.09.003.

(54) Lee, C. H.; McCloskey, B. D.; Cook, J.; Lane, O.; Xie, W.; Freeman, B. D.; Lee, Y. M.; McGrath, J. E. Disulfonated Poly(Arylene Ether Sulfone) Random Copolymer Thin Film Composite Membrane Fabricated Using a Benign Solvent for Reverse Osmosis Applications. *J. Memb. Sci.* **2012**, *389*, 363–371. https://doi.org/10.1016/j.memsci.2011.11.001.

(55) Paul, M.; Park, H. B.; Freeman, B. D.; Roy, A.; McGrath, J. E.; Riffle, J. S. Synthesis and Crosslinking of Partially Disulfonated Poly(Arylene Ether Sulfone) Random Copolymers as Candidates for Chlorine Resistant Reverse Osmosis Membranes. *Polymer (Guildf).* **2008**, *49* (9), 2243–2252. https://doi.org/10.1016/j.polymer.2008.02.039.

(56) Cassady, H. J.; Cimino, E. C.; Kumar, M.; Hickner, M. A. Specific Ion Effects on the Permselectivity of Sulfonated Poly(Ether Sulfone) Cation Exchange Membranes. *J. Memb. Sci.* **2016**, *508*, 146–152. https://doi.org/10.1016/j.memsci.2016.02.048.

(57) Kricheldorf, H. R. What Does Polycondensation Mean? In *Macromolecular Symposia*; 2003; Vol. 199, pp 1–13. https://doi.org/10.1002/masy.200350901.

(58) Martinez, C. A.; Hay, A. S. Synthesis of Dendritic-Linear Copoly(Arylene Ether)s from a Linear Copolymer Core. *Polymer (Guildf).* **2002**. https://doi.org/10.1016/S0032-3861(02)00527-X.

(59) Robello, D. R.; Ulman, A.; Urankar, E. J. Poly(p-Phenylene Sulfone). *Macromolecules* **1993**. https://doi.org/10.1021/ma00077a004.

(60) Zhao, C.; Xue, J.; Ran, F.; Sun, S. Modification of Polyethersulfone Membranes - A Review of Methods. *Prog. Mater. Sci.* **2013**, *58* (1), 76–150. https://doi.org/10.1016/j.pmatsci.2012.07.002.

(61) Kricheldorf, H. R.; Vakhtangishvili, L.; Fritsch, D. Synthesis and Functionalization of Poly(Ether Sulfone)s Based on 1,1,1-Tris(4-Hydroxyphenyl)Ethane. *J. Polym. Sci. Part A Polym. Chem.* **2002**, *40* (17), 2967–2978. https://doi.org/10.1002/pola.10372.

(62) Noshay, A.; Robeson, L. M. Sulfonated Polysulfone. *J. Appl. Polym. Sci.* **1976**, *20* (7), 1885–1903. https://doi.org/10.1002/app.1976.070200717.

(63) Wang, F.; Glass, T.; Li, X.; Hickner, M.; Kim, Y. S.; McGrath, J. Synthesis and Characterization of Controlled Molecular Weight Poly(Arylene Ether Sulfone) Copolymers Bearing Sulfonate Groups by Endgroup Analysis. In *American Chemical*

Society, Polymer Preprints, Division of Polymer Chemistry; 2002; Vol. 43, pp 492–493.

(64) Harrison, W. L.; O'Connor, K.; Arnett, N.; McGrath, J. E. Homogeneous Synthesis and Characterization of Sulfonated Poly(Arylene Ether Sulfone)s via Chlorosulfonic Acid. In *American Chemical Society, Polymer Preprints, Division of Polymer Chemistry*; 2002; Vol. 43, p 1159.

(65) Johnson, B. C.; Yilgör, İ.; Tran, C.; Iqbal, M.; Wightman, J. P.; Lloyd, D. R.; McGrath, J. E. Synthesis and Characterization of Sulfonated Poly(Acrylene Ether Sulfones). *J. Polym. Sci. Polym. Chem. Ed.* **1984**, *22* (3), 721–737. https://doi.org/10.1002/pol.1984.170220320.

(66) Robeson, L. M.; Farnham, A. G.; McGrath, J. E. Synthesis and Dynamic Mechanical Characteristics of Poly(Aryl Ethers). *Appl. Polym. Symp.* **1975**, *26* (polym. polycondensat), 375–385.

(67) Dennis, J. M.; Fahs, G. B.; Moore, R. B.; Turner, S. R.; Long, T. E. Synthesis and Characterization of Polysulfone-Containing Poly(Butylene Terephthalate) Segmented Block Copolymers. *Macromolecules* **2014**, *47* (23), 8171–8177. https://doi.org/10.1021/ma501903h.

(68) Duncan, A. J.; Layman, J. M.; Cashion, M. P.; Leo, D. J.; Long, T. E. Oligomeric A2+ B3synthesis of Highly Branched Polysulfone Ionomers: Novel Candidates for Ionic Polymer Transducers. *Polym. Int.* **2010**, *59* (1), 25–35. https://doi.org/10.1002/pi.2684.

(69) Suga, T.; Wi, S.; Long, T. E. Synthesis of Diazocine-Containing Poly(Arylene Ether Sulfone)s for Tailored Mechanical and Electrochemical Performance. *Macromolecules* **2009**, *42* (5), 1526–1532. https://doi.org/10.1021/ma802249a.

(70) Kricheldorf, H. R.; Böhme, S.; Schwarz, G.; Krüger, R. P.; Schulz, G. Macrocycles. 18. The Role of Cyclization in Syntheses of Poly(Ether-Sulfone)S. *Macromolecules* **2001**, *34* (26), 8886–8893. https://doi.org/10.1021/ma010218l.

(71) Sahre, K.; Hoffmann, T.; Pospiech, D.; Eichhorn, K. J.; Fischer, D.; Voit, B. Monitoring of the Polycondensation Reaction of Bisphenol A and 4,4′-Dichlorodiphenylsulfone towards Polysulfone (PSU) by Real-Time ATR-FTIR Spectroscopy. *Eur. Polym. J.* **2006**, *42* (10), 2292–2301. https://doi.org/10.1016/j.eurpolymj.2006.05.025.

(72) Jennings, B. E.; Jones, M. E. B.; Rose, J. B. Synthesis of Poly(Arylene Sulfones) and Poly(Arylene Ketones) by Reactions Involving Substitution at Aromatic Nuclei. *J. Polym. Sci. Polym. Symp.* **1967**, *16* (Pt. 2), 715–724. https://doi.org/10.1002/polc.5070160212.

(73) Bunnett, J. F. Aromatic Substitution by the SRN1 Mechanism. *Acc. Chem. Res.* **1978**, *11* (11), 413–420. https://doi.org/10.1021/ar50131a003.

(74) Bunnett, J. F.; Zahler, R. E. Aromatic Nucleophilic Substitution Reactions. *Chem. Rev.* **1951**, *49* (2), 273–412. https://doi.org/10.1021/cr60153a002.

(75) Servis, K. L. Nuclear Magnetic Resonance Studies of Meisenheimer Complexes. *J. Am. Chem. Soc.* **1967**. https://doi.org/10.1021/ja00982a039.

(76) Ganguly, S.; Gibson, H. W. Synthesis of a Novel Macrocyclic Arylene Ether Sulfone. *Macromolecules* **1993**, *26* (10), 2408–2412. https://doi.org/10.1021/ma00062a003.

(77) Viswanathan, R.; Johnson, B. C.; McGrath, J. E. Synthesis, Kinetic Observations and Characteristics of Polyarylene Ether Sulphones Prepared via a Potassium Carbonate DMAC Process. *Polymer (Guildf).* **1984**, *25* (12), 1827–1836. https://doi.org/10.1016/0032-3861(84)90258-1.

(78) Hale, W. F.; Farnham, A. G.; Johnson, R. N.; Clendinning, R. A. Poly(Aryl Ethers) by Nucleophilic Aromatic Substitution. II. Thermal Stability. *J. Polym. Sci. Part A-1 Polym. Chem.* **1967**. https://doi.org/10.1002/pol.1967.150050917.

(79) Nebipasagil, A.; Park, J.; Lane, O. R.; Sundell, B. J.; Mecham, S. J.; Freeman, B. D.; Riffle, J. S.; McGrath, J. E. Polyurethanes Containing Poly(Arylene Ether Sulfone) and Poly(Ethylene Oxide) Segments for Gas Separation Membranes. *Polymer (Guildf).* **2017**. https://doi.org/10.1016/j.polymer.2017.03.017.

(80) Wijmans, J. G.; Baker, R. W. The Solution-Diffusion Model: A Review. *Journal of Membrane Science*. 1995, pp 1–21. https://doi.org/10.1016/0376-7388(95)00102-I.

(81) Verliefde, A. R. D.; Meeren, P. Van Der; Bruggen, B. Van Der. Solution-Diffusion Processes. In *Encyclopedia of Membrane Science and Technology*; 2013; pp 1–26. https://doi.org/10.1002/9781118522318.emst017.

(82) Geise, G. M.; Paul, D. R.; Freeman, B. D. Fundamental Water and Salt Transport Properties of Polymeric Materials. *Progress in Polymer Science*. 2014, pp 1–24. https://doi.org/10.1016/j.progpolymsci.2013.07.001.

(83) Yasuda, H.; Lamaze, C.; Ikenberry, L. D. Permeability of Solutes through Hydrated Polymer Membranes. Part I. Diffusion of Sodium Chloride. *Die Makromol. Chemie* **1968**, *118* (3086), 19–35. https://doi.org/10.1002/macp.1968.021180102.

(84) Lind, M. L.; Jeong, B.-H.; Subramani, A.; Huang, X.; Hoek, E. M. V. Effect of Mobile Cation on Zeolite-Polyamide Thin Film Nanocomposite Membranes. *J. Mater. Res.* **2009**, *24* (05), 1624–1631. https://doi.org/10.1557/jmr.2009.0189.

(85) Yadav, A.; Lind, M. L.; Ma, X.; Lin, Y. S. Nanocomposite Silicalite-1/Polydimethylsiloxane Membranes for Pervaporation of Ethanol from Dilute Aqueous Solutions. *Ind. Eng. Chem. Res.* **2013**, *52* (14), 5207–5212. https://doi.org/10.1021/ie303240f.

(86) Mahajan, R.; Koros, W. J. Mixed Matrix Membrane Materials with Glassy Polymers. Part 1. *Polym. Eng. Sci.* **2002**, *42* (7), 1420–1431. https://doi.org/10.1002/pen.11041.

(87) Wang, J.; Dlamini, D. S.; Mishra, A. K.; Pendergast, M. T. M.; Wong, M. C. Y.; Mamba,

B. B.; Freger, V.; Verliefde, A. R. D.; Hoek, E. M. V. A Critical Review of Transport through Osmotic Membranes. *J. Memb. Sci.* **2014**, *454*, 516–537. https://doi.org/10.1016/j.memsci.2013.12.034.

(88) Van Der Bruggen, B.; Vandecasteele, C.; Van Gestel, T.; Doyen, W.; Leysen, R. A Review of Pressure-Driven Membrane Processes in Wastewater Treatment and Drinking Water Production. *Environ. Prog.* **2003**. https://doi.org/10.1002/ep.670220116.

(89) Cheryan, M. *Ultrafiltration and Microfiltration Handbook*; 2018. https://doi.org/10.1201/9781482278743.

(90) Liu, Y.; Wang, G. Membranes: Technology and Applications. In *Nanostructured Polymer Membranes*; 2016. https://doi.org/10.1002/9781118831823.ch2.

(91) Madaeni, S. S. Nanofiltration Membranes. In *Encyclopedia of Membranes*; 2015. https://doi.org/10.1007/978-3-642-40872-4_2207-1.

(92) Maruf, S. H.; Greenberg, A. R.; Ding, Y. Influence of Substrate Processing and Interfacial Polymerization Conditions on the Surface Topography and Permselective Properties of Surface-Patterned Thin-Film Composite Membranes. *J. Memb. Sci.* **2016**. https://doi.org/10.1016/j.memsci.2016.04.003.

(93) Jun, B. M.; Kim, S. H.; Kwak, S. K.; Kwon, Y. N. Effect of Acidic Aqueous Solution on Chemical and Physical Properties of Polyamide NF Membranes. *Appl. Surf. Sci.* **2018**. https://doi.org/10.1016/j.apsusc.2018.03.078.

(94) Baker, R. W. *Membrane Technology and Applications*; 2012. https://doi.org/10.1016/S0958-2118(96)90133-0.

(95) Lloyd, D. R.; Kim, S. S.; Kinzer, K. E. Microporous Membrane Formation via Thermally-Induced Phase Separation. II. Liquid-Liquid Phase Separation. *J. Memb. Sci.* **1991**, *64* (1–2), 1–11. https://doi.org/10.1016/0376-7388(91)80073-F.

(96) Feng, Q.; Wu, D.; Zhao, Y.; Wei, A.; Wei, Q.; Fong, H. Electrospun AOPAN/RC Blend Nanofiber Membrane for Efficient Removal of Heavy Metal Ions from Water. *J. Hazard. Mater.* **2018**. https://doi.org/10.1016/j.jhazmat.2017.11.035.

(97) Wang, M.; Xi, X.; Gong, C.; Zhang, X. L.; Fan, G. Open Porous BiVO4 Nanomaterials: Electronspinning Fabrication and Enhanced Visible Light Photocatalytic Activity. *Mater. Res. Bull.* **2016**. https://doi.org/10.1016/j.materresbull.2015.10.051.

(98) Baji, A.; Mai, Y. W.; Wong, S. C.; Abtahi, M.; Chen, P. Electrospinning of Polymer Nanofibers: Effects on Oriented Morphology, Structures and Tensile Properties. *Composites Science and Technology*. 2010. https://doi.org/10.1016/j.compscitech.2010.01.010.

(99) Chen, P.; Wu, H.; Yuan, T.; Zou, Z.; Zhang, H.; Zheng, J.; Yang, H. Electronspun Nanofiber Network Anode for a Passive Direct Methanol Fuel Cell. *J. Power Sources*

2014. https://doi.org/10.1016/j.jpowsour.2013.12.130.

(100) Ahmed, F. E.; Lalia, B. S.; Hashaikeh, R. A Review on Electrospinning for Membrane Fabrication: Challenges and Applications. *Desalination*. 2015. https://doi.org/10.1016/j.desal.2014.09.033.

(101) Matthews, J. A.; Wnek, G. E.; Simpson, D. G.; Bowlin, G. L. Electrospinning of Collagen Nanofibers. *Biomacromolecules* **2002**. https://doi.org/10.1021/bm015533u.

(102) Dalton, P. D.; Grafahrend, D.; Klinkhammer, K.; Klee, D.; Möller, M. Electrospinning of Polymer Melts: Phenomenological Observations. *Polymer (Guildf).* **2007**. https://doi.org/10.1016/j.polymer.2007.09.037.

(103) Aljehani, A. K.; Hussaini, M. A.; Hussain, M. A.; Alothmany, N. S.; Aldhaheri, R. W. Effect of Electrospinning Parameters on Nanofiber Diameter Made of Poly (Vinyl Alcohol) as Determined by Atomic Force Microscopy. In *Middle East Conference on Biomedical Engineering, MECBME*; 2014. https://doi.org/10.1109/MECBME.2014.6783283.

(104) Quinn, J. A.; Yang, Y.; Buffington, A. N.; Romero, F. N.; Green, M. D. Preparation and Characterization of Crosslinked Electrospun Poly(Vinyl Alcohol) Nanofibrous Membranes. *Polymer (Guildf).* **2018**. https://doi.org/10.1016/j.polymer.2017.11.023.

(105) Hong, H. R.; Tronstad, Z. C.; Yang, Y.; Green, M. D. Characterization of PVC-Soy Protein Nonwoven Mats Prepared by Electrospinning. *AIChE J.* **2018**. https://doi.org/10.1002/aic.16109.

(106) Elimelech, M.; Zhu, X.; Childress, A. E.; Hong, S. Role of Membrane Surface Morphology in Colloidal Fouling of Cellulose Acetate and Composite Aromatic Polyamide Reverse Osmosis Membranes. *J. Memb. Sci.* **1997**. https://doi.org/10.1016/S0376-7388(96)00351-1.

(107) Mi, B.; Elimelech, M. Organic Fouling of Forward Osmosis Membranes: Fouling Reversibility and Cleaning without Chemical Reagents. *J. Memb. Sci.* **2010**. https://doi.org/10.1016/j.memsci.2009.11.021.

(108) Vrijenhoek, E. M.; Hong, S.; Elimelech, M. Influence of Membrane Surface Properties on Initial Rate of Colloidal Fouling of Reverse Osmosis and Nanofiltration Membranes. *J. Memb. Sci.* **2001**. https://doi.org/10.1016/S0376-7388(01)00376-3.

(109) Zhu, X.; Elimelech, M. Colloidal Fouling of Reverse Osmosis Membranes: Measurements and Fouling Mechanisms. *Environ. Sci. Technol.* **1997**. https://doi.org/10.1021/es970400v.

(110) Asadollahi, M.; Bastani, D.; Musavi, S. A. Enhancement of Surface Properties and Performance of Reverse Osmosis Membranes after Surface Modification: A Review. *Desalination*. 2017. https://doi.org/10.1016/j.desal.2017.05.027.

(111) Kaner, P.; Dudchenko, A. V.; Mauter, M. S.; Asatekin, A. Zwitterionic Copolymer

Additive Architecture Affects Membrane Performance: Fouling Resistance and Surface Rearrangement in Saline Solutions. *J. Mater. Chem. A* **2019**, *7* (9), 4829–4846. https://doi.org/10.1039/C8TA11553B.

(112) Song, L.; Elimelech, M. Theory of Concentration Polarization in Crossflow Filtration. *J. Chem. Soc. Faraday Trans.* **1995**. https://doi.org/10.1039/FT9959103389.

(113) Hoek, E. M. V.; Elimelech, M. Cake-Enhanced Concentration Polarization: A New Fouling Mechanism for Salt-Rejecting Membranes. *Environ. Sci. Technol.* **2003**. https://doi.org/10.1021/es0262636.

(114) Di Bella, G.; Mannina, G.; Viviani, G. An Integrated Model for Physical-Biological Wastewater Organic Removal in a Submerged Membrane Bioreactor: Model Development and Parameter Estimation. *Journal of Membrane Science*. 2008. https://doi.org/10.1016/j.memsci.2008.05.036.

(115) Jhaveri, J. H.; Murthy, Z. V. P. A Comprehensive Review on Anti-Fouling Nanocomposite Membranes for Pressure Driven Membrane Separation Processes. *Desalination*. 2016. https://doi.org/10.1016/j.desal.2015.11.009.

(116) Misdan, N.; Ismail, A. F.; Hilal, N. Recent Advances in the Development of (Bio)Fouling Resistant Thin Film Composite Membranes for Desalination. *Desalination*. 2016. https://doi.org/10.1016/j.desal.2015.06.001.

(117) Sagle, A. C.; Van Wagner, E. M.; Ju, H.; McCloskey, B. D.; Freeman, B. D.; Sharma, M. M. PEG-Coated Reverse Osmosis Membranes: Desalination Properties and Fouling Resistance. *J. Memb. Sci.* **2009**. https://doi.org/10.1016/j.memsci.2009.05.013.

(118) Choi, W.; Choi, J.; Bang, J.; Lee, J. H. Layer-by-Layer Assembly of Graphene Oxide Nanosheets on Polyamide Membranes for Durable Reverse-Osmosis Applications. *ACS Appl. Mater. Interfaces* **2013**. https://doi.org/10.1021/am403790s.

(119) Shafi, H. Z.; Khan, Z.; Yang, R.; Gleason, K. K. Surface Modification of Reverse Osmosis Membranes with Zwitterionic Coating for Improved Resistance to Fouling. *Desalination* **2015**. https://doi.org/10.1016/j.desal.2015.02.009.

(120) Matin, A.; Shafi, H.; Wang, M.; Khan, Z.; Gleason, K.; Rahman, F. Reverse Osmosis Membranes Surface-Modified Using an Initiated Chemical Vapor Deposition Technique Show Resistance to Alginate Fouling under Cross-Flow Conditions: Filtration & Subsequent Characterization. *Desalination* **2016**. https://doi.org/10.1016/j.desal.2015.11.003.

(121) Kang, S.; Asatekin, A.; Mayes, A. M.; Elimelech, M. Protein Antifouling Mechanisms of PAN UF Membranes Incorporating PAN-g-PEO Additive. *J. Memb. Sci.* **2007**. https://doi.org/10.1016/j.memsci.2007.03.012.

(122) Asatekin, A.; Kang, S.; Elimelech, M.; Mayes, A. M. Anti-Fouling Ultrafiltration Membranes Containing Polyacrylonitrile-Graft-Poly(Ethylene Oxide) Comb Copolymer

Additives. *J. Memb. Sci.* **2007**. https://doi.org/10.1016/j.memsci.2007.04.011.

(123) Chowdhury, M. R.; Steffes, J.; Huey, B. D.; McCutcheon, J. R. 3D Printed Polyamide Membranes for Desalination. *Science (80-.).* **2018**. https://doi.org/10.1126/science.aar2122.

(124) Koo, J.; Lee, J. H.; Jung, Y. D.; Hong, S. P.; Yoon, S. R. Chlorine Resistant Membrane and The Mechanism of Membrane Degradation by Chlorine. *Proc. Water Environ. Fed.* **2012**. https://doi.org/10.2175/193864708788734205.

(125) Barassi, G.; Borrmann, T. N-Chlorination and Orton Rearrangement of Aromatic Polyamides, Revisited. *J. Membr. Sci. Technol.* **2012**. https://doi.org/10.4172/2155-9589.1000115.

(126) Andrzejewski, P.; Kasprzyk-Hordern, B.; Nawrocki, J. The Hazard of N-Nitrosodimethylamine (NDMA) Formation during Water Disinfection with Strong Oxidants. *Desalination* **2005**. https://doi.org/10.1016/j.desal.2004.11.009.

(127) Huang, H.; Lin, S.; Zhang, L.; Hou, L. Chlorine-Resistant Polyamide Reverse Osmosis Membrane with Monitorable and Regenerative Sacrificial Layers. *ACS Appl. Mater. Interfaces* **2017**. https://doi.org/10.1021/acsami.6b16462.

(128) Cadotte, J. E.; Petersen, R. J.; Larson, R. E.; Erickson, E. E. A New Thin-Film Composite Seawater Reverse Osmosis Membrane. *Desalination* **1980**. https://doi.org/10.1016/S0011-9164(00)86003-8.

(129) Cho, K. L.; Hill, A. J.; Caruso, F.; Kentish, S. E. Chlorine Resistant Glutaraldehyde Crosslinked Polyelectrolyte Multilayer Membranes for Desalination. *Adv. Mater.* **2015**. https://doi.org/10.1002/adma.201405783.

(130) Kim, S. G.; Hyeon, D. H.; Chun, J. H.; Chun, B. H.; Kim, S. H. Novel Thin Nanocomposite RO Membranes for Chlorine Resistance. *Desalin. Water Treat.* **2013**. https://doi.org/10.1080/19443994.2013.780994.

(131) Zhang, Y.; Zhao, C.; Yan, H.; Pan, G.; Guo, M.; Na, H.; Liu, Y. Highly Chlorine-Resistant Multilayer Reverse Osmosis Membranes Based on Sulfonated Poly(Arylene Ether Sulfone) and Poly(Vinyl Alcohol). *Desalination* **2014**. https://doi.org/10.1016/j.desal.2013.12.034.

(132) Kim, S. G.; Park, S. Y.; Chun, J. H.; Chun, B. H.; Kim, S. H. Novel Thin-Film Composite Membrane for Seawater Desalination with Sulfonated Poly(Arylene Ether Sulfone) Containing Amino Groups. *Desalin. Water Treat.* **2012**. https://doi.org/10.1080/19443994.2012.672177.

(133) Zhao, Y.; Dai, L.; Zhang, Q.; Zhou, S.; Zhang, S. Chlorine-Resistant Sulfochlorinated and Sulfonated Polysulfone for Reverse Osmosis Membranes by Coating Method. *J. Colloid Interface Sci.* **2019**. https://doi.org/10.1016/j.jcis.2019.01.104.

(134) Yum, I.; Jeong, D.; Oh, J.; Lee, Y. A Novel Sulfonated Poly(Arylene Ether Ketone) Reverse Osmosis Membrane: Effect of Casting Condition on Separation Characteristics. *Desalin. Water Treat.* **2010**. https://doi.org/10.5004/dwt.2010.1719.

(135) Xia, Y.; Gao, C.; Lu, X. Preliminary Study on Sulfonated Polyether Sulfone Membranes. *Shuichuli Jishu* **1993**.

(136) Liu, M.; Chen, Z.; Yu, S.; Wu, D.; Gao, C. Thin-Film Composite Polyamide Reverse Osmosis Membranes with Improved Acid Stability and Chlorine Resistance by Coating N-Isopropylacrylamide-Co-Acrylamide Copolymers. *Desalination* **2011**. https://doi.org/10.1016/j.desal.2010.11.052.

(137) Liu, M.; Chen, Q.; Wang, L.; Yu, S.; Gao, C. Improving Fouling Resistance and Chlorine Stability of Aromatic Polyamide Thin-Film Composite RO Membrane by Surface Grafting of Polyvinyl Alcohol (PVA). *Desalination* **2015**. https://doi.org/10.1016/j.desal.2015.03.028.

(138) Zhang, Y.; Zhao, C.; Yan, H.; Pan, G.; Guo, M.; Na, H.; Liu, Y. Highly Chlorine-Resistant Multilayer Reverse Osmosis Membranes Based on Sulfonated Poly(Arylene Ether Sulfone) and Poly(Vinyl Alcohol) for Water Desalination [Erratum to Document Cited in CA160:376052]. *Desalination* **2014**.

(139) Kim, S. G.; Park, K. T.; Chun, B.-H.; Bang, J.; Kim, S. H. Sulfonated Poly(Arylene Ether Sulfone) RO Membranes for High Water Flux and Chlorine Resistance. *Desalin. Water Treat.* **2010**. https://doi.org/10.5004/dwt.2010.1687.

(140) Liu, C.; Lee, J.; Ma, J.; Elimelech, M. Antifouling Thin-Film Composite Membranes by Controlled Architecture of Zwitterionic Polymer Brush Layer. *Environ. Sci. Technol.* **2017**, *51* (4), 2161–2169. https://doi.org/10.1021/acs.est.6b05992.

(141) Bengani-Lutz, P.; Converse, E.; Cebe, P.; Asatekin, A. Self-Assembling Zwitterionic Copolymers as Membrane Selective Layers with Excellent Fouling Resistance: Effect of Zwitterion Chemistry. *ACS Appl. Mater. Interfaces* **2017**, *9* (24), 20859–20872. https://doi.org/10.1021/acsami.7b04884.

(142) Zhao, Y. F.; Zhang, P. Bin; Sun, J.; Liu, C. J.; Zhu, L. P.; Xu, Y. Y. Electrolyte-Responsive Polyethersulfone Membranes with Zwitterionic Polyethersulfone-Based Copolymers as Additive. *J. Memb. Sci.* **2016**, *510*, 306–313. https://doi.org/10.1016/j.memsci.2016.03.006.

(143) Surawanvijit, S.; Rahardianto, A.; Cohen, Y. An Integrated Approach for Characterization of Polyamide Reverse Osmosis Membrane Degradation Due to Exposure to Free Chlorine. *J. Memb. Sci.* **2016**, *510*, 164–173. https://doi.org/10.1016/j.memsci.2016.02.044.

(144) McCutcheon, J. R.; Elimelech, M. Influence of Membrane Support Layer Hydrophobicity on Water Flux in Osmotically Driven Membrane Processes. *J. Memb. Sci.* **2008**, *318* (1–2), 458–466. https://doi.org/10.1016/j.memsci.2008.03.021.

(145) Xu, J.; Boyer, C. Visible Light Photocatalytic Thiol-Ene Reaction: An Elegant Approach for Fast Polymer Postfunctionalization and Step-Growth Polymerization. *Macromolecules* **2015**, *48* (3), 520–529. https://doi.org/10.1021/ma502460t.

(146) Chede, S.; Anaya, N. M.; Oyanedel-Craver, V.; Gorgannejad, S.; Harris, T. A. L.; Al-Mallahi, J.; Abu-Dalo, M.; Qdais, H. A.; Escobar, I. C. Desalination Using Low Biofouling Nanocomposite Membranes: From Batch-Scale to Continuous-Scale Membrane Fabrication. *Desalination* **2017**, No. May, 1–11. https://doi.org/10.1016/j.desal.2017.05.007.

(147) Li, J. H.; Li, M. Z.; Miao, J.; Wang, J. Bin; Shao, X. S.; Zhang, Q. Q. Improved Surface Property of PVDF Membrane with Amphiphilic Zwitterionic Copolymer as Membrane Additive. *Appl. Surf. Sci.* **2012**, *258* (17), 6398–6405. https://doi.org/10.1016/j.apsusc.2012.03.049.

(148) Zhang, Q.; Zhang, S.; Dai, L.; Chen, X. Novel Zwitterionic Poly(Arylene Ether Sulfone)s as Antifouling Membrane Material. *J. Memb. Sci.* **2010**, *349* (1–2), 217–224. https://doi.org/10.1016/j.memsci.2009.11.048.

(149) Ismail, A. F.; Hassan, A. R. Effect of Additive Contents on the Performances and Structural Properties of Asymmetric Polyethersulfone (PES) Nanofiltration Membranes. *Sep. Purif. Technol.* **2007**, *55* (1), 98–109. https://doi.org/10.1016/j.seppur.2006.11.002.

(150) Harris, D. c. *Quantitative Chemical Analysis*; 2007; Vol. 42. https://doi.org/10.1016/j.micron.2011.01.004.

(151) Yi, Z.; Zhu, L. P.; Xu, Y. Y.; Zhao, Y. F.; Ma, X. T.; Zhu, B. K. Polysulfone-Based Amphiphilic Polymer for Hydrophilicity and Fouling-Resistant Modification of Polyethersulfone Membranes. *J. Memb. Sci.* **2010**, *365* (1–2), 25–33. https://doi.org/10.1016/j.memsci.2010.08.001.

(152) Liu, S.; Liu, W.; Liu, Y.; Lin, J. H.; Zhou, X.; Janik, M. J.; Colby, R. H.; Zhang, Q. Influence of Imidazolium-Based Ionic Liquids on the Performance of Ionic Polymer Conductor Network Composite Actuators. *Polym. Int.* **2010**, *59* (3), 321–328. https://doi.org/10.1002/pi.2771.

(153) Schreiner, C.; Bridge, A. T.; Hunley, M. T.; Long, T. E.; Green, M. D. Segmented Imidazolium Ionenes: Solution Rheology, Thermomechanical Properties, and Electrospinning. *Polym. (United Kingdom)* **2017**, *114*, 257–265. https://doi.org/10.1016/j.polymer.2017.03.003.

(154) Tang, C. Y.; Kwon, Y. N.; Leckie, J. O. Effect of Membrane Chemistry and Coating Layer on Physiochemical Properties of Thin Film Composite Polyamide RO and NF Membranes. II. Membrane Physiochemical Properties and Their Dependence on Polyamide and Coating Layers. *Desalination* **2009**, *242* (1–3), 168–182. https://doi.org/10.1016/j.desal.2008.04.004.

(155) Cheng, G.; Zhang, Z.; Chen, S.; Bryers, J. D.; Jiang, S. Inhibition of Bacterial Adhesion

and Biofilm Formation on Zwitterionic Surfaces. *Biomaterials* **2007**, *28* (29), 4192–4199. https://doi.org/10.1016/j.biomaterials.2007.05.041.

(156) Geise, G. M.; Park, H. B.; Sagle, A. C.; Freeman, B. D.; McGrath, J. E. Water Permeability and Water/Salt Selectivity Tradeoff in Polymers for Desalination. *J. Memb. Sci.* **2011**, *369* (1–2), 130–138. https://doi.org/10.1016/j.memsci.2010.11.054.

(157) Cohen-Tanugi, D.; McGovern, R. K.; Dave, S. H.; Lienhard, J. H.; Grossman, J. C. Quantifying the Potential of Ultra-Permeable Membranes for Water Desalination. *Energy Environ. Sci.* **2014**, *7* (3), 1134–1141. https://doi.org/10.1039/C3EE43221A.

(158) Deshmukh, A.; Yip, N. Y.; Lin, S.; Elimelech, M. Desalination by Forward Osmosis: Identifying Performance Limiting Parameters through Module-Scale Modeling. *J. Memb. Sci.* **2015**, *491*, 159–167. https://doi.org/10.1016/j.memsci.2015.03.080.

(159) Callow, J. A.; Callow, M. E. Trends in the Development of Environmentally Friendly Fouling-Resistant Marine Coatings. *Nat. Commun.* **2011**, *2*, 244. https://doi.org/10.1038/ncomms1251.

(160) Yue, W. W.; Li, H. J.; Xiang, T.; Qin, H.; Sun, S. D.; Zhao, C. S. Grafting of Zwitterion from Polysulfone Membrane via Surface-Initiated ATRP with Enhanced Antifouling Property and Biocompatibility. *J. Memb. Sci.* **2013**, *446*, 79–91. https://doi.org/10.1016/j.memsci.2013.06.029.

(161) Escobar, I. C.; Van Der Bruggen, B. Microfiltration and Ultrafiltration Membrane Science and Technology. *J. Appl. Polym. Sci.* **2015**, *132* (21). https://doi.org/10.1002/app.42002.

(162) Li, Q.; Imbrogno, J.; Belfort, G.; Wang, X. L. Making Polymeric Membranes Antifouling via "Grafting from" Polymerization of Zwitterions. *J. Appl. Polym. Sci.* **2015**, *132* (21). https://doi.org/10.1002/app.41781.

(163) Sae-Ung, P.; Kolewe, K. W.; Bai, Y.; Rice, E. W.; Schiffman, J. D.; Emrick, T.; Hoven, V. P. Antifouling Stripes Prepared from Clickable Zwitterionic Copolymers. *Langmuir* **2017**, *33* (28), 7028–7035. https://doi.org/10.1021/acs.langmuir.7b01431.

(164) Shaikh, A. A. G.; Hay, A. S. Synthesis and Characterization of Soluble, Fluorescent Poly(Arylene Ether)s, Poly(Arylene Thioether)s, and Poly(Arylene Sulfone)s Containing 1,3,5-Triphenylbenzene Segments. *J. Polym. Sci. Part A Polym. Chem.* **2002**, *40* (4), 496–510. https://doi.org/10.1002/pola.10136.

(165) Lu, J.; Miyatake, K.; Hlil, A. R.; Hay, A. S. Novel Soluble and Fluorescent Poly(Arylene Ether)s Containing p-Quaterphenyl, 2,5-Bis(4-Phenylphenyl)Oxadiazole, or 2,5-Bis(4-Phenylphenyl)Triazole Groups. *Macromolecules* **2001**, *34* (17), 5860–5867. https://doi.org/10.1021/ma0103977.

(166) Park, J.; Kim, J.; Seo, M.; Lee, J.; Kim, S. Y. Dual-Mode Fluorescence Switching Induced by Self-Assembly of Well-Defined Poly(Arylene Ether Sulfone)s Containing Pyrene and Amide Moieties. *Chem. Commun.* **2012**, *48* (85), 10556.

https://doi.org/10.1039/c2cc35804b.

(167) Yang, Y. F.; Li, Y.; Li, Q. L.; Wan, L. S.; Xu, Z. K. Surface Hydrophilization of Microporous Polypropylene Membrane by Grafting Zwitterionic Polymer for Anti-Biofouling. *J. Memb. Sci.* **2010**, *362* (1–2), 255–264. https://doi.org/10.1016/j.memsci.2010.06.048.

(168) Chiang, Y. C.; Chang, Y.; Chuang, C. J.; Ruaan, R. C. A Facile Zwitterionization in the Interfacial Modification of Low Bio-Fouling Nanofiltration Membranes. *J. Memb. Sci.* **2012**, *389*, 76–82. https://doi.org/10.1016/j.memsci.2011.10.017.

(169) Lee, K. P.; Arnot, T. C.; Mattia, D. A Review of Reverse Osmosis Membrane Materials for Desalination-Development to Date and Future Potential. *J. Memb. Sci.* **2011**, *370* (1–2), 1–22. https://doi.org/10.1016/j.memsci.2010.12.036.

(170) Misdan, N.; Lau, W. J.; Ismail, A. F. Seawater Reverse Osmosis (SWRO) Desalination by Thin-Film Composite Membrane-Current Development, Challenges and Future Prospects. *Desalination* **2012**, *287*, 228–237. https://doi.org/10.1016/j.desal.2011.11.001.

(171) Ross, S. D. Nucleophilic Aromatic Substitution Reactions. In *Progress in Physical Organic Chemistry*; 2007; Vol. 1, pp 31–74. https://doi.org/10.1002/9780470171806.ch2.

(172) Ross, S. D. Catalysis of Intermediate Formation in Nucleophilic Aromatic Substitution. *Tetrahedron* **1969**, *25* (18), 4427–4436. https://doi.org/10.1016/S0040-4020(01)82984-7.

(173) Ross, S. D.; Finkelstein, M.; Petersen, R. C. Nucleophilic Displacement Reactions in Aromatic Systems. V. The Mechanism of the Reaction of 2,4-Dinitrochlorobenzene with Primary Amines in Chloroform. *J. Am. Chem. Soc.* **1959**, *81* (20), 5336–5342. https://doi.org/10.1021/ja01529a024.

(174) Jones, G. O.; Al Somaa, A.; O'Brien, J. M.; Albishi, H.; Al-Megren, H. A.; Alabdulrahman, A. M.; Alsewailem, F. D.; Hedrick, J. L.; Rice, J. E.; Horn, H. W. Computational Investigations on Base-Catalyzed Diaryl Ether Formation. *J. Org. Chem.* **2013**. https://doi.org/10.1021/jo400550c.

(175) Severnyi, V. V.; Minsker, Y. I.; Ovechkina, N. A. Processes Occurring in Organosilicon Compositions Undergoing Vulcanization by Atmospheric Moisture. *Polym. Sci. U.S.S.R.* **1977**, *19* (1), 42–49. https://doi.org/10.1016/0032-3950(77)90146-0.

(176) Nomura, N.; Tsurugi, K.; RajanBabu, T. V.; Kondo, T. Homogeneous Two-Component Polycondensation without Strict Stoichiometric Balance via the Tsuji-Trost Reaction: Remote Control of Two Reaction Sites by Catalysis. *J. Am. Chem. Soc.* **2004**, *126* (17), 5354–5355. https://doi.org/10.1021/ja0492743.

(177) Dove, A. P.; Meier, M. A. R. Step-Growth Polymerization in the 21st Century. *Macromolecular Chemistry and Physics*. 2014, pp 2135–2137. https://doi.org/10.1002/macp.201400512.

(178) Viswanathan, R.; Johnson, B. C.; McGrath, J. E. Synthesis, Kinetic Observations and Characteristics of Polyarylene Ether Sulphones Prepared via a Potassium Carbonate DMAC Process. *Polymer (Guildf).* **1984**. https://doi.org/10.1016/0032-3861(84)90258-1.

(179) Plenio, H. The Coordination Chemistry of the CF Unit in Fluorocarbons. *Chem. Rev.* **1997**, *97* (8), 3363–3384. https://doi.org/10.1021/cr970465g.

(180) Costello, C. A.; McCarthy, T. J. Surface-Selective Introduction of Specific Functionalities onto Poly (Tetrafluoroethylene. *Macromolecules* **1987**, *20* (11), 2819–2828. https://doi.org/10.1021/ma00177a030.

(181) Bergeron, M.; Johnson, T.; Paquin, J. F. The Use of Fluoride as a Leaving Group: S N2′ Displacement of a C-F Bond on 3,3-Difluoropropenes with Organolithium Reagents to Give Direct Access to Monofluoroalkenes. *Angew. Chemie - Int. Ed.* **2011**, *50* (47), 11112–11116. https://doi.org/10.1002/anie.201105138.

(182) Odian, G. *Principles of Polymerization, 4th Edition*; 2004. https://doi.org/10.1016/B978-1-85617-803-7.50022-5.

(183) Choi, U. H.; Liang, S.; O'Reilly, M. V.; Winey, K. I.; Runt, J.; Colby, R. H. Influence of Solvating Plasticizer on Ion Conduction of Polysiloxane Single-Ion Conductors. *Macromolecules* **2014**. https://doi.org/10.1021/ma500146v.

(184) Robeson, L. M.; Smith, Z. P.; Freeman, B. D.; Paul, D. R. Contributions of Diffusion and Solubility Selectivity to the Upper Bound Analysis for Glassy Gas Separation Membranes. *J. Memb. Sci.* **2014**. https://doi.org/10.1016/j.memsci.2013.10.066.

(185) Merkel, T. C.; Freeman, B. D.; Spontak, R. J.; He, Z.; Pinnau, I.; Meakin, P.; Hill, A. J. Ultrapermeable, Reverse-Selective Nanocomposite Membranes. *Science (80-.).* **2002**. https://doi.org/10.1126/science.1069580.

(186) Zhang, H.; Geise, G. M. Modeling the Water Permeability and Water/Salt Selectivity Tradeoff in Polymer Membranes. *J. Memb. Sci.* **2016**. https://doi.org/10.1016/j.memsci.2016.08.035.

(187) Merkel, T. C.; Freeman, B. D.; Spontak, R. J.; He, Z.; Pinnau, I.; Meakin, P.; Hill, A. J. Sorption, Transport, and Structural Evidence for Enhanced Free Volume in Poly(4-Methyl-2-Pentyne)/Fumed Silica Nanocomposite Membranes. *Chem. Mater.* **2003**. https://doi.org/10.1021/cm020672j.

(188) Lee, C. H.; Vanhouten, D.; Lane, O.; McGrath, J. E.; Hou, J.; Madsen, L. A.; Spano, J.; Wi, S.; Cook, J.; Xie, W.; et al. Disulfonated Poly(Arylene Ether Sulfone) Random Copolymer Blends Tuned for Rapid Water Permeation via Cation Complexation with Poly(Ethylene Glycol) Oligomers. *Chem. Mater.* **2011**. https://doi.org/10.1021/cm1032173.

(189) Luo, H.; Aboki, J.; Ji, Y.; Guo, R.; Geise, G. M. Water and Salt Transport Properties of Triptycene-Containing Sulfonated Polysulfone Materials for Desalination Membrane

Applications. *ACS Appl. Mater. Interfaces* **2018**. https://doi.org/10.1021/acsami.7b17225.

(190) Kamcev, J.; Doherty, C. M.; Lopez, K. P.; Hill, A. J.; Paul, D. R.; Freeman, B. D. Effect of Fixed Charge Group Concentration on Salt Permeability and Diffusion Coefficients in Ion Exchange Membranes. *J. Memb. Sci.* **2018**. https://doi.org/10.1016/j.memsci.2018.08.053.

(191) Wang, X. Y.; Hill, A. J.; Freeman, B. D.; Sanchez, I. C. Structural, Sorption and Transport Characteristics of an Ultrapermeable Polymer. *J. Memb. Sci.* **2008**. https://doi.org/10.1016/j.memsci.2007.12.074.

(192) Mafi, A.; Raisi, A.; Hatam, M.; Aroujalian, A. A Mass Transfer Model for Pure Alcoholic Permeation through the PDMS Membrane. *Desalin. Water Treat.* **2014**. https://doi.org/10.1080/19443994.2013.836996.

(193) Marcus, Y.; Hefter, G. Ion Pairing. *Chem. Rev.* **2006**. https://doi.org/10.1021/cr040087x.

(194) Roda, A.; Hofmann, A. F.; Mysels, K. J. The Influence of Bile Salt Structure on Self-Association in Aqueous Solutions. *J. Biol. Chem.* **1983**.

(195) Davis, H. E.; Rosinski, M.; Morgan, J. R.; Yarmush, M. L. Charged Polymers Modulate Retrovirus Transduction via Membrane Charge Neutralization and Virus Aggregation. *Biophys. J.* **2004**. https://doi.org/10.1016/S0006-3495(04)74197-1.

(196) Golodnitsky, D.; Strauss, E.; Peled, E.; Greenbaum, S. Review—On Order and Disorder in Polymer Electrolytes. *J. Electrochem. Soc.* **2015**. https://doi.org/10.1149/2.0161514jes.

(197) Rehm, T. H.; Gröhn, F.; Schmuck, C. Self-Assembly of a Triple-Zwitterion in Polar Solutions: Hierarchical Formation of Nanostructures. *Soft Matter* **2012**. https://doi.org/10.1039/c2sm07153c.

(198) Matsumoto, T.; Ichikawa, T.; Ohno, H. Design of Ionic Liquid-Based Polyelectrolytes by Combining “nanostructurisation” and “Zwitterionisation.” *Polym. Chem.* **2016**. https://doi.org/10.1039/c5py01838b.

(199) Kim, S.; Kim, H.; Choi, J. H.; Cho, M. Ion Aggregation in High Salt Solutions: Ion Network versus Ion Cluster. *J. Chem. Phys.* **2014**. https://doi.org/10.1063/1.4896227.

(200) Iskrenova-Tchoukova, E.; Kalinichev, A. G.; Kirkpatrick, R. J. Metal Cation Complexation with Natural Organic Matter in Aqueous Solutions: Molecular Dynamics Simulations and Potentials of Mean Force. *Langmuir* **2010**. https://doi.org/10.1021/la102535n.

(201) Young, L. M.; Saunders, J. C.; Mahood, R. A.; Revill, C. H.; Foster, R. J.; Tu, L. H.; Raleigh, D. P.; Radford, S. E.; Ashcroft, A. E. Screening and Classifying Small-Molecule Inhibitors of Amyloid Formation Using Ion Mobility Spectrometry-Mass Spectrometry. *Nat. Chem.* **2015**. https://doi.org/10.1038/nchem.2129.

(202) Hoarfrost, M. L.; Tyagi, M. S.; Segalman, R. A.; Reimer, J. A. Effect of Confinement on Proton Transport Mechanisms in Block Copolymer/Ionic Liquid Membranes. *Macromolecules* **2012**. https://doi.org/10.1021/ma202741g.

(203) Noriega, R.; Rivnay, J.; Vandewal, K.; Koch, F. P. V; Stingelin, N.; Smith, P.; Toney, M. F.; Salleo, A. A General Relationship between Disorder, Aggregation and Charge Transport in Conjugated Polymers. *Nat. Mater.* **2013**. https://doi.org/10.1038/nmat3722.

(204) Goodenough, J. B.; Park, K. S. The Li-Ion Rechargeable Battery: A Perspective. *Journal of the American Chemical Society*. 2013. https://doi.org/10.1021/ja3091438.

(205) Li, D.; Yan, Y.; Wang, H. Recent Advances in Polymer and Polymer Composite Membranes for Reverse and Forward Osmosis Processes. *Progress in Polymer Science*. 2016. https://doi.org/10.1016/j.progpolymsci.2016.03.003.

(206) Li, D.; Wang, H. Recent Developments in Reverse Osmosis Desalination Membranes. *J. Mater. Chem.* **2010**. https://doi.org/10.1039/b924553g.

(207) Bolto, B.; Tran, T.; Hoang, M.; Xie, Z. Crosslinked Poly(Vinyl Alcohol) Membranes. *Progress in Polymer Science (Oxford)*. 2009. https://doi.org/10.1016/j.progpolymsci.2009.05.003.

(208) Lufrano, F.; Baglio, V.; Staiti, P.; Arico', A. S.; Antonucci, V. Development and Characterization of Sulfonated Polysulfone Membranes for Direct Methanol Fuel Cells. *Desalination* **2006**. https://doi.org/10.1016/j.desal.2006.03.069.

(209) Padaki, M.; Isloor, A. M.; Wanichapichart, P.; Ismail, A. F. Preparation and Characterization of Sulfonated Polysulfone and N-Phthloyl Chitosan Blend Composite Cation-Exchange Membrane for Desalination. *Desalination* **2012**. https://doi.org/10.1016/j.desal.2012.04.025.

(210) Joseph, D.; Krishnan, N. N.; Henkensmeier, D.; Jang, J. H.; Choi, S. H.; Kim, H. J.; Han, J.; Nam, S. W. Thermal Crosslinking of PBI/Sulfonated Polysulfone Based Blend Membranes. *J. Mater. Chem. A* **2017**. https://doi.org/10.1039/c6ta07653j.

(211) Arens, L.; Albrecht, J. B.; Höpfner, J.; Schlag, K.; Habicht, A.; Seiffert, S.; Wilhelm, M. Energy Consumption for the Desalination of Salt Water Using Polyelectrolyte Hydrogels as the Separation Agent. *Macromol. Chem. Phys.* **2017**, *218* (24). https://doi.org/10.1002/macp.201700237.

(212) Al-Karaghouli, A.; Kazmerski, L. L. Energy Consumption and Water Production Cost of Conventional and Renewable-Energy-Powered Desalination Processes. *Renewable and Sustainable Energy Reviews*. 2013. https://doi.org/10.1016/j.rser.2012.12.064.

(213) Avlonitis, S. A.; Kouroumbas, K.; Vlachakis, N. Energy Consumption and Membrane Replacement Cost for Seawater RO Desalination Plants. *Desalination* **2003**. https://doi.org/10.1016/S0011-9164(03)00395-3.

(214) Bódalo-Santoyo, A.; Gómez-Carrasco, J. L.; Gómez-Gómez, E.; Máximo-Martín, M. F.; Hidalgo-Montesinos, A. M. Spiral-Wound Membrane Reverse Osmosis and the Treatment of Industrial Effluents. *Desalination* **2004**, *160* (2), 151–158. https://doi.org/10.1016/S0011-9164(04)90005-7.

(215) Al-Obaidi, M. A.; Mujtaba, I. M. Steady State and Dynamic Modeling of Spiral Wound Wastewater Reverse Osmosis Process. *Comput. Chem. Eng.* **2016**, *90*, 278–299. https://doi.org/10.1016/j.compchemeng.2016.04.001.

(216) Fritzmann, C.; Löwenberg, J.; Wintgens, T.; Melin, T. State-of-the-Art of Reverse Osmosis Desalination. *Desalination* **2007**, *216* (1–3), 1–76. https://doi.org/10.1016/j.desal.2006.12.009.

(217) Kumano, A. Advances in Hollow-Fiber Reverse-Osmosis Membrane Modules in Seawater Desalination. In *Advances in Water Desalination*; 2012; pp 309–375. https://doi.org/10.1002/9781118347737.ch4.

(218) Baker, R. W. *Membrane Technology and Applications*; 2004. https://doi.org/10.1002/0470020393.

APPENDIX REFERENCES

1. Hamid, Z. A. A.; Lim, K. W., Evaluation of UV-crosslinked poly (ethylene glycol) diacrylate/poly (dimethylsiloxane) dimethacrylate hydrogel: properties for tissue engineering application. *Procedia Chemistry* **2016,** *19*, 410-418.

2. Crosby, A. J.; Lee, J. Y., Polymer nanocomposites: the "nano" effect on mechanical properties. *Polymer reviews* **2007,** *47* (2), 217-229.

3. Ganesan, V.; Jayaraman, A., Theory and simulation studies of effective interactions, phase behavior and morphology in polymer nanocomposites. *Soft Matter* **2014,** *10* (1), 13-38.

4. Hall, L. M.; Jayaraman, A.; Schweizer, K. S., Molecular theories of polymer nanocomposites. *Current Opinion in Solid State and Materials Science* **2010,** *14* (2), 38-48.

5. Hore, M. J. A.; Composto, R. J., Functional Polymer Nanocomposites Enhanced by Nanorods. *Macromolecules* **2014,** *47* (3), 875-887.

6. Kumar, P.; Sandeep, K. P.; Alavi, S.; Truong, V. D., A Review of Experimental and Modeling Techniques to Determine Properties of Biopolymer-Based Nanocomposites. *Journal of Food Science* **2011,** *76* (1), E2-E14.

7. Moniruzzaman, M.; Winey, K. I., Polymer Nanocomposites Containing Carbon Nanotubes. *Macromolecules* **2006,** *39* (16), 5194-5205.

8. Kumar, S. K.; Benicewicz, B. C.; Vaia, R. A.; Winey, K. I., 50th anniversary perspective: are polymer nanocomposites practical for applications? *Macromolecules* **2017,** *50* (3), 714-731.

9. Englebienne, P.; Van Hoonacker, A., Gold–conductive polymer nanoparticles: A hybrid material with enhanced photonic reactivity to environmental stimuli. *Journal of Colloid and Interface Science* **2005,** *292* (2), 445-454.

10. Oh, Y.; Chun, K.-Y.; Lee, E.; Kim, Y.-J.; Baik, S., Functionalized nano-silver particles assembled on one-dimensional nanotube scaffolds for ultra-highly conductive silver/polymer composites. *Journal of Materials Chemistry* **2010,** *20* (18), 3579-3582.

11. Turhan, Y.; Dogan, M.; Alkan, M., Poly (vinyl chloride)/kaolinite nanocomposites: characterization and thermal and optical properties. *Industrial & Engineering Chemistry Research* **2010,** *49* (4), 1503-1513.

12. Huang, X.-J.; Zeng, X.-F.; Wang, J.-X.; Chen, J.-F., Transparent dispersions of monodispersed ZnO nanoparticles with ultrahigh content and stability for polymer nanocomposite film with excellent optical properties. *Industrial & Engineering Chemistry Research* **2018,** *57* (12), 4253-4260.

13. Amancio, S. T.; dos Santos, J. F., Joining of Polymers and Polymer-Metal Hybrid Structures: Recent Developments and Trends. *Polymer Engineering and Science* **2009,** *49* (8), 1461-1476.

14. Giannelis, E. P., Polymer layered silicate nanocomposites. *Advanced materials* **1996,** *8* (1), 29-35.

15. Paul, D. R.; Robeson, L. M., Polymer nanotechnology: nanocomposites. *Polymer* **2008,** *49* (15), 3187-3204.

16. Zhang, H.; Wang, L.; Song, L.; Niu, G.; Cao, H.; Wang, G.; Yang, H.; Zhu, S., Controllable properties and microstructure of hydrogels based on crosslinked poly (ethylene glycol) diacrylates with different molecular weights. *Journal of Applied Polymer Science* **2011,** *121* (1), 531-540.

17. Browning, M. B.; Cereceres, S. N.; Luong, P. T.; Cosgriff-Hernandez, E. M., Determination of the in vivo degradation mechanism of PEGDA hydrogels. *Journal of Biomedical Materials Research Part A* **2014,** *102* (12), 4244-4251.

18. Bertrand, O.; Gohy, J.-F., Photo-responsive polymers: synthesis and applications. *Polymer Chemistry* **2017,** *8* (1), 52-73.

19. Bencherif, S. A.; Srinivasan, A.; Sheehan, J. A.; Walker, L. M.; Gayathri, C.; Gil, R.; Hollinger, J. O.; Matyjaszewski, K.; Washburn, N. R., End-group effects on the properties of PEG-co-PGA hydrogels. *Acta biomaterialia* **2009,** *5* (6), 1872-1883.

20. Nguyen, Q. T.; Hwang, Y.; Chen, A. C.; Varghese, S.; Sah, R. L., Cartilage-like mechanical properties of poly (ethylene glycol)-diacrylate hydrogels. *Biomaterials* **2012,** *33* (28), 6682-6690.

21. Ficek, B. A.; Thiesen, A. M.; Scranton, A. B., Cationic photopolymerizations of thick polymer systems: Active center lifetime and mobility. *European polymer journal* **2008,** *44* (1), 98-105.

22. Anseth, K. S.; Kline, L. M.; Walker, T. A.; Anderson, K. J.; Bowman, C. N., Reaction kinetics and volume relaxation during polymerizations of multiethylene glycol dimethacrylates. *Macromolecules* **1995,** *28* (7), 2491-2499.

23. Estridge, C. E.; Jayaraman, A., Effect of homopolymer matrix on diblock copolymer grafted nanoparticle conformation and potential of mean force: A molecular simulation study. *Journal of Polymer Science Part B: Polymer Physics* **2015,** *53* (1), 76-88.

24. Jayaraman, A.; Schweizer, K. S., Effect of the number and placement of polymer tethers on the structure of concentrated solutions and melts of hybrid nanoparticles. *Langmuir* **2008,** *24* (19), 11119-11130.

25. Jayaraman, A.; Schweizer, K. S., Effective interactions and self-assembly of hybrid polymer grafted nanoparticles in a homopolymer matrix. *Macromolecules* **2009,** *42* (21), 8423-8434.

26. Martin, T. B.; Jayaraman, A., Identifying the Ideal Characteristics of the Grafted Polymer Chain Length Distribution for Maximizing Dispersion of Polymer Grafted Nanoparticles in a Polymer Matrix. *Macromolecules* **2013,** *46* (22), 9144-9150.

27. Nair, N.; Jayaraman, A., Self-Consistent PRISM Theory−Monte Carlo Simulation Studies of Copolymer Grafted Nanoparticles in a Homopolymer Matrix. *Macromolecules* **2010,** *43* (19), 8251-8263.

28. Gaharwar, A. K.; Peppas, N. A.; Khademhosseini, A., Nanocomposite hydrogels for biomedical applications. *Biotechnology and bioengineering* **2014,** *111* (3), 441-453.

29. Zhan, Y.; Pan, Y.; Chen, B.; Lu, J.; Zhong, Z.; Niu, X., Strain rate dependent hyperelastic stress-stretch behavior of a silica nanoparticle reinforced poly (ethylene glycol) diacrylate nanocomposite hydrogel. *Journal of the mechanical behavior of biomedical materials* **2017,** *75*, 236-243.

30. Wang, M.; Dheressa, E.; Brown Kristen, A.; Green Matthew, D., Effect of Crosslinker Length and Architecture on the Thermomechanical Properties of CNT-Loaded Elastomeric Polymer Matrix Composites. *Macromolecular Rapid Communications* **2018,** *0* (0), 1800091.

31. Bae, M.; Gemeinhart, R. A.; Divan, R.; Suthar, K. J.; Mancini, D. C., Fabrication of poly (ethylene glycol) hydrogel structures for pharmaceutical applications using electron beam and optical lithography. *Journal of Vacuum Science & Technology B, Nanotechnology and Microelectronics: Materials, Processing, Measurement, and Phenomena* **2010,** *28* (6), C6P24-C6P29.

32. Janusziewicz, R.; Tumbleston, J. R.; Quintanilla, A. L.; Mecham, S. J.; DeSimone, J. M., Layerless fabrication with continuous liquid interface production. *Proceedings of the National Academy of Sciences* **2016,** *113* (42), 11703-11708.

33. Johnson, A. R.; Caudill, C. L.; Tumbleston, J. R.; Bloomquist, C. J.; Moga, K. A.; Ermoshkin, A.; Shirvanyants, D.; Mecham, S. J.; Luft, J. C.; DeSimone, J. M., Single-step fabrication of computationally designed microneedles by continuous liquid interface production. *PLoS One* **2016,** *11* (9), e0162518.

34. Tumbleston, J. R.; Shirvanyants, D.; Ermoshkin, N.; Janusziewicz, R.; Johnson, A. R.; Kelly, D.; Chen, K.; Pinschmidt, R.; Rolland, J. P.; Ermoshkin, A.; Samulski, E. T.;

DeSimone, J. M., Continuous liquid interface production of 3D objects. *Science* **2015,** *347* (6228), 1349-1352.

35. Timur, M.; Paşa, A., Synthesis, Characterization, Swelling, and Metal Uptake Studies of Aryl Cross-Linked Chitosan Hydrogels. *ACS Omega* **2018,** *3* (12), 17416-17424.

36. Ilavsky, J.; Jemian, P. R., Irena: tool suite for modeling and analysis of small-angle scattering. *Journal of Applied Crystallography* **2009,** *42* (2), 347-353.

37. Ilavsky, J., Nika: software for two-dimensional data reduction. *Journal of Applied Crystallography* **2012,** *45* (2), 324-328.

38. Dai, X.; Chen, X.; Yang, L.; Foster, S.; Coury, A. J.; Jozefiak, T. H., Free radical polymerization of poly (ethylene glycol) diacrylate macromers: Impact of macromer hydrophobicity and initiator chemistry on polymerization efficiency. *Acta biomaterialia* **2011,** *7* (5), 1965-1972.

39. Frau, A. F.; Lane, T. J.; Schlather, A. E.; Park, J. Y.; Advincula, R. C., Modulating electrochemical activity in polyaniline/titanium oxide hybrid nanostructured ultrathin films. *Industrial & Engineering Chemistry Research* **2011,** *50* (9), 5532-5542.

40. Caldona, E. B.; De Leon, A. C. C.; Thomas, P. G.; Naylor Iii, D. F.; Pajarito, B. B.; Advincula, R. C., Superhydrophobic rubber-modified polybenzoxazine/SiO2 nanocomposite coating with anticorrosion, anti-ice, and superoleophilicity properties. *Industrial & Engineering Chemistry Research* **2017,** *56* (6), 1485-1497.

41. Cho, J. D.; Ju, H. T.; Hong, J. W., Photocuring kinetics of UV-initiated free-radical photopolymerizations with and without silica nanoparticles. *Journal of Polymer Science Part A: Polymer Chemistry* **2005,** *43* (3), 658-670.

42. Kane, M. C.; Londono, J. D.; Beyer, F. L.; Brennan, A. B., Characterization of the hierarchical structures of a dry nanopowder in a polymer matrix by X-ray scattering techniques. *Journal of Applied Crystallography* **2009,** *42* (5), 925-931.

43. Jouault, N.; Zhao, D.; Kumar, S. K., Role of casting solvent on nanoparticle dispersion in polymer nanocomposites. *Macromolecules* **2014,** *47* (15), 5246-5255.

44. Bera, O.; Pilić, B.; Pavličević, J.; Jovičić, M.; Holló, B.; Szécsényi, K. M.; Špirkova, M., Preparation and thermal properties of polystyrene/silica nanocomposites. *Thermochimica acta* **2011,** *515* (1-2), 1-5.

45. Zou, H.; Wu, S.; Shen, J., Polymer/silica nanocomposites: preparation, characterization, properties, and applications. *Chemical reviews* **2008,** *108* (9), 3893-3957.

46. Chiang, C.-L.; Ma, C.-C. M., Synthesis, characterization, thermal properties and flame retardance of novel phenolic resin/silica nanocomposites. *Polymer Degradation and Stability* **2004,** *83* (2), 207-214.

47. Zhang, F.-A.; Lee, D.-K.; Pinnavaia, T. J., PMMA/mesoporous silica nanocomposites: effect of framework structure and pore size on thermomechanical properties. *Polymer Chemistry* **2010,** *1* (1), 107-113.

48. Jankong, S.; Srikulkit, K., Preparation of polypropylene/hydrophobic silica nanocomposites. *J. Met. Mater. Miner* **2008,** *18* (2), 43-146.

APPENDIX A

PHOTOCURABLE POLY(ETHYLENE GLYCOL) DIACRYLATE RESINS WITH VARIABLE SILICA NANOPARTICLE LOADINGS

Photocurable poly(ethylene glycol) diacrylate resins with variable silica nanoparticle loadings

To be published as

Alexis Hocken, Yi Yang, Frederick L. Beyer, III, Katelyn Kline, Tyler Piper, and Matthew D. Green, "Photocurable poly(ethylene glycol) diacrylate resins with variable silica nanoparticle loading".

A1.1. Introduction

Polymer composites have been studied for decades because of their ability to join together processable polymer resins with functional additives.[1-8] The additives can range in size from 1-5 nm to 1-5 μm and can be selected for the type of functionality introduced to the matrix, such as electrical conductivity/insulation, optical characteristics, strength, etc.[9-12] These composite systems boast a density far less than the additive material and are thus touted as lightweight, multi-functional materials.[13] Due to their tunability and the breadth of potential functionalities, they are heavily used within consumer products, construction, nanoelectronics, and biomaterial applications.[1, 14-17]

Polymeric nanocomposites that are cured when exposed to light serve as promising materials for tissue engineering and 3D architectural applications because the spatiotemporal cure percentage can be externally controlled.[1, 17-20] Additionally, photopolymerizations have been explored as alternatives to injection molding wherein the propagating reactive group moves as a wave through a resin-filled mold; this implementation typically requires a monomer that can undergo cationic polymerization.[21] In either case, the composites that are constructed with

photoinitiators will form stable, covalently bonded crosslinks.[1] In the last decade, a great amount of attention has been devoted to decoupling, or at least understanding the interplay, the polymer chemistry from additive dispersion as well as to improving composite mechanical properties.[1, 3, 4, 22-27] It has been seen that the incorporation of nanoparticles into the structures can increase the composite's structural integrity.[28, 29] Nanoparticles act as anchors to stiffen the polymer matrix, contributing to a more robust material.[30]

Recent efforts have sought to further reduce the density by creating porous structures or 3D material designs. The latter must be prepared by additive manufacturing, which restricts the catalog of polymer chemistries available. A photocurable monomer or photoinitiator/monomer system would have to be utilized in order to prepare a 3D thermoset nanocomposite, wherein the resin/nanoparticle mixture was cured after printing using micro-stereolithography or technology similar to Carbon 3D (Continuous Liquid Interface Printing–CLIP).[31-34]

To use the nanoparticles to their maximum potential, it is critical to fully understand the fundamentals of their mechanical and physical properties. In this project, we studied a model photocurable polymer nanocomposite system: poly(ethylene glycol) diacrylate monomers loaded with varying weight fractions of 100 nm silica nanoparticles and a fixed concentration of photoinitiator, which were cured via UV light irradiation. Five different weight loadings of silica nanoparticles (0, 3.8, 7.4, 10.7, and 13.8 wt%) were tested to elucidate the effects on thermal, mechanical, and physical characteristics of the nanocomposite. The mechanical properties were characterized using compressive testing to determine the Young's modulus, the ultimate compressive stress, and the ultimate strain at break. Physical characteristics, such as the water uptake, the gel fraction, the cross-sectional morphology, and nanoparticle size and size distribution in the composite were determined. Finally, the thermal characteristics were revealed using

differential scanning calorimetry (DSC) and thermogravimetric analysis (TGA). This research provides a basis for understanding the mechanical capabilities and chemical properties of hydrophilic, silica-loaded nanocomposite. The ultimate goal is the development of a model system that can be used to make 3D-printable nanocomposites via stereolithography.

A1.2. Materials and Methods

A1.2.1 Chemicals

The poly(ethylene glycol) diacrylate (PEGDA, M_n = 575 g/mol) and 2-dimethoxy-2-phenylacetophenone (DMPA) were purchased from Sigma-Aldrich. The silicon dioxide (SiO_2) nanoparticles (100 nm in diameter) were purchased from NanoCym. Tetrahydrofuran (THF) was purchased from Fisher Chemical. All materials were used as received.

A1.2.2 Composites Fabrication

Composite samples were made by loading silica into PEGDA. To reduce silica aggregation, the nanoparticles were first dispersed in THF (0, 0.04, 0.08, 0.12, or 0.16 g of silica was added to 3 mL) and sonicated for 40 min. Separately, DMPA was mixed with the PEGDA at a wt/wt ratio of 0.0035:1 (DMPA:PEGDA). The THF solution was then pipetted into 1.0 g of the DMPA/PEGDA mixture and stirred at 23 ˚C for 45 min. Next, the THF was evaporated at 23 ˚C and the solution was transferred into a silicone mold and cured under UV light (wavelength of approximately 365 nm) for 3 min.

A1.2.3 Determination of sol-gel fractions

Soxhlet extraction was used to determine gel fractions. A pre-weighed sample was placed in the apparatus and 3 complete solvent wash cycles were completed. THF was used as the solvent to dissolve any remaining soluble fraction. The sample was then weighed again after air drying overnight to determine its final mass (W_f) and compared to its initial mass (W_i). The gel fraction (C) was calculated according to Eqn. 1.

$$C = \frac{W_f}{W_i} \times 100\% \quad (1)$$

A1.2.4 Water uptake determination

In a standard process, the sample was freeze dried for 14 h to ensure all water that was absorbed from atmospheric moisture was removed. First, samples were subjected to testing to determine the time required to reach equilibrium. In this equilibrium experiment, the samples were weighed every 30 min until the weight no longer increased (~2.5 h). For each subsequent experiment, all samples were equilibrated for >3 h to ensure maximum water uptake. The sample was then weighed and immersed in deionized water for 3 h to reach the absorption equilibrium.[35] The sample was removed from the water and blotted with a cloth to remove excess water on the surface. This sample's mass (W_s) was recorded and compared to its initial mass (W_d). The percent by weight of water taken up by the network (S) was calculated using Eqn. 2.[35]

$$S = \frac{W_s - W_d}{W_d} \times 100\% \quad (2)$$

Thermogravimetric analysis (TGA) was performed using a TA instruments Q500. Samples ~5 mg were heated at a rate of 10 ˚C/min from 23–600 ˚C under nitrogen.

A1.2.6 Characterization of composites morphology

The composite cross-sectional morphology was characterized using an environmental scanning electron microscope Philips XL30 ESEM-FEG operating at 15 kV. Composite samples were freeze-fractured using liquid nitrogen for cross-sectional examination, and sputter coated with gold before imaging. Small-angle X-ray scattering (SAXS) data were obtained using a Rigaku Americas, Inc., S-MAX3000 SAXS camera having a large gas-filled area detector, pinhole collimation optics, and a Confocal Max-Flux collimating optic. X-rays having $\lambda = 1.542$ Å were generated by a Rigaku MicroMax 007HFM rotating copper anode source. The isotropic two-dimensional SAXS data were corrected for background noise and sample transmission prior to azimuthal averaging into one-dimensional data in the form of intensity, I, as a function of q, where $q = 4\pi \cdot \sin(\theta)/\lambda$ and 2θ is the scattering angle. Distance and beam center calibration were performed using silver behenate. Data were placed on an absolute scale by comparison to a calibrated glassy carbon standard. All data corrections and analysis were performed using Igor Pro v. 7 (Wavemetrics, Inc.) and procedures available from Argonne National Laboratory.[36, 37]

Transmission Electron Microscopy (TEM) was performed using a JEOL JEM-2100F TEM operated at 200 kV in bright field mode. Micrographs were collected using an ORIUS SC1000 camera (Gatan, Inc.). Samples of SiO_2 nanoparticles were prepared by drop casting nanoparticle dispersions in either methanol or THF onto carbon-coated TEM grids. The nanoparticle dispersions were made by hand mixing SiO_2 powder in the desired solvent, then dispensed using a micropipette.

A1.2.7 Thermal and mechanical analysis

The glass transition temperature (T_g) was characterized using differential scanning calorimetry (DSC, Q2000 from TA Instruments). Samples of 4-6 mg and were sealed into

aluminum sample pans. The samples were subjected to a heat-cool-heat process from -100 to 200 ˚C with heating rates of 5˚C/min and a cooling rate of 10 ˚C/min. An Instron E3000 was used to perform compression testing of the silica-loaded nanocomposites. A fresh, dry sample was used for each test. The samples were cut into rectangles and then compressed at a strain rate of 0.1500 mm/min at 23 ˚C until the sample integrity was compromised.

A1.3. Results and Discussion

A1.3.1 Synthesis and characterization

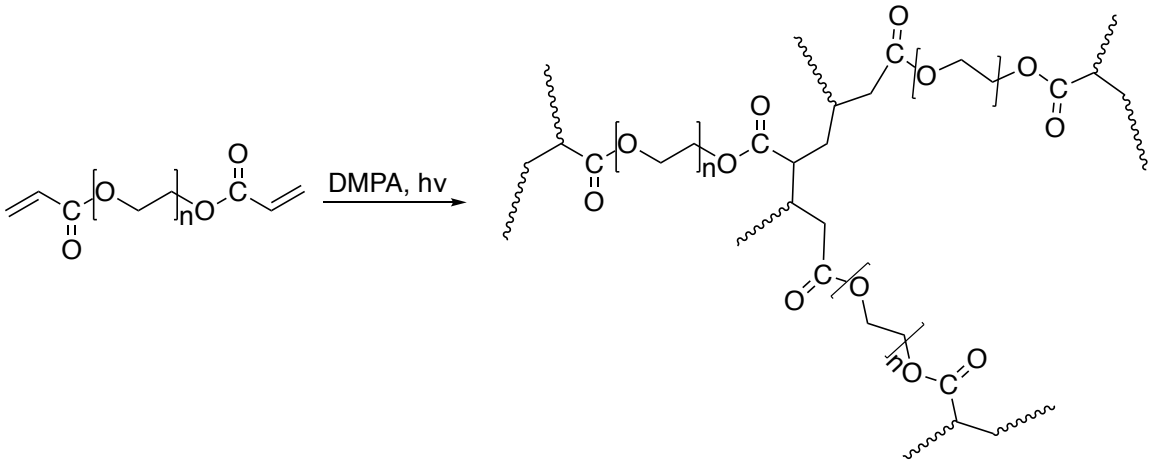

Scheme A1.1. Crosslinking reaction of PEGDA initiated by DMPA under UV light.

The photo-initiated curing of PEGDA has been well developed and proposed as a free radical polymerization mechanism,[19, 38] and the synthetic route is shown in **Scheme A1.1**. First, the optimal concentration of the photoinitiator was determined by preparing a series of PEGDA hydrogels with various DMPA concentrations without any silica nanoparticles present. After curing the resins, the gel fractions were determined using Soxhlet extraction. Briefly, the polymer was washed with an organic solvent in which the monomer is soluble for multiple cycles and the as-cured weight was compared to the weight after rinsing. THF was used as the solvent to dissolve

any un-crosslinked monomers or oligomers that remained within the structure. The highest gel fraction was obtained with 0.35 wt% DMPA; therefore, this initiator concentration was used throughout the rest of the investigation.

Next, SiO_2 nanoparticles were added at various weight fractions and the PEGDA oligomers were cured using the same process as described above. Silica nanoparticles are common additives in polymer nanocomposites because of their low cost, tunable hydrophilicity, and the ability to purchase particles across a very broad range of sizes and size distributions.[39, 40] The results shown in **Figure A1.1** reveal that the gel fraction decreased as the concentration of SiO_2 nanoparticles increased. This suggests that the SiO_2 nanoparticles inhibit crosslinking by scavenging radicals, limiting diffusion, or simply by diluting the concentration of monomer in the system. Others have observed an acceleration of the polymerization process (involving silica nanoparticles and acrylate-based monomers) but did observe that silica agglomeration at higher volume fractions reduced the reactivity.[41] However, even at the maximum silica loading of 13.8 wt% a gel fraction of 90.9% was achieved. The network with no nanoparticles added exhibited a gel fraction of 100%.

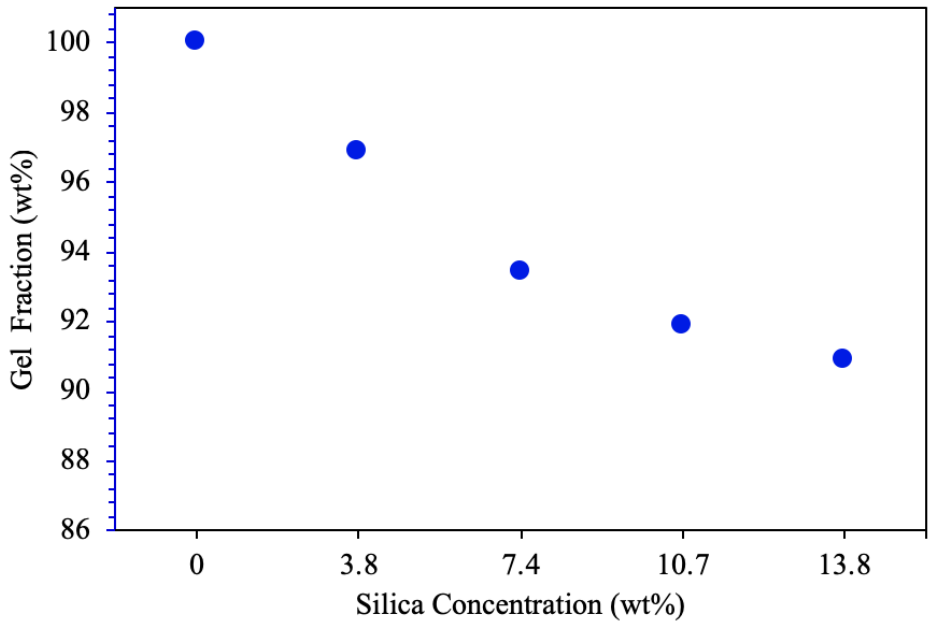

Figure A1.1. The gel fracton of PEGDA networks with varying SiO_2 concentrations.

Quantitative measurements of the nanoparticle loading in the hydrogel composites were performed using TGA (**Figure A1.2**). The TGA thermograms display dehydration weight losses of approximately 1% at temperatures below 100 ˚C. This weight loss is due to the desorption of moisture physically adsorbed from the air. A single decomposition step was observed for the series at ~360 ˚C with sharp weight losses of 95.1, 92.4, 85.5, 82.3, and 77.4 wt% as the silica loading increased from 0 to 13.8 wt%. The weight loss in this step is attributed to the decomposition of the PEG matrix. By correcting for the char weight of the PEGDA matrix, this indicates that the silica weight percentages of the series were 2.7, 10.1, 12.8, and 17.7 wt% for the 3.8, 7.4, 10.7, and 13.8 wt% silica-loaded nanocomposite samples, respectively. Thus, the TGA data confirm that increasing the silica nanoparticle loading during synthesis increased the loading in the nanocomposite.

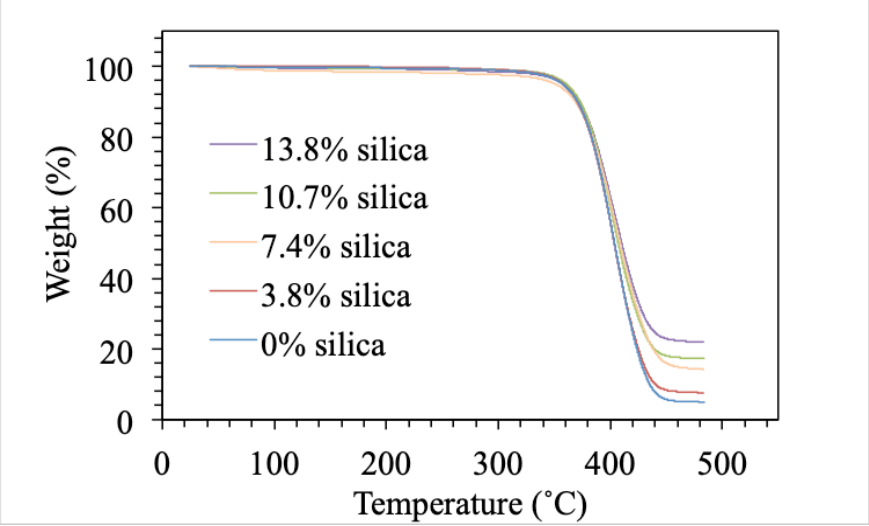

Figure A1.2. TGA thermograms showing the weight loss from thermal decomposition of the SiO_2-loaded PEGDA nanocomposites.

A1.3.2 Characterization of composite morphology

The cross-sectional morphology of silica-PEG hydrogels was examined using SEM. As shown in **Figure A1.3**, the morphology of the series of silica-PEG nanocomposites showed few features at lower nanoparticle loadings (3.8 and 7.4 wt%), but at higher loadings (10.7 and 13.8 wt%) the nanoparticles became visible. Large scale aggregates were not observed in these images, but the bulk morphology and nanoparticle distribution were further probed using SAXS.

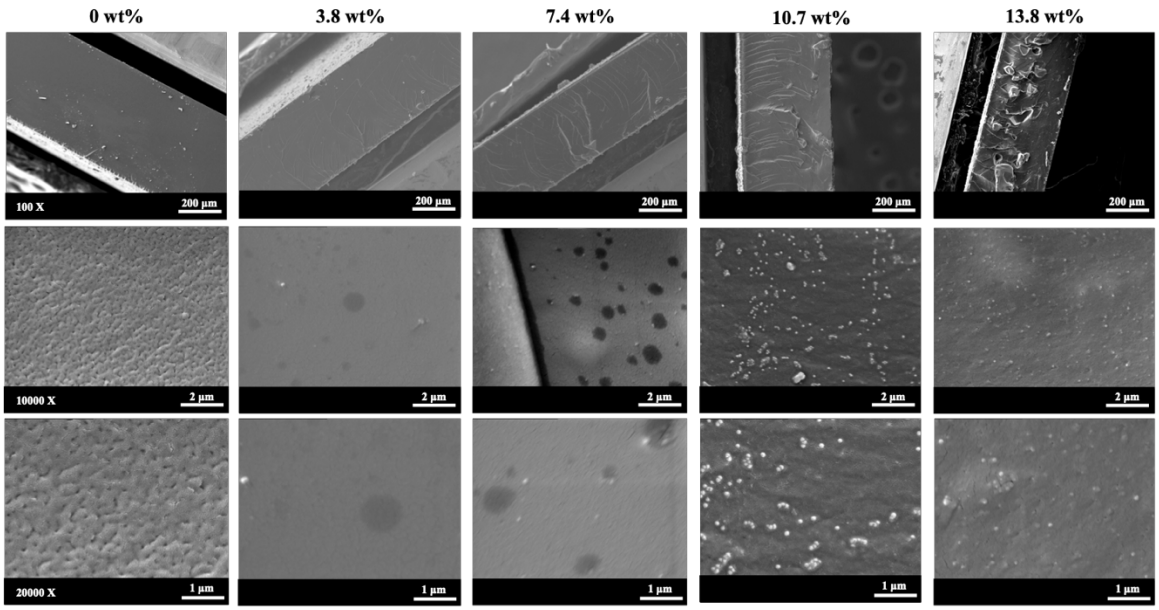

Figure A1.3. Cross-sectional SEM images of the series of composites with different silica nanoparticle loadings of 0, 3.8, 7.4, 10.7, and 13.8 wt% (left to right), at magnifications of 100x, 10,000x, and 20,000x (top to bottom). The scale bar at 100x, 10,000x and 20,000x is 200 µm, 2 µm, and 1 µm, respectively.

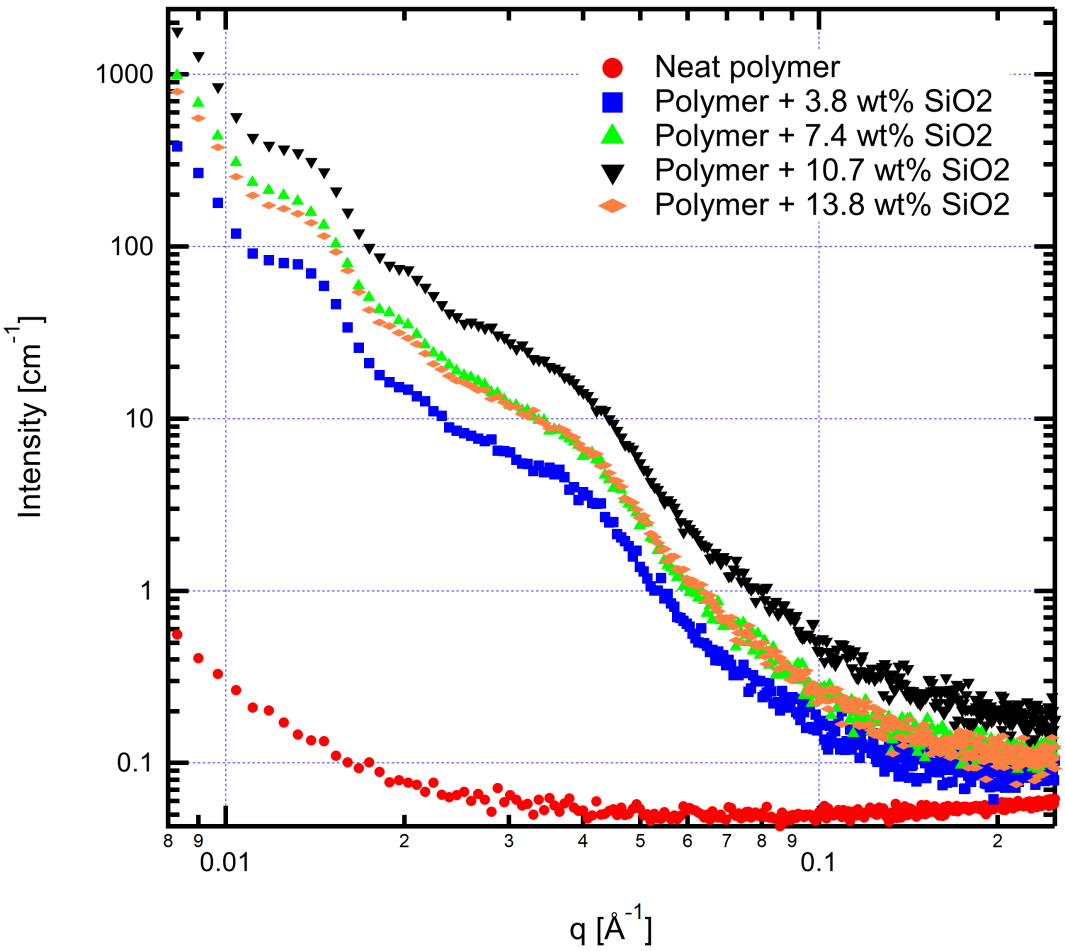

Figure A1.4. Azimuthally averaged SAXS data from the nanocomposites containing varying amounts of silica nanoparticles.

The bulk morphological behavior of the nanocomposites was investigated using SAXS, which has been shown to be useful for polymers containing nanoparticle fillers.[42] The resulting data, shown in **Figure A1.4**, reveal that the neat polymer is morphologically featureless on the size scale investigated by SAXS (roughly 1 nm to 100 nm). Addition of the nanoparticles results in a strong increase in scattered intensity at lower angles, with several distinct features in the low-*q* and mid-*q* regions. Increasing the silica content results in a corresponding increase in the scattered

intensity. The one exception to this trend is 13.8 wt% silica sample, from which the scattered intensity is roughly the same as that from the 7.4 wt% silica sample. Attempts to fit the above SAXS data using scattering from a monomodal, spherical particle having even a broad size distribution were unsuccessful. Use of a single size distribution allowed a partial fit of the scattering data in the range of $0.01 < q < 0.03$ Å^{-1}, but for no other part of the $I(q)$ data.

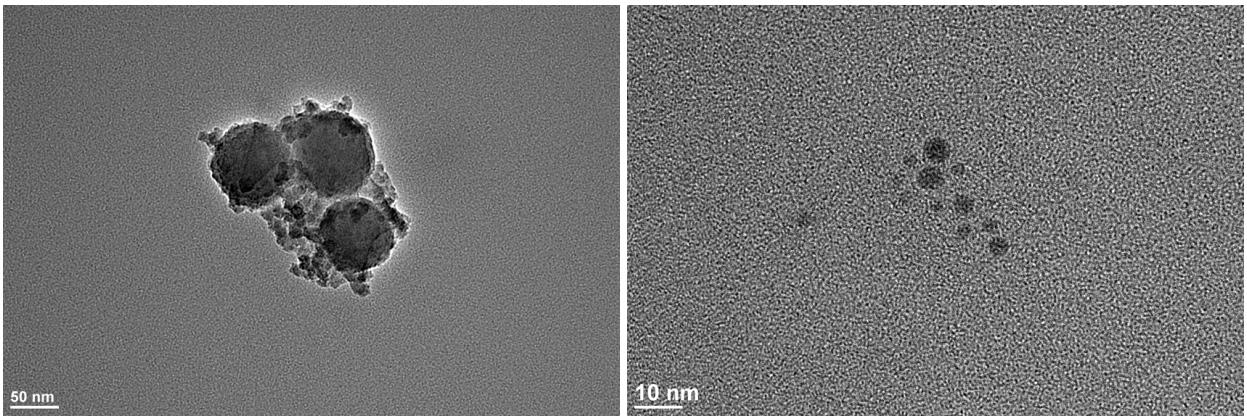

Figure A1.5. (left) An agglomerate of silica nanoparticles with various diameters, after drop-casting from THF. (right) An aggregate of silica nanoparticles with diameters of approximately 3 nm, after drop-casting from methanol.

TEM data were collected to provide complementary, real space information on the silica nanoparticles. **Figure A1.5 (left)** shows a representative TEM micrograph of an agglomerate of silica nanoparticles after dispersion in THF. Several nanoparticles roughly 85 nm in diameter can be seen, along with a large number of nanoparticles roughly 10 nm in diameter. It appears that nanoparticles having an even smaller diameter are also present. Dispersion of the nanoparticles in methanol revealed this small size component, as shown in **Figure A1.5 (right),** having a diameter of roughly 3 nm. Others have observed that the solvent used for casting nanocomposites can impact the propensity for agglomeration;[43] while these micrographs are of only the nanoparticles

it is important to note that the solvent selected for mixing the nanoparticles with the polymer matrix could impact the nanoparticle size distribution.

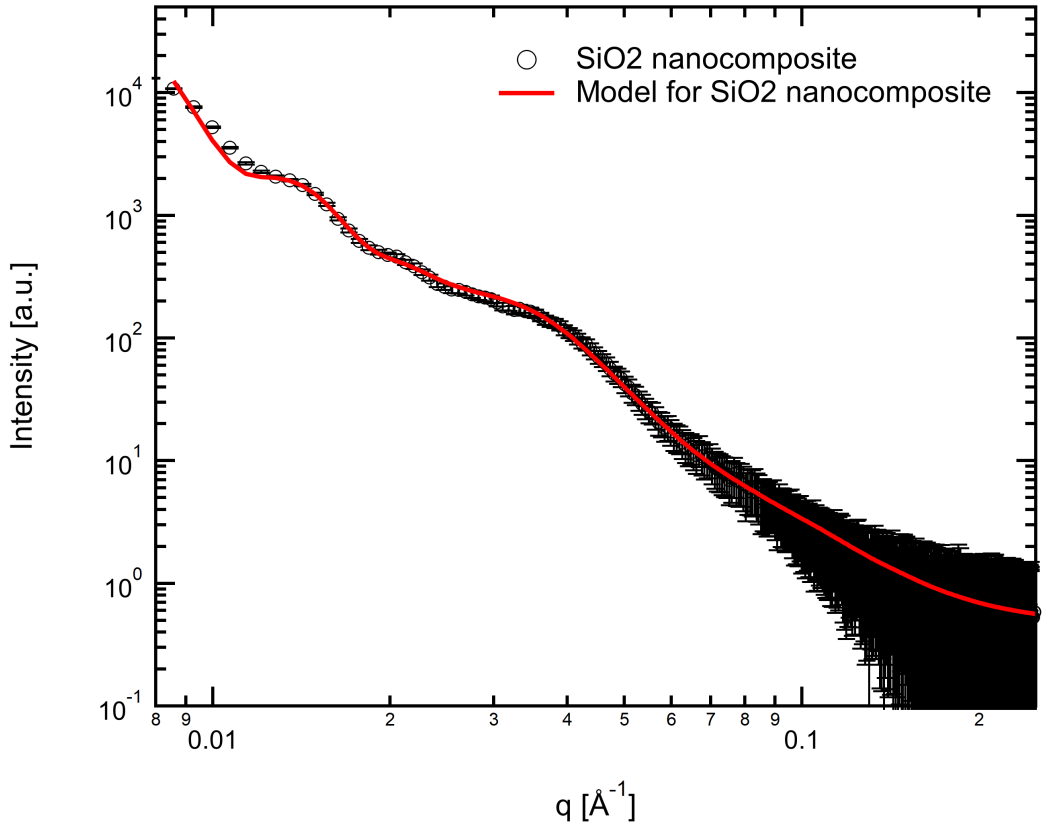

Figure A1.6. SAXS data from the silica nanoparticles as received, and the corresponding model data based on particle size information derived from TEM.

The TEM data clearly show that the silica nanoparticles used in this study contain nanoparticles having not only the target diameter (100 nm), but also at least two other distinct diameters. This information was used to create a model scattering function that was then fitted to the data, as shown in **Figure A1.6**. Although an exact fit was not determined, **Figure A1.6** shows that the model function captures the main features in the experimental SAXS data. The model function comprises a power-law background at low angles, which is a common feature in both

polymer and nanocomposite materials, three distinct particle size distributions, and a constant background. The average particle diameters for the three distributions are 82 nm, 12 nm, and 3.2 nm. The standard deviations were 9.2 nm, 2.3 nm, and 1.6 nm, respectively.

A1.3.3 Thermal and mechanical analysis of the composites

Water uptake tests were conducted to qualitatively analyze the crosslinking of the composites and to determine their relative hydrophilicity. The results, shown in **Figure A1.7** and summarized in **Table A1.1,** indicate that the loading of silica nanoparticles, from 3.8 to 13.8 wt%, does not alter the hydrophilic nature of the cured PEG network in any statistically relevant way. The glass transition temperatures (T_g) of the silica-PEG nanocomposites were measured as a function of silica concentration using DSC (**Figure A1.7)**. Upon addition of 3.8 wt% silica, the T_g of the nanocomposite decreased by ~2 ˚C. Further loading of the SiO_2 nanoparticles caused the T_g to increase by 5 ˚C up to the highest concentration of 13.8 wt%. The initial reduction of T_g is attributed to the drop in gel fraction, which enhanced the segmental mobility by decreasing the restrictions from the network on T_g.[44, 45] However, at nanoparticle concentrations >3.8 wt% the volume fraction and subsequent surface area of interaction between the nanoparticle and the matrix outweigh the decreases observed in gel fraction.[45-47] We predict that nanocomposites prepared with low weight fractions of nanoparticle that achieved gel fractions of 100% would only display increases in T_g.

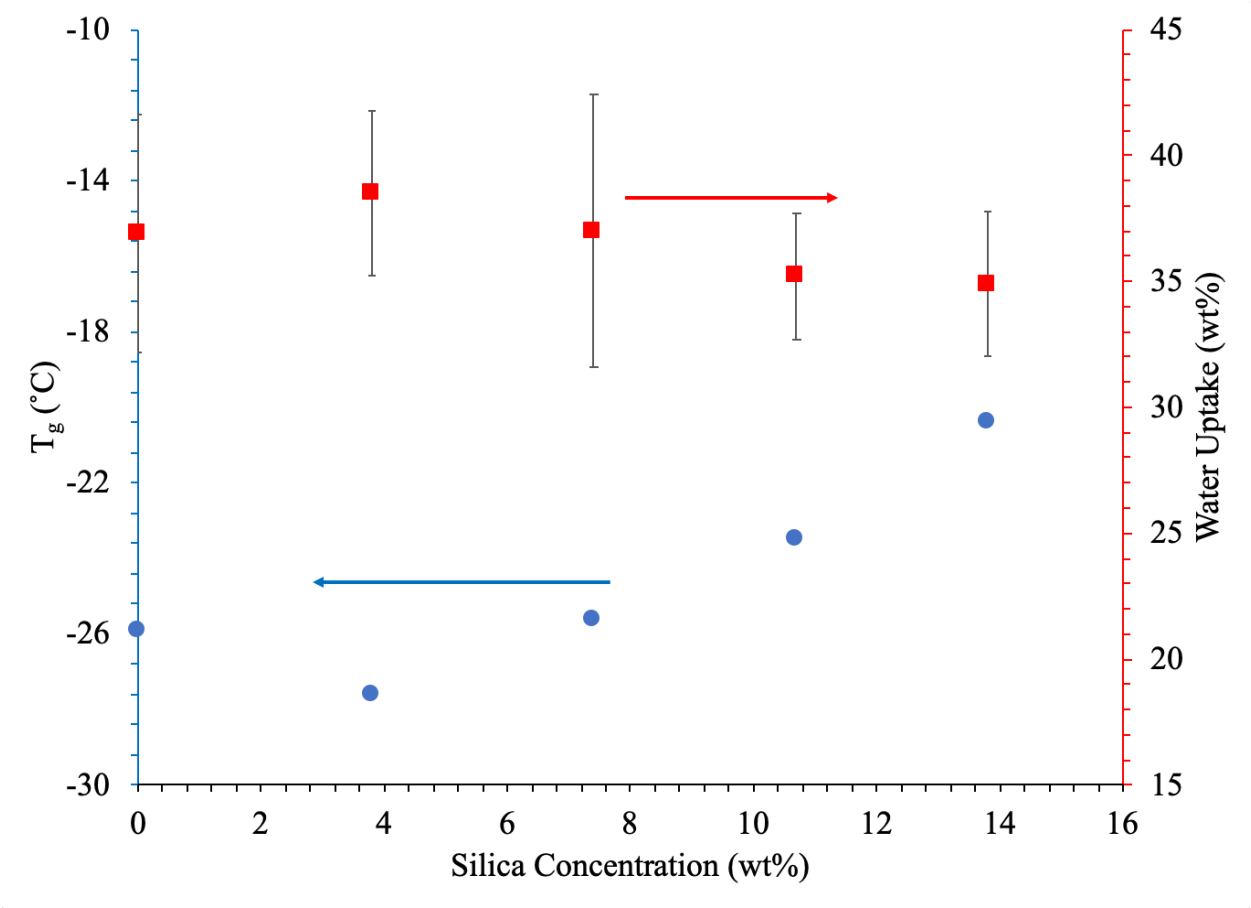

Figure A1.7. The T_g of the composites as measured by DSC and the water uptake measured gravimetrically at various silica nanoparticle concentrations. Error bars on the water uptake data indicate the mean +/- one standard deviation.

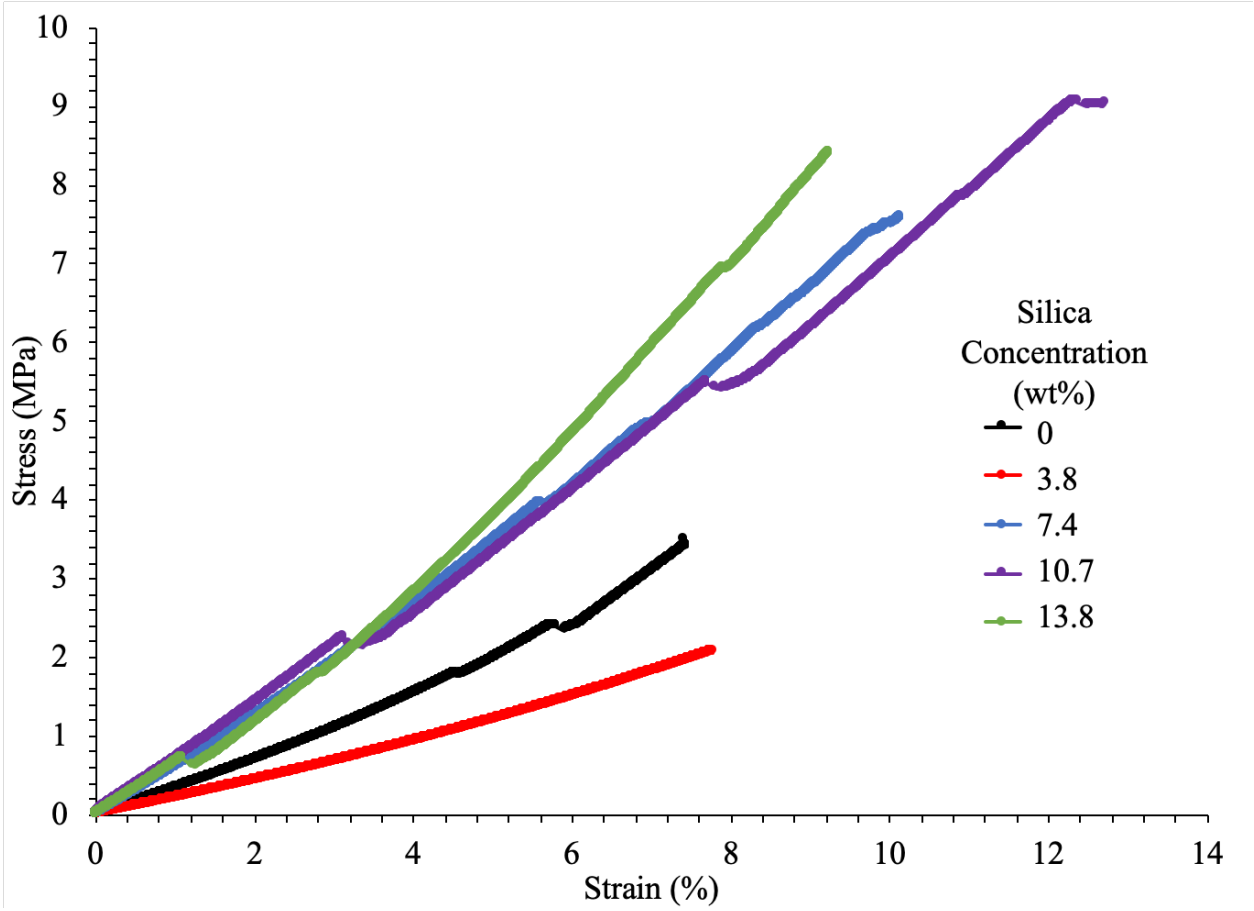

Figure A1.8. Tensile testing of the silica-loaded nanocomposites in compression mode at a strain rate of 0.150 mm/min. These traces are representative plots of three individual runs per silica loading.

The mechanical properties of the nanocomposites were determined using a static strain rate compression test (**Figure A1.8**). The data plotted are representative of three individual runs for each silica nanoparticle loading. Because of the soft nature of the PEGDA networks, the samples appeared to yield or slip multiple times during the experiment. Upon visual inspection, the sample had not yielded or deformed; these observations were consistent throughout the tensile testing. From the stress-strain curves, the Young's modulus and the Ultimate Compressive Stress were obtained. The Young's modulus was taken as the slope of the stress-strain curve at low strain and was found to be impacted by both silica concentration and the gel fraction (**Figure A1.9a**). The

addition of silica had a similar effect on the Young's modulus as it had on the T_g. As before, going from the neat PEGDA network to a silica concentration of 3.8 wt% caused a decrease in the Young's modulus, producing a softer network that we attribute to the gel fraction. However, by loading additional silica to create a 7.4 wt% composition and beyond caused the reinforcement from the addition of silica to outweigh the lower gel fraction. Therefore, the Young's modulus increased as more silica is added to the structure at silica concentrations >3.8 wt%. Interestingly, the Young's modulus did not decrease at high loadings, a hallmark or nanoparticle aggregation at high volume fractions.[47] This data, together with the cross-sectional SEM, possibly rules out percolation of the spherical nanoparticles, but does not rule out aggregates altogether.

In addition to the Young's modulus, the tensile testing showed that the higher silica nanoparticle concentration (>3.8 wt%) increased the strain at break and had an impact on the ultimate compressive strength (UCS, **Figure A1.9b**). At low nanoparticle concentrations the effect of the lower gel fraction was dominant causing a softer sample with a lower ultimate compressive strength (similar to the trend observed for T_g and Young's modulus). However, after adding more nanoparticles to achieve a 7.4 wt% composite, the reinforcement from the nanoparticles overcame the negative effects of the decreasing gel fraction. Thus, the ultimate compressive strength increased as the nanoparticle loading increased.[48] Collectively, these data suggest that the limited segmental mobility (relatively high T_g) contributed by loading silica nanoparticles at ~10 wt% overcomes the negative effects of an increased gel fraction, and also enhanced the mechanical strength 2~3 times relative to the unloaded sample. The absolute values for the Tg, gel fraction, water uptake, Young's modulus, and UCS as a function of silica concentration are summarized in Table A1.1.

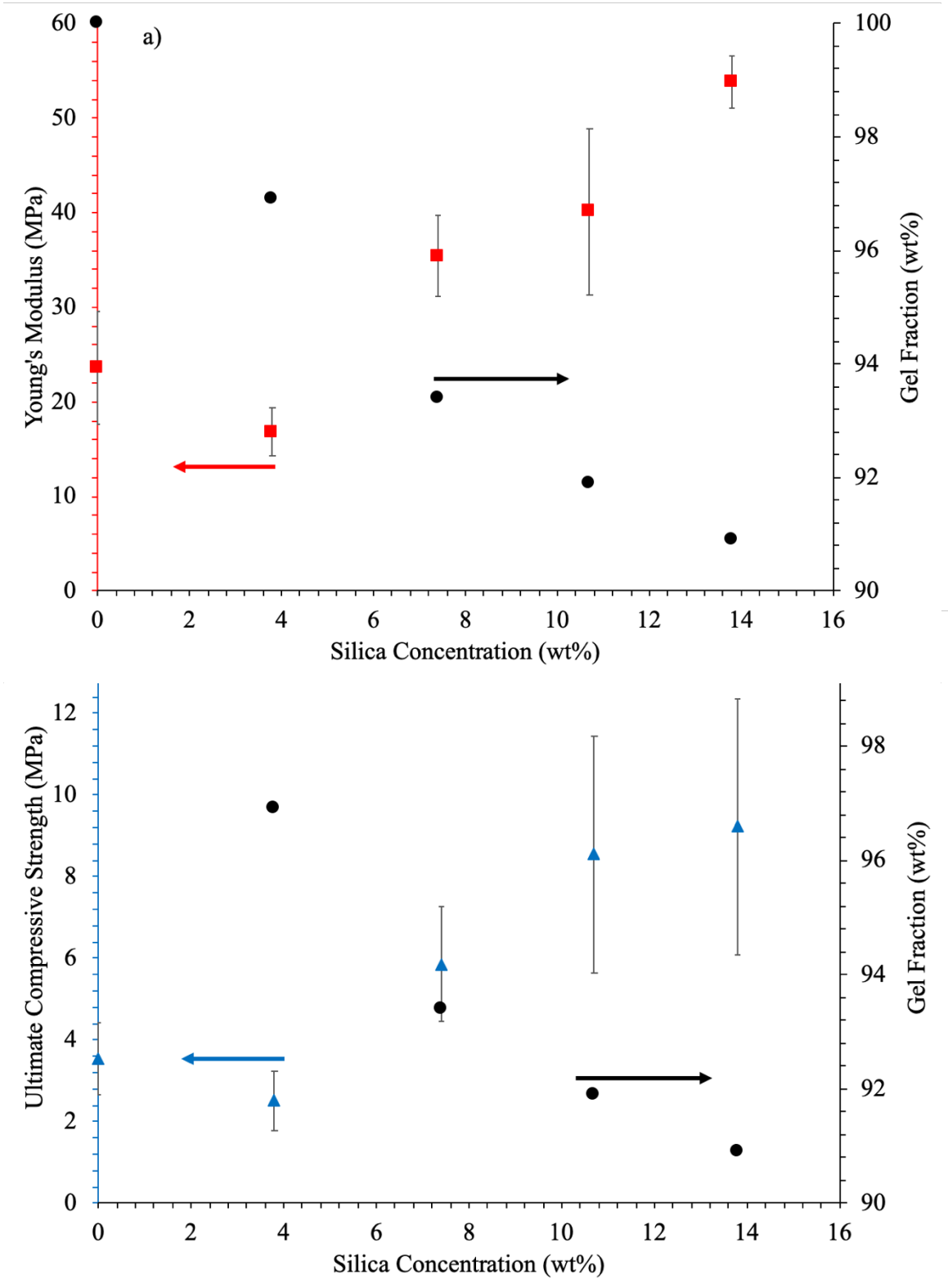

Figure A1.9. The Young's modulus (a) and ultimate compressive strength (b) as a function of silica nanoparticle concentration and gel fraction.

Table A1.1. Summary of the gel fraction, water uptake, glass transition temperature, young's modulus, and ultimate compressive stress of the series of nanocomposites with different silica loadings.

Silica Nanoparticle (wt%)	Gel Fraction (%)	Water Uptake (%)	T_g (°C)	Young's Modulus (MPa)	Ultimate Compressive Stress (MPa)
0	100	36.9 ± 4.7	-25.9	23.58 ± 5.94	3.54 ± 0.87
3.8	96.9	38.5 ± 3.3	-27.6	16.80 ± 2.53	2.52 ± 0.73
7.4	93.4	37.0 ± 5.4	-25.6	35.43 ± 4.34	5.86 ± 1.40
10.7	91.9	35.2 ± 2.5	-23.5	40.10 ± 8.75	8.55 ± 2.90
13.8	90.9	34.9 ± 2.9	-20.4	53.83 ± 2.70	9.22 ± 3.14

A1.4. Conclusions

Silica-PEG nanocomposites exhibit qualities that are promising for tissue engineering, advanced manufacturing, and structural, multifunctional materials. Higher concentrations of the silica nanoparticle limited the gel fraction obtainable and had no impact on the water uptake experiments. At low loadings, <3.8 wt%, the T_g, Young's modulus and UCS all decreased. However, the addition of silica nanoparticles at concentrations from 3.8–13.8 wt% resulted in a monotonic increase in T_g, Young's modulus, and UCS. Cross-sectional SEM and SAXS experiments indicated that some fraction of the particles existed as 82, 12, or 3.2 nm particles, all of which were also observed in TEM imaging of the nanoparticles. In summary, the low density of the silica-loaded nanocomposite gives way to creating a lightweight and multifunctional material. The tunability of this material combined with its amenability to photo-activated polymerization suggests that 3D and hierarchical assemblies are near-term possibilities.